Out-of-equilibrium dynamics in strongly correlated one-dimensional quantum many-body systems

PHD THESIS

DÁVID SZÁSZ-SCHAGRIN

Supervisor: DR. GÁBOR TAKÁCS
                Professor
                BME Institute of Physics
                Department of Theoretical Physics

M Ű E G Y E T E M   1 7 8 2

Budapest University of Technology and Economics
2024

Contents

Chapter 1

Introduction

Conceptualised over 100 years ago, quantum theory is considered one of the most successful theories of the twentieth century that forms the basis of numerous directions of contemporary physical research. Historically, quantum mechanics was used to describe the electron states and dynamics in atoms through the Schrödinger equation, which led to the atomic theory that is generally accepted today. Quantum systems containing a large number of particles, such as heavy atoms or solid-state materials, require enormous computational power to address the dynamics, an obstacle which resulted in the ever-growing field of quantum many-body theory, intending to describe the dynamics of many-body systems.

One of the most fruitful approaches to quantum many-body systems is provided by quantum field theories (QFT), originally developed as a relativistic formulation of ordinary quantum mechanics. It describes the physics of particles in terms of relativistic quantum fields and has resulted in our current understanding of fundamental physics and the standard model of particle physics describing the fundamental interactions and particles of our world. In the process, the spiking interest in high-energy physics propelled the growth of the QFT toolbox, and it can be considered to be one of the most successful and well-established theoretical frameworks of contemporary physics. These systems are generally interacting, and many are strongly correlated, especially those where the dynamics is effectively low-dimensional. Nowadays, QFT is used to investigate the collective behaviour of many quantum systems, from high-energy and solid-state physics to statistical physics and cosmology.

In particular, QFTs provide an ideal framework to study the physics of condensed matter systems. These systems are in many cases, very strongly interacting. They often exhibit phase transitions where correlations become enhanced close to the critical point, and the correlation length diverges. As a result, the corresponding critical phenomena manifest a universal behaviour at large scales and are independent of the microscopic details of the system. Their dynamics can be modelled by an appropriate field theory that describes the large-scale behaviour of the statistical system in the vicinity of the critical point [1], making QFTs a powerful tool to extract the universal behaviour of statistical physical systems.

In many condensed matter setups, the principal question is the out-of-equilibrium dynamics and thermalisation of the physical system. Recent advances in ultracold atomic experiments [2–8] opened the possibility to experimentally realise and carefully manipulate these strongly correlated quantum systems to study their dynamics and properties. This warrants accurate theoretical predictions about the dynamics of strongly interacting many-body

systems in and out of equilibrium. In these experiments, quantum fluctuations are easily suppressed by thermal fluctuations. To combat this, experiments target low-dimensional many-body systems cooled very close to zero temperature, where the quantum correlations are naturally strong due to the enhanced scattering between particles and are not overpowered by thermal fluctuations. A seminal example of these ultracold-atomic systems is the Bose-Einstein condensate first realised experimentally in 1995 [9, 10], laying the foundation for tremendous progress in realising and controlling strongly-correlated quantum many-body systems. As a result, the interest in quasi-one-dimensional systems, such as (1+1)d quantum field theories or spin chains, has increased significantly in recent years, and the demand for progress in their theoretical description is higher than ever.

In many cases, systems confined to one spatial dimension exhibit peculiar scattering behaviour that allows for exact analytical predictions. In these integrable systems, quasi-particles suffer only two-body scatterings due to the large number of conserved charges that strongly limit the dynamics. Consequently, powerful analytical approaches are available to study the properties of such systems, such as conformal field theory [1], the S-matrix bootstrap [11] or the Bethe ansatz [12–14] that allow for analytical solutions of the dynamics [15]. These models exhibit a relaxation behaviour very different from that of general quantum systems [2, 4, 7, 16, 17] which, together with their experimental realisation, accounts for their significance in contemporary condensed matter physics. Additionally, integrability has strong connections to the AdS/CFT correspondence [18], which further boosts its popularity.

Chapter 2

Non-equilibrium dynamics and thermalisation

The question of out-of-equilibrium dynamics in quantum systems is a vast subject with numerous interesting scenarios such as the equilibration of observables, transport of conserved quantities, the dynamics of inhomogeneities or time evolution of open quantum systems. One of the simplest and most common situations is that of a closed quantum system initialised in a pure state subject to unitary time evolution governed by the Schrödinger equation. In a non-equilibrium setting, the initial state is not an eigenstate of the Hamiltonian governing the time evolution, and the dynamics becomes highly non-trivial. A natural question - motivated by classical physics - is the relaxation of observables to some long-time steady state corresponding to the equilibrium. Equilibration in a generic closed quantum system can occur in multiple ways; the most natural prospect is the thermalisation of the system, where the steady-state expectation values depend only on the energy (and the corresponding temperature) of the system.

The time evolution in a generic classical mechanical system is governed by the Hamilton equations of motion which are generally non-linear. As a result, the dynamics quickly becomes independent of the microscopic details of the initial state, and the trajectories explore the available energy shell in the phase space uniformly. In the long-time limit, the time average of observables is equivalent to a statistical average given by the (micro-)canonical ensemble. This universal behaviour is called ergodicity and is due to the non-linearity of the equations of motion.

2.1   Quantum quenches and thermalisation

To understand the out-of-equilibrium time evolution of a generic isolated quantum system initiated in a pure state, we employ a simple yet powerful protocol called the *quantum quench* [19, 20], which can nowadays be routinely realised in experiments with ultra-cold atoms [2, 3, 5–8]. In this scenario, the physical system is prepared in a pure state $|\Psi_0\rangle$ that is usually the ground state of some pre-quench Hamiltonian $\hat{H}_0$. To force the system out of equilibrium, some parameters of the system are abruptly changed at time $t = 0$, resulting in a non-trivial time evolution of the system. Time evolution is governed by the linear

Schrödinger equation, and as a result, the dynamics is unitary, governed by the Hamiltonian after the quench $\hat{H}$:

$$|\Psi(t)\rangle = e^{-i\hat{H}t} |\Psi_0\rangle \ . \tag{2.1}$$

We are interested in the time evolution of expectation values of some observable $\hat{\mathcal{O}}$:

$$\langle\Psi(t)|\hat{\mathcal{O}}|\Psi(t)\rangle = \langle\Psi_0|e^{i\hat{H}t}\hat{\mathcal{O}}e^{-i\hat{H}t}|\Psi_0\rangle = \sum_{n,m} C_n^* C_m \langle n|\hat{\mathcal{O}}|m\rangle\, e^{i(E_n - E_m)t} \ , \tag{2.2}$$

where the $|n\rangle$ are the energy eigenstates of the Hamiltonian $\hat{H}$ with energy E_n and the C_n are the overlaps of the initial state and the energy eigenstates $\langle n|\Psi_0\rangle$. The above formula relates the time evolution of expectation values of local observables to equilibrium properties of the system (namely the energy spectrum) and contains dynamical information (the overlaps) that depend on the initial state. Performing the summation is generally impossible, with a few exceptions for integrable systems where specific tools such as the thermodynamic Bethe ansatz are available [21–24]. Nevertheless, Eq. (2.2) predicts the non-equilibrium time evolution of $\hat{\mathcal{O}}$ following a quantum quench in generic quantum systems.

If the expectation value (2.2) reaches a steady state, its value must be equal to the time average:

$$\bar{\mathcal{O}} = \lim_{T\to\infty} \frac{1}{T} \int_0^T dt\, \langle\hat{\mathcal{O}}(t)\rangle \ . \tag{2.3}$$

Inserting (2.2) into (2.3), in a generic quantum system with no degeneracies in the spectrum, the long-time average of an operator $\hat{\mathcal{O}}$ can be expressed by the so-called diagonal ensemble:

$$\bar{\mathcal{O}} = \sum_n |C_n|^2 \langle n|\hat{\mathcal{O}}|n\rangle \tag{2.4}$$

corresponding to a state of the system described by the density matrix

$$\hat{\rho}_{\mathrm{DE}} = \sum_n |C_n|^2 |n\rangle \langle n| \ . \tag{2.5}$$

Clearly, there is a problem here due to the fact that during the unitary time evolution, the system is at all times in a pure state given by (2.1). Additionally, the long-time average given by the diagonal ensemble (2.4) contains information on the microscopical details of the initial state in the form of the overlaps. In contrast, the thermalisation of a physical system is expected to be reflected in some ensemble average that is independent of the microscopic details of the initial state and described by a small set of macroscopical quantities such as e.g. the energy. Therefore, thermalisation is equivalent to the time average (2.3) being equal to the thermal (canonical) ensemble average given by the Gibbs ensemble:

$$\langle\hat{\mathcal{O}}\rangle_{\mathrm{GE}} = \frac{1}{Z} \mathrm{Tr}\left(\hat{\mathcal{O}}\, e^{-\beta\hat{H}}\right) \ , \tag{2.6}$$

where $Z = \mathrm{Tr}\, e^{-\beta\hat{H}}$. The diagonal ensemble (2.4), although universal, cannot describe the long-time dynamics in terms of a small set of macroscopical quantities and, as a result, cannot account for the thermalisation in itself.

2.2 The Eigenstate Thermalisation Hypothesis

The most widely accepted resolution to these problems is the Eigenstate Thermalisation Hypothesis (ETH) formulated by Deutsch [25] and Srednicki [26]. The main idea behind the ETH is that by the nature of the unitary time evolution, the thermalisation of the system does not occur at the level of the full density matrix. Instead, it is now generally accepted that equilibration only takes place for a certain set of observables whose equilibrium value can be described by the canonical (Gibbs) ensemble. The set of operators for which the ETH holds (equivalently, the set of observables that thermalise) can not be the whole set of many-body operators, as it would mean that the density matrix should transition from a pure state to a totally mixed state described by $\hat{\rho}_{\mathrm{GE}}$ which is forbidden due to the unitary time evolution. Instead, these observables are the ones that are generally accessible in a realistic setup and correspond to few-body or local observables that depend on a finite (small) number of particles or local degrees of freedom. A simple example is given by quantum spin chains, where the overall Hilbert space is constructed from constituent local Hilbert spaces corresponding to single spins localised on each site. A few-body or local operator is supported on a small number of local Hilbert spaces ("sites") that are much smaller than the length of the chain. Measurement of a local observable $\hat{\mathcal{O}}$ is equivalent to performing the expectation value $\mathrm{Tr}(\hat{\mathcal{O}}\hat{\rho})$ which includes taking the partial trace over the parts of the Hilbert space that is unaffected by the operator $\hat{\mathcal{O}}$. For a large enough system, the rest of the Hilbert space effectively acts as an environment of the support of $\hat{\mathcal{O}}$ and mixes the two parts of the Hilbert space:

$$\mathrm{Tr}_{\bar{\mathcal{O}}}\,\hat{\rho}_{\mathrm{DE}} = \mathrm{Tr}_{\bar{\mathcal{O}}}\,\hat{\rho}_{\mathrm{therm}}\,, \tag{2.7}$$

where $\mathrm{Tr}_{\bar{\mathcal{O}}}$ denotes the partial trace over the local degrees of freedom outside the support of the local observable $\hat{\mathcal{O}}$. As a result, the expectation value of the local operator $\hat{\mathcal{O}}$ is described by a mixed state $\hat{\rho}_{\mathrm{DE}}$.

The Eigenstate Thermalisation Hypothesis [25, 26] states that in the thermodynamic limit, the matrix elements of few-body (local) operators between the eigenstates of a generic Hamiltonian exhibit two important properties:

I. The diagonal elements $\mathcal{O}_{nn}$ are smooth functions of the energy of the eigenstates of the Hamiltonian and are independent of any other details of the eigenstates.

II. The off-diagonal elements $\mathcal{O}_{nm}$, $n \neq m$ are suppressed exponentially in the system size.

These two statements can be cast into the mathematical form

$$\mathcal{O}_{nm} = \mathcal{O}(E)\delta_{nm} + e^{-\frac{S(E)}{2}} f_{\hat{\mathcal{O}}}(E, \Delta E)R_{nm}\,, \tag{2.8}$$

where $\mathcal{O}_{nm}$ denotes the matrix element $\langle n|\hat{\mathcal{O}}|m\rangle$, $|n\rangle$ are the eigenstates of the Hamiltonian $\hat{H}$ with energy E_n, $\mathcal{O}(E)$ and $f_{\hat{\mathcal{O}}}(E, \Delta E)$) are smooth functions depending on the variables $E = (E_n + E_m)/2$ and $\Delta E = E_n - E_m$. $S(E)$ is the thermodynamic entropy of the system, and R_{nm} is a random variable with zero mean and unit variance. A consequence of the ETH is that if the energy fluctuations in the initial state are negligible in the thermodynamic limit (corresponding to infinite system size), the diagonal ensemble average is equivalent to

the microcanonical ensemble average corresponding to energy E. Finally, the equivalence between the microcanonical and canonical ensembles in the thermodynamic limit follows from ordinary statistical mechanics, and as a result, the steady-state expectation value of the local observable $\hat{\mathcal{O}}$ is given by the thermal average:

$$\sum_n |C_n|^2 \langle n|\hat{\mathcal{O}}|n\rangle \xrightarrow{\text{TDL}} \frac{1}{Z}\text{Tr}\left(\hat{\mathcal{O}}\, e^{-\beta\hat{H}}\right) . \tag{2.9}$$

Equivalently, the steady-state expectation value $\bar{\mathcal{O}}$ becomes independent of the microscopic details of the initial state and takes the value corresponding to the thermal distribution $\hat{\rho}_{\text{GE}}$ associated with thermalisation.

Therefore, the ETH can be considered to be the quantum equivalent of the ergodicity principle in classical statistical mechanics. It describes the observed thermalisation in isolated quantum systems through the equilibration of few-body observables that are accessible in realistic experimental scenarios. Thermalisation of a closed quantum system is therefore equivalent to thermalisation of these local observables for which ETH holds. The ETH has now been observed in various setups [27–39] and has been generally accepted as the underlying mechanism behind the thermalisation of isolated quantum systems.

2.3 Equilibration of integrable systems

In generic quantum systems where the ETH holds, the expectation values of suitable observables eventually thermalise to a steady state described by thermal distribution. However, some systems violate the ETH and do not thermalise in the usual sense.

The most well-known exceptions are integrable models with an infinite number of local conserved charges. Even though equilibration in a certain sense has been observed in integrable systems [4, 5, 7, 16, 17], the steady-state expectation values differ from the thermal predictions associated with the thermalisation of the system. The infinitely many local quantities that are conserved during the time evolution encode information about the initial state of the system, and the initial distribution of charges has to be reflected in the steady state, which is not accounted for by the standard Gibbs ensemble. A resolution proposed in [40, 41] is the idea of the steady state being described by a *generalised* Gibbs ensemble that takes into account all local conserved charges Q_j of the integrable system:

$$\langle\hat{\mathcal{O}}\rangle_{\text{GGE}} = \frac{1}{Z}\text{Tr}\,\hat{\mathcal{O}}\, e^{-\sum_j \lambda_j Q_j} \tag{2.10}$$

where the partition function $Z = \text{Tr}e^{-\sum_j \lambda_j Q_j}$ ensures normalisation and the λ_j are generalised chemical potentials which are Lagrange multipliers originating from the maximal entropy principle [42]. The validity of GGE has been proven to predict the equilibration of free systems [43–47] and has been tested experimentally [16]. However, for the Heisenberg spin chain, the GGE fails to describe the steady state of the system for generic initial states [48, 49]. Instead, the long-time average is described by the so-called *complete* generalised Gibbs ensemble [50] which, in addition to the set of local charges present in the GGE, also incorporates a set of quasi-local charges as well [51, 52]. The specific set of quasi-local

quantities that is necessary for the complete GGE is generally an open question, and the complete GGE today is only known in certain cases such as the Heisenberg spin chain [50] and SU(3) spin chains [53].

Apart from integrable systems, the ETH is violated in special non-integrable systems admitting solutions called *many-body scar states* [54–60]. Many-body scars are energy eigenstates for which the expectation values of local observables are very far from what is predicted by the thermal average. Typically, many-body scars form a zero-measure infinite set within the Hilbert space which corresponds to a set of expectation values of local fields that violate the ETH. The origin of many-body scar states is generally an open question, together with their fate in the thermodynamic limit: thermalisation of the system corresponds to satisfying the usual (also called *strong*) ETH (2.8) which requires the disappearance of these states. Alternatively, if scar states do persist in the spectrum, forming a zero-measure set, the *weak* form of ETH holds, where the energy eigenstates appearing in (2.8) are restricted to non-scar states. If, instead, these many-body scar states form a finite density set in the spectrum, even the weak ETH is violated, and the system fails to thermalise in general.

Closely related to integrability, systems exhibiting many-body localisation (MBL) [61–68] also violate the ETH and therefore fail to thermalise. MBL is the many-body generalisation of Anderson localisation [69] and results from the disorder of an isolated many-body system. MBL generally breaks ergodicity due to a new kind of emergent "integrability" of the system: MBL is characterised by a set of quasi-local integrals of motion [67, 68, 70] that similarly to the usual integrability, results in the violation of ETH and prevents the system from thermalising. This "localised integrability" is very different from the usual integrability. Nevertheless, the structure of the set of quasi-local integrals of motion forbids systems with MBL to equilibrate, contrary to usual integrable systems.

Chapter 3

Models

This work studies the out-of-equilibrium time evolution and related phenomena in (1+1)-dimensional, strongly correlated quantum systems. In the following, we introduce the models studied, discussing only the details relevant to our investigation. As mentioned in Chapter 2, the relaxation of observables changes significantly if the system is integrable, motivating us to consider integrable and non-integrable systems as well.

First, in Section 3.1, we review the spin-1/2 XXZ spin chain, focusing on the phase diagram and the charges and currents characterising the model. We then turn to continuous field theories, starting with the (1+1)-dimensional φ^4 theory, which we discuss in Section 3.2. The sine-Gordon model is introduced in Section 3.3.

3.1 The XXZ spin chain

One-dimensional spin chains are at the heart of contemporary condensed matter physics. On the one hand, spin chains can nowadays be realised in experiments with ultracold atoms or certain magnetic crystals [71–75]. On the other hand, many of these systems exhibit integrable properties that allows for powerful theoretical tools to study these systems exactly [14]. Due to the simple structure of their Hilbert space and the available theoretical techniques, integrable spin chains provide an excellent platform to study the notion of integrability and its breakdown in quantum many-body systems.

One of the most important integrable spin chains is the spin-1/2 XXZ model. Experimental realisations of the model using ultracold atoms in Rydberg states [73] and magnetic atoms [75] and crystals such as $Cs_2CoCl_4^2$ [74] opened up the possibility of experimentally probing its dynamics and properties. The spin-1/2 XXZ spin chain is described by the Hamiltonian

$$\hat{H}_{\text{XXZ}} = \sum_{i=1}^{L} \left[\hat{s}_i^x \hat{s}_{i+1}^x + \hat{s}_i^y \hat{s}_{i+1}^y + \Delta \hat{s}_i^z \hat{s}_{i+1}^z \right] \tag{3.1}$$

where the spin operators are defined as $\hat{s}^a = \frac{1}{2}\hat{\sigma}^a$ using the Pauli operators

$$\hat{\sigma}^x = \begin{bmatrix} 0 & 1 \\ 1 & 0 \end{bmatrix} \quad \hat{\sigma}^y = \begin{bmatrix} 0 & -i \\ i & 0 \end{bmatrix} \quad \hat{\sigma}^z = \begin{bmatrix} 1 & 0 \\ 0 & -1 \end{bmatrix}, \tag{3.2}$$
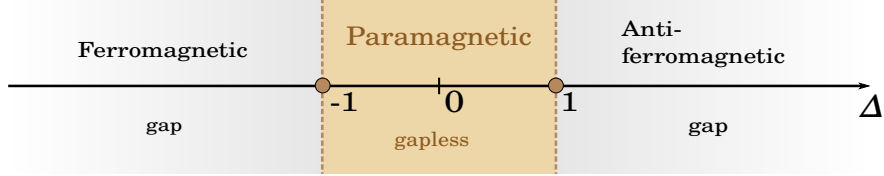
Figure 3.1: The phase diagram of the spin-1/2 XXZ spin chain.

and Δ is the (real) anisotropy parameter. Working with a finite chain, we specify periodic boundary conditions $\hat{s}^a_{L+1} \equiv \hat{s}^a_1$. The model has three distinct phases as a function of Δ, illustrated in Fig. 3.1:

I. The phase $\Delta < -1$ is gapped, corresponding to an Ising ferromagnet. In the limit $\Delta \to -\infty$, the two degenerate ground states

$$|\text{GS}_\uparrow\rangle = \prod_{j=1}^L |\uparrow_j\rangle \quad \text{and} \quad |\text{GS}_\downarrow\rangle = \prod_{j=1}^L |\downarrow_j\rangle \tag{3.3}$$

are related to each other by flipping every spin. The low-energy excitations are single magnons and their bound states [14].

II. For $-1 < \Delta < 1$, the gap in the spectrum disappears, and the ground state is a paramagnetic ground state with zero magnetisation. For $\Delta = 0$, the XXZ chain reduces to the XX model, which can be mapped to a system of free spinless fermions on a lattice through Jordan-Wigner transformation [14].

III. There is a gap again for $\Delta > 1$, and the phase corresponds to an Ising antiferromagnet. In the limit of $\Delta \to \infty$, the degenerate ground states are Néel states, written as

$$|N_1\rangle = |\uparrow_1, \downarrow_2, \uparrow_3, ...\rangle \quad \text{and} \quad |N_2\rangle = |\downarrow_1, \uparrow_2, \downarrow_3, ...\rangle \; . \tag{3.4}$$

Again, the ground states $|N_{1,2}\rangle$ can be transformed into each other by flipping each spin. In the low-energy sector, the excitations are spinors, corresponding to domain walls, regions in space where one type of Néel state changes into the other, forming two unidirectional adjacent spins.

The points $|\Delta| = 1$ are special as the system admits additional symmetries. In the following, we focus on regions of the anisotropy parameter away from these points, and so we restrain ourselves from further discussions of the parameters $\Delta = \pm 1$[1].

The XXZ chain is an integrable model characterised by an infinite set of conserved charges $\hat{Q}^\alpha$, $\alpha = 1, 2, 3 \ldots$ that commute with each other and the Hamiltonian (3.1). The charges $\hat{Q}^\alpha$ are extensive and expressed as a sum of local charge densities $\hat{q}^\alpha_j$

$$\hat{Q}^\alpha = \sum_{j=1}^L \hat{q}^\alpha_j \,, \tag{3.5}$$

---

[1]Interested readers will find a detailed discussion in [14].

that are localised on α sites around site j. Their conservation is expressed through the respective continuity equation

$$\hat{j}_{l+1}^{\alpha} - \hat{j}_{l}^{\alpha} = i \left[\hat{q}_{l}^{\alpha}, \hat{H}_{\text{XXZ}} \right] , \tag{3.6}$$

which defines the corresponding generalised current $\hat{J}^{\alpha}$:

$$\hat{J}^{\alpha} = \sum_{j=1}^{L} \hat{j}_{j}^{\alpha} . \tag{3.7}$$

Historically, the construction of the charges is given through the quantum inverse scattering method (QISM) by Fadeev et al. [12]. Recently, Pozsgay discovered an algebraic construction of the generalised currents in [76], which can be applied to a number of integrable systems apart from the XXZ chain. For the XXZ model, the first two charges correspond to the total magnetisation

$$\hat{Q}^{1} = \hat{S}^{z} = \sum_{j=1}^{L} \hat{s}_{j}^{z} \tag{3.8}$$

and the Hamiltonian (energy) of the system:

$$\hat{Q}^{2} = \sum_{j=1}^{L} \hat{q}_{j}^{2} , \quad q_{j}^{2} = \hat{s}_{j}^{x} \hat{s}_{j+1}^{x} + \hat{s}_{j}^{y} \hat{s}_{j+1}^{y} + \Delta \hat{s}_{j}^{z} \hat{s}_{j+1}^{z} . \tag{3.9}$$

The first non-trivial charge that corresponds to the integrability of the XXZ model is given by

$$\hat{Q}^{3} = \sum_{l=1}^{L} \hat{q}_{l}^{3} ,$$
$$\hat{q}_{l}^{3} = \hat{s}_{l-1}^{x} \hat{s}_{l}^{z} \hat{s}_{l+1}^{y} - \hat{s}_{l-1}^{y} \hat{s}_{l}^{z} \hat{s}_{l+1}^{x} + \Delta \left(-\hat{s}_{l-1}^{z} \hat{s}_{l}^{x} \hat{s}_{l+1}^{y} + \hat{s}_{l-1}^{z} \hat{s}_{l}^{y} \hat{s}_{l+1}^{x} - \hat{s}_{l-1}^{x} \hat{s}_{l}^{y} \hat{s}_{l+1}^{z} + \hat{s}_{l-1}^{y} \hat{s}_{l}^{x} \hat{s}_{l+1}^{z} \right) , \tag{3.10}$$

together with the corresponding conserved current

$$\hat{J}^{3} = \sum_{l=1}^{L} \hat{j}_{l}^{3} ,$$
$$\hat{j}_{l}^{3} = -\frac{1}{2} \Bigg[2\Delta \left(\hat{s}_{l-2}^{x} \hat{s}_{l-1}^{y} \hat{s}_{l}^{x} \hat{s}_{l+1}^{y} + \hat{s}_{l-2}^{x} \hat{s}_{l-1}^{z} \hat{s}_{l}^{x} \hat{s}_{l+1}^{z} + \hat{s}_{l-2}^{y} \hat{s}_{l-1}^{x} \hat{s}_{l}^{y} \hat{s}_{l+1}^{x} + \hat{s}_{l-2}^{y} \hat{s}_{l-1}^{z} \hat{s}_{l}^{y} \hat{s}_{l+1}^{z} \right.$$
$$+ \hat{s}_{l-2}^{z} \hat{s}_{l-1}^{x} \hat{s}_{l}^{z} \hat{s}_{l+1}^{x} + \hat{s}_{l-2}^{z} \hat{s}_{l-1}^{y} \hat{s}_{l}^{z} \hat{s}_{l+1}^{y} - \hat{s}_{l-2}^{x} \hat{s}_{l-1}^{y} \hat{s}_{l}^{y} \hat{s}_{l+1}^{x} - \hat{s}_{l-2}^{y} \hat{s}_{l-1}^{x} \hat{s}_{l}^{x} \hat{s}_{l+1}^{y} \big)$$
$$- 2 \left(\hat{s}_{l-2}^{x} \hat{s}_{l-1}^{z} \hat{s}_{l}^{z} \hat{s}_{l+1}^{x} + \hat{s}_{l-2}^{y} \hat{s}_{l-1}^{z} \hat{s}_{l}^{z} \hat{s}_{l+1}^{y} \right) - 2\Delta^{2} \left(\hat{s}_{l-2}^{z} \hat{s}_{l-1}^{x} \hat{s}_{l}^{x} \hat{s}_{l+1}^{z} + \hat{s}_{l-2}^{z} \hat{s}_{l-1}^{y} \hat{s}_{l}^{y} \hat{s}_{l+1}^{z} \right) \Bigg]$$
$$- \frac{1+\Delta^{2}}{4} \left(\hat{s}_{l-1}^{x} \hat{s}_{l}^{x} + \hat{s}_{l-1}^{y} \hat{s}_{l}^{y} \right) - \frac{\Delta}{2} \hat{s}_{l-1}^{z} \hat{s}_{l}^{z} . \tag{3.11}$$

3.2 The (1+1)d φ^4 model

The simplest example of an interacting, non-integrable, relativistic quantum field theory is provided by the (1+1)d φ^4 theory. It is the simplest non-trivial Ginzburg-Landau theory and gives the scaling limit of the Ising model [1]. As such, the model is subject to a second-order phase transition where $\mathbb{Z}_2$ symmetry is spontaneously broken, characteristic of the Ising universality class. Therefore, studying the theory enables understanding universal behaviour in Ising-like ferromagnets near the critical point, independent of lattice details. Apart from its importance in statistical physics, the (1+1)d φ^4 model describes the one-dimensional analogue of the Higgs field in the Standard Model. Consequently, studying the dynamics of the theory is expected to reveal some general characteristics of the elementary particle, such as the proposed decay of the false vacuum [77].

The theory is a textbook example of interacting relativistic quantum field theories. As such, it has been widely studied using perturbation theory [78,79] and by various implementations of the truncated Hamiltonian approach, both on the massless free boson basis [80] and the Fock space of the massive free boson [81–83].

The φ^4 model is non-integrable. Therefore, the expectation values of local observables are expected to thermalise at long times to the thermal distribution. However, as pointed out by Durnin et al. in [84], the time scale at which the relaxation takes place is much larger than general non-integrable models. The origin of the much larger time scale can be understood perturbatively: at first order in perturbation theory, the φ^4 interaction allows only for fully elastic two-particle scattering processes, reminiscent of integrability and therefore, it is classified as weak integrability breaking [85].

Classically, the (1+1)d φ^4 model is given by the Hamiltonian

$$H = \int dx \left[\frac{1}{2}(\partial_t \varphi)^2 + \frac{1}{2}(\partial_x \varphi)^2 \pm \frac{1}{2}m^2\varphi^2 + \frac{\lambda}{4!}\varphi^4 \right] \tag{3.12}$$

describing a bosonic field $\varphi(x,t)$ subject to a quartic self-interaction. From now on, we work in units in which $c = \hbar = 1$, and so dimensionful physical parameters can be measured in units of some characteristic energy scale m_{scale}, whose choice is usually dependent on the details of the theory. Here, a natural choice for this scale is the mass m appearing in the Hamiltonian (3.12), and so the interaction strength is characterised by the dimensionless parameter λ/m^2. We also use the parameter $g = \frac{\lambda}{4m^2}$ in the following.

The theory admits two distinct phases characterised by the sign of the coefficient of the φ^2 term in (3.12): when the sign is positive, the $\mathbb{Z}_2$ transformation $\varphi \to -\varphi$ is a global symmetry, and the theory is in the disordered (paramagnetic) phase. For a negative coefficient, the $\mathbb{Z}_2$ symmetry is spontaneously broken and leads to a potential with two degenerate minima at $\varphi = \pm\sqrt{6m^2/\lambda}$ corresponding to an Ising-type ferromagnetic phase.

Expanding the potential around these minima

$$V\left(\pm\sqrt{\frac{6m^2}{\lambda}} + \eta\right) = -\frac{6m}{4\lambda} + m^2\eta^2 \pm m\sqrt{\frac{\lambda}{6}}\eta^3 + \frac{\lambda}{24}\eta^4 = -\frac{3m}{2\lambda} + \frac{1}{2}m_0^2\eta^2 + \dots \tag{3.13}$$

gives the mass of the elementary particle $m_0 = \sqrt{2}m$. The theory also admits static kink

and antikink solutions interpolating between the two vacua:

$$\phi_{\text{kink}}^{\pm} = \pm\sqrt{\frac{6m^2}{\lambda}} \tanh\left(\frac{mx}{\sqrt{2}}\right), \tag{3.14}$$

where the (+) refers to the kink and (-) to the antikink, and have energy

$$M_0 = \frac{m_0}{g}. \tag{3.15}$$

Kink solutions moving with velocity v can be generated by appropriate Lorentz transformation due to the relativistic nature of the theory. Bound states of a kink and antikink are called oscillons [86], which are quasi-periodic solutions of the classical equations of motion forming a continuous spectrum. However, they are not stable as they are constantly losing energy in the form of outgoing radiation of small fluctuations, which depends on their oscillation amplitude.

Semi-classical quantisation

The theory can be quantised semi-classically by quantising the fluctuations around the minima of the potential. To avoid divergences, the theory needs to be regularised via normal ordering with respect to some free theory. In the work by Dashen et al. [87], the reference theory is chosen to be the infinite volume free theory with mass m_0, describing the (free bosonic) fluctuations around any of the minima of (3.13). The semi-classical mass shift of the kinks and related objects needs to be calculated non-perturbatively, and so the authors quantised the theory around the saddle point of the semi-classical path integral [87]. The semiclassical correction to the kink (and antikink) mass is given by

$$M = M_0 - m_0 c = \frac{4\sqrt{2}m^3}{\lambda} - \sqrt{2}mc + \mathcal{O}(\lambda), \qquad c = \frac{3}{2\pi} - \frac{1}{4\sqrt{3}}, \tag{3.16}$$

where the parameters m and λ are the coefficients appearing in the renormalised Hamiltonian.

Although classically unstable, the kink-antiking bound states (oscillons) can still be quantised. Semi-classically, they correspond to periodic breathers, and their spectrum becomes discrete [88]:

$$m_n = 2M \sin\left(n\frac{\zeta}{2}\right) \qquad \zeta = \frac{g}{1 - gc}. \tag{3.17}$$

Although the theory is non-integrable, at the quantum level, the lightest breather ($n = 1$) is identified with the elementary particle (small fluctuations), and therefore, it is stable. Higher breathers can be considered as bound states of the $n = 1$ breather, and their stability against decays into the lightest particle requires

$$m_n < 2m_1, \tag{3.18}$$

which only holds for $n = 2$, but not for $n \geq 3$. This is still true at the quantum level [88], where only two stable breather solutions exist. However, as the quartic coupling g increases, the spectrum changes, and the second breather becomes unstable around

$$g_{\text{B2}}^* = \frac{\pi/2}{(1 + c\pi/2)} \approx 1.031, \tag{3.19}$$

decaying into a kink and an antikink. Further increasing g, the first breather also disappears from the spectrum by decaying into a kink-antikink pair for

$$g > g_{\text{B1}}^* = \frac{\pi}{(1 + c\pi)} \approx 1.535. \tag{3.20}$$

Perturbative results

At the quantum level, the bosonic field φ becomes an operator $\hat{\varphi}$, and the Hamiltonian takes the form

$$\hat{H} = \int dx : \left[\frac{1}{2}(\partial_t \hat{\varphi})^2 + \frac{1}{2}(\partial_x \hat{\varphi})^2 \pm \frac{1}{2}m^2\hat{\varphi}^2 + \frac{\lambda}{4!}\hat{\varphi}^4 \right] : \tag{3.21}$$

the semicolons denote normal ordering with respect to some infinite-volume free theory with some mass m_0. Choosing the $(+)$ sign in the above Hamiltonian describes the system in the $\mathbb{Z}_2$-symmetry phase. Here, the spectrum is gapped, and its value can be computed perturbatively in the quartic coupling λ using resummation techniques [78]. Up to 8th order, it is given by:

$$\frac{M^2}{m^2} = 1 - \frac{3}{2}g_4^2 + \left(\frac{9}{\pi} + \frac{63\zeta(3)}{2\pi^3} \right) g_4^3 - 14.655869(22)g_4^4 + 65.97308(43)g_4^5 \\ -347.8881(28)g_4^6 + 2077.703(36)g_4^7 - 13771.04(54)g_4^8 + O(g_4^9). \tag{3.22}$$

where $g_4 = \lambda/24$ is the coefficient of the $: \varphi^4 :$ term in the Hamiltonian (3.21). The vacuum energy density can be similarly obtained and up to 8th order reads:

$$\Lambda/m^2 = -\frac{21\zeta(3)}{16\pi^3}g_4^2 + \frac{27\zeta(3)}{8\pi^4}g_4^3 - 0.116125964(91)g_4^4 + 0.3949534(18)g_4^5 \\ -1.629794(22)g_4^6 + 7.85404(21)g_4^7 - 43.1920(21)g_4^8 + O(g_4^9). \tag{3.23}$$

When the sign of the quadratic term in (3.21) is negative, the $\mathbb{Z}_2$ symmetry is spontaneously broken, and the spectrum is built up from kinks, antikinks and two stable breather solutions. As mentioned before, the elementary particle is identified with the lightest breather corresponding to the gap in the spectrum. A perturbative expansion of its mass m_1 reads as [89]:

$$m_1^2(g) - m_0^2 = \\ m_0^2 \left(-\frac{g}{2\sqrt{3}} - \frac{1}{36} \left(0.375 + 2.2492 + 2.8020 - \frac{1}{2}(1.06864 + 1.9998 + 5.50025) \right) g^2 \right). \tag{3.24}$$

Perturbative result regarding the second breather mass can be computed from [89]

$$m_2 = 2m_1 \cos \frac{g}{2} \tag{3.25}$$

using (3.24).

15

3.3 The sine-Gordon model

The sine-Gordon model is a paradigmatic example of an integrable relativistic quantum field theory. Besides its theoretical significance in quantum field theory, the theory describes the low-energy dynamics of many gapped one-dimensional systems, such as, e.g., bosonic and fermionic Hubbard models [90–93], spin chains [94–96], quantum magnets [97] and circuit quantum eletrodynamics [98, 99]. Recently, an experimental realisation of the model using two one-dimensional Josephson-coupled bosonic quasi-condensates [2, 4, 8, 100–102] opened up the possibility to study the non-equilibrium dynamics of the sine-Gordon model in a laboratory setting. In this setup, ^{87}Rb atoms are trapped in an elongated double-well potential on an atomchip, which effectively restricts their dynamics to one spatial dimension. The finite potential barrier between the wells induces tunnelling between the one-dimensional condensates in the form of particle hopping, and the tunnelling strength can be tuned by adjusting the height of the barrier. The tunnelling disappears in the limit of a very high barrier, and the condensates become independent. Abruptly changing the height forces the system out of equilibrium and allows for the experimental study of the subsequent time evolution.

The coupled condensate pair can be discussed in terms of bosonisation, where the system is described by symmetric and antisymmetric collective degrees of freedom coupled together, corresponding to a Luttinger liquid (symmetric) and the sine-Gordon model (asymmetric) and their interaction [100] (c.f. App. B). Information about the tunnelling between condensates, to a first approximation, is contained in the sine-Gordon potential. As a result, the dynamics of the coupled condensate pair can be investigated via the abundant toolbox of integrable QFTs and QFTs in general.

Classical spectrum

Classically, the sine-Gordon model is defined by the action

$$\mathcal{S}_{\mathrm{sG}}^{\mathrm{cl}} = \int dt \int dx \left[\frac{1}{2}(\partial_t \varphi)^2 - \frac{1}{2}(\partial_x \varphi)^2 + \lambda \cos \beta \varphi \right] , \qquad (3.26)$$

which describes the continuum limit of a chain of torsion-coupled mathematical pendula through the angular field variable φ. It has an infinite number of vacua corresponding to the zeros of the potential $-\lambda \cos \beta \varphi$:

$$\varphi_{\mathrm{vac}}^{(n)} = \frac{2\pi}{\beta} n , \qquad n \in \mathbb{Z} , \qquad (3.27)$$

and the elementary particle excitation has a mass $\sqrt{\lambda}\beta$. Besides the elementary excitations, the equations of motion provide stable field configurations in the form of static solitons (+) and antisolitons (-) interpolating between two consecutive vacua:

$$\varphi_{\pm}(x) = \pm \frac{4}{\beta} \arctan \left(e^{\lambda \beta x} \right) \qquad (3.28)$$

with masses

$$M_{\mathrm{cl}} = \frac{8\sqrt{\lambda}}{\beta} . \qquad (3.29)$$

16

Due to the relativistic invariance of the model, moving solitons are generated via the appropriate Lorentz transformation.

The sine-Gordon model is integrable and has an infinite number of conserved charges that restrict the dynamics to a collection of tori in the phase space. As a result, the model admits spatially localised stable periodic field configurations parametrised by a continuous parameter ε called breathers:

$$\varphi_\varepsilon = \frac{4}{\beta} \arctan \left(\frac{\varepsilon}{\omega} \frac{\cos m\omega t}{\cosh m\varepsilon x} \right) \tag{3.30}$$

where $\varepsilon^2 + \omega^2 = 1$. The breather energy spectrum is a continuous function of ε:

$$m_\varepsilon = \frac{16\varepsilon\sqrt{\lambda}}{\beta} . \tag{3.31}$$

Quantum theory

The classical scalar field φ is promoted to the field operator $\hat{\varphi}$ at the quantum level. Its dynamics is governed by the Hamiltonian

$$\hat{H}_{\text{sG}} = \int dx : \left(\frac{1}{2}(\partial_t \hat{\varphi})^2 + \frac{1}{2}(\partial_x \hat{\varphi})^2 - \lambda \cos \beta\hat{\varphi} \right) : . \tag{3.32}$$

The semicolons denote normal ordering with respect to the free massless boson defined by setting $\lambda = 0$, which regulates the theory. The potential's minima correspond to the theory's infinitely degenerate vacua.

The parameter β characterises the strength of the quantum fluctuations, and depending on its value, the sine-Gordon model admits two distinct regimes. For $4\pi \leq \beta^2 < 8\pi$, the spectrum consists of solitons and antisolitons and their scattering states that repel each other. When $\beta < \sqrt{4\pi}$, the theory is in the attractive regime, and the spectrum consists of many-particle states of breathers and (anti)solitons. The spectrum of the breathers becomes discrete:

$$m_n = 2M \sin \frac{\pi\xi n}{2} , \tag{3.33}$$

where M denotes the mass of the quantum soliton. The parameter ξ is related to the coupling β through

$$\xi = \frac{\beta^2}{8\pi - \beta^2} , \tag{3.34}$$

and characterises the strength of the interactions. At $\xi = 1$, the sine-Gordon model can be mapped to a free fermion, and the inverse $1/\xi$ counts the existing breather species in the spectrum. At the limit $\xi \to 0$, the model describes a free massive boson associated with the lowest-lying breather. Choosing the mass scale to be the lightest breather mass m_1 allows for all physical parameters to be expressed in terms of m_1. As a result, the soliton mass is given by

$$M = \frac{1}{2 \sin \frac{\pi\xi}{2}} . \tag{3.35}$$

17

Integrability relates the mass scale m_1 to the dimensionful coupling constant λ [103]:

$$\lambda = \left(2\sin\frac{\pi\xi}{2}\right)^{2h-2}\frac{2\Gamma(h)}{\pi\Gamma(1-h)}\left(\frac{\sqrt{\pi}\Gamma\left(\frac{1}{2-2h}\right)m_1}{2\Gamma\left(\frac{h}{2-2h}\right)}\right)^{2-2h} \tag{3.36}$$

where

$$2h = \frac{\beta^2}{4\pi} \tag{3.37}$$

is the anomalous dimension associated with the cosine operator.

Chapter 4

Methods

In Chapter 2, we discussed the notion of quantum quenches, a simple protocol for studying the out-of-equilibrium dynamics of quantum many-body systems, where at time $t = 0$ some parameters of the system are suddenly changed, forcing it out of equilibrium. An initial state $|\Psi_0\rangle$ (usually the ground state of the Hamiltonian $\hat{H}_0$ before the quench) is then evolved in time by the Hamiltonian $\hat{H}_1$ after the quench:

$$|\Psi(t)\rangle = e^{-i\hat{H}_1 t} |\Psi_0\rangle . \tag{4.1}$$

In this context, the naturally interesting question is the time evolution of the expectation values of local observables, defined as

$$\mathcal{O}(t) = \langle \Psi(t)|\hat{\mathcal{O}}|\Psi(t)\rangle . \tag{4.2}$$

However, $\hat{H}_1$ is often interacting, and (4.2) can not be computed analytically exactly, requiring approximate and numerical methods.

Now we introduce some of these methods used to compute the non-equilibrium time evolution of expectation values of local operators in interacting quantum field theories (though some of these can also be applied to lattice models, here we focus on continuous theories). In Section 4.1, we start by discussing the self-consistent Gaussian approach for the (1+1)d φ^4 theory, one of the simplest ways of dealing with the interactions. Then, we discuss another semi-classical approach, the truncated Wigner approximation in Section 4.2. Finally, in Section 4.3, we consider various versions of the truncated Hamiltonian approach, applicable to various physical systems, such as the φ^4 theory and the sine-Gordon model.

4.1 The self-consistent Gaussian method

One of the simplest ways of approximating (4.2) in interacting field theories is provided by the self-consistent Gaussian (SCA) approximation, also called the mean-field or Hartree-Fock approach. The method can be formulated in many equivalent ways and has been widely used to study dynamics in numerous models [104–110]. In terms of perturbation theory, the SCA amounts to dropping all skeleton diagrams contributing to the correlation functions, apart from the one-loop diagram. Alternatively, approximating the system state

with some Gaussian wavefunction that satisfies Wick's theorem for all times t results in the same dynamics.

For the φ^4 theory, the SCA was developed by Cardy and Sotiriadis [111] to study the non-equilibrium dynamics of the propagator following quantum quenches by initiating the system in the ground state of

$$\hat{H}_0 = \int_0^L dx : \left[\frac{1}{2}(\partial_t\hat{\varphi})^2 + \frac{1}{2}(\partial_x\hat{\varphi})^2 + \frac{1}{2}m_0^2\hat{\varphi}^2 + \frac{\lambda_0}{4!}\hat{\varphi}^4\right] : \qquad (4.3)$$

and at $t = 0$ changing the mass and coupling parameters $(m_0, \lambda_0) \to (m, \lambda)$. The system is subject to non-equilibrium time evolution governed by the post-quench Hamiltonian

$$\hat{H} = \int_0^L dx : \left[\frac{1}{2}(\partial_t\hat{\varphi})^2 + \frac{1}{2}(\partial_x\hat{\varphi})^2 + \frac{1}{2}m^2\hat{\varphi}^2 + \frac{\lambda}{4!}\hat{\varphi}^4\right] : . \qquad (4.4)$$

The main idea behind their formulation of the method is to replace the quartic interaction in the Hamiltonian (4.4) with a Gaussian approximation:

$$\hat{\varphi}^4 \to 6\left\langle\hat{\varphi}^2\right\rangle\hat{\varphi}^2 - 3\left\langle\hat{\varphi}^2\right\rangle^2 \qquad (4.5)$$

which is equivalent to dropping the fully connected part $: \hat{\varphi}^4 :$. Since the second term is just a constant shift in energy, it does not contribute to the time evolution and can also be dropped. The replacement of the interactions by a mean-field term is eventually justified in the large-N limit of the linear σ-model, a generalisation of the φ^4 theory to an N-component field, where the system becomes integrable, and the dynamics are described exactly by the SCA. In 4.5, the first term corresponds to a shift in the particle mass, essentially reducing the dynamics to that of a massive Klein-Gordon model with a self-consistently determined, time-dependent particle mass. Naively, it is given by the self-consistent gap equation, computed from the two-point correlation function:

$$m_{\text{eff}}^2(t) = m^2 + \frac{\lambda}{2}\sum_k \left\langle\hat{\varphi}_k(t)\hat{\varphi}_{-k}(t)\right\rangle . \qquad (4.6)$$

However, Eq. (4.6) suffers from ultraviolet divergences due to the infinite sum on the right-hand side, and the actual effective mass can be defined through a renormalisation procedure, leading to the renormalised gap equation:

$$m_{\text{eff}}^2(t) = m^2 + \frac{\lambda}{2}\sum_k \left(\left\langle\hat{\varphi}_k(t)\hat{\varphi}_{-k}(t)\right\rangle - \frac{1}{2\omega_k}\right) . \qquad (4.7)$$

with $\omega_k^2 = m^2 + k^2$. This procedure is equivalent to normal ordering with respect to the bosonic modes corresponding to mass m.

The mean field approximation to the time evolution only takes into account the lowest-order quantum correlations and reduces the dynamics to Gaussian time evolution of free bosonic modes with a self-consistently determined effective mass. As a result, the scattering of particles with different momenta is disregarded, and the SCA can not account for relaxation phenomena originating from the energy exchange between different momentum modes.

Such an approach is equivalent to modelling the non-integrable system via the closest (Gaussian) integrable theory, and as such, it is expected to reproduce some of the generalities of the non-integrable dynamics, particularly in the weakly interacting regime when λ is small.

Computation of the time evolution of the correlator $\langle \varphi_k(t) \hat{\varphi}_{-k} \rangle$ in the self-consistent approximation can be obtained by solving the Gaussian equations of motion containing a time-dependent mass term, defined through (4.5):

$$\partial_t^2 \hat{\varphi}_k + \omega_k^2(t) \hat{\varphi}_k = 0, \qquad \omega_k^2(t) = k^2 + m_{\text{eff}}^2 \qquad (4.8)$$

and self-consistently determining $m_{\text{eff}}(t)$ from the condition (4.7). This can be done by substituting the ansatz

$$\hat{\varphi}_k \sim \frac{1}{\sqrt{2\Omega_k(t)}} \exp\left[-i \int_0^t dt' \Omega_k(t')\right] \qquad (4.9)$$

into the EOM (4.8) and determining the frequencies Ω_k for all k using the initial conditions

$$\Omega_k(0) = \omega_k(0) \qquad \dot{\Omega}_k(0) = 0. \qquad (4.10)$$

The correlator $\langle \hat{\varphi}^2(t) \rangle$ and the effective mass m_{eff}^2 can be obtained straightforwardly.

Though analytically tedious, this procedure can be easily implemented numerically by discretising the (t, k)-space and solving the equations of motion by the following iterative procedure [111]:

1. Construct the time-dependent mode frequency function $\Omega_k(t)$ for every mode k from

$$\frac{\ddot{\Omega}_k}{2\Omega_k} - \frac{3}{4}\left(\frac{\dot{\Omega}_k}{\Omega_k}\right)^2 + \Omega_k^2 = \omega_k(t)^2. \qquad (4.11)$$

   with the initial condition

$$\Omega_k(0) = \omega_k(0) \qquad \dot{\Omega}_k(0) = 0. \qquad (4.12)$$

   where

$$\omega_k(t) = \sqrt{m_{\text{eff}}^2(t) + k^2}. \qquad (4.13)$$

2. Compute $\langle \hat{\varphi}_k(t) \hat{\varphi}_{-k}(t) \rangle$ for every k from

$$\langle \hat{\varphi}_k(t) \hat{\varphi}_{-k}(t) \rangle = \frac{1}{\Omega_k(t)}\left[\frac{\omega_k(0)^2 + \omega_{0k}^2}{2\omega_k(0)\omega_{0k}} + \frac{\omega_k(0)^2 - \omega_{0k}^2}{2\omega_k(0)\omega_{0k}} \cos\left(2\int_0^t dt' \Omega_k(t')\right)\right], \quad (4.14)$$

   where $\omega_{0k}^2 = m_0^2 + k^2$.

3. The effective mass $m_{\text{eff}}^2(t)$ can be obtained from the gap equation

$$m_{\text{eff}}^2(t) = m^2 + \frac{\lambda}{2}\sum_k \left(\langle \hat{\varphi}_k(t) \hat{\varphi}_{-k}(t) \rangle - \frac{1}{2\omega_k(0)}\right). \qquad (4.15)$$

4. Move to the next time step $t \to t + dt$.

In a finite volume L, using periodic boundary conditions, the allowed Fourier modes become a discrete set: $k = 2\pi n/L$ with $n \in \mathbb{Z}$ which can simply be made finite by introducing an upper cutoff $N_{\max}$ so that $|n| \leq N_{\max}$. In our later computations (see Chapter 6), $N_{\max}$ is chosen such that results converge. However, choosing the cutoff too high introduces instabilities and must be avoided. Moreover, the time-step parameter dt has to be tuned so that results no longer depend on its value.

4.2 The truncated Wigner approximation

As discussed in the previous section, the self-consistent Gaussian (or mean-field) approach fails to accurately describe the out-of-equilibrium dynamics as it neglects the energy exchange between particles with different momenta that would result in the relaxation of expectation values of observables. Indeed, it is a general fact that semi-classical approximations can not reproduce the exact time evolution of strongly coherent quantum many-body systems. However, they are expected to provide accurate results whenever the interactions and coherence between the degrees of freedom are weak, close to the classical limit of the theory.

In a general out-of-equilibrium setting, the time evolution of expectation values of local operators can be expressed via the Keldysh path integral formalism [112, 113], which can be systematically expanded in the quantum fluctuations to compute (in theory) the time evolution to arbitrary precision. The lowest-order expansion is usually referred to as the truncated Wigner approximation (TWA) [112–114], which is a widely used semi-classical approximation for computing non-equilibrium time evolution in interacting quantum many-body systems. It has been previously argued that it provides a good description of the dynamics of interacting field theories, such as the sine-Gordon model [115]. However, its accuracy is hard to control, requiring careful validation against other, more controlled methods whenever available.

Now we turn to discuss the implementation of the TWA for 1-dimensional relativistic field theories, focusing on the (1+1)d φ^4 model first in detail, then moving on to the application of TWA for the sine-Gordon model, only highlighting the differences where necessary. In our subsequent work presented in Chapters 6 and 8, the TWA was implemented and applied to the dynamics by Izabella Lovas [115].

4.2.1 Lattice regularisation

The TWA is formulated using the lattice regularised form of the φ^4 Hamiltonian:

$$\hat{H}_{\text{latt}} = \sum_{j=1}^{N_s} \left(\frac{\hat{\pi}_j^2 + (\hat{\varphi}_j - \hat{\varphi}_{j-1})^2}{2a} + \frac{m^2 a}{2} \hat{\varphi}_j^2 + \frac{\lambda a}{4!} : \hat{\varphi}_j^4 : \right) , \tag{4.16}$$

where N_s denotes the number of lattice sites, $a = L/N_s$ is the lattice constant, and the operators $\hat{\varphi}_j$ and $\hat{\pi}_j = a\partial_t \hat{\varphi}_j$ satisfy canonical commutation relations

$$[\hat{\varphi}_j, \hat{\pi}_{j'}] = i\delta_{jj'} . \tag{4.17}$$

Here, normal ordering of the operator $: \hat{\varphi}_j^4 :$ is done with respect to the (post-quench) mass m. Setting $\lambda = 0$, the quadratic part of (4.16) can be diagonalised via the Fourier transform

$$\hat{\varphi}_k = \frac{1}{\sqrt{N_s}} \sum_j e^{-ijak} \hat{\varphi}_j \,, \quad \hat{\pi}_k = \frac{1}{\sqrt{N_s}} \sum_j e^{-ijak} \hat{\pi}_j \,, \tag{4.18}$$

and results in the dispersion relation

$$\omega_k^{\text{latt}} = \sqrt{\left(\frac{2}{a} \sin \frac{ka}{2} \right)^2 + m^2} \tag{4.19}$$

which reduces to the continuum relation $\omega_k = \sqrt{m^2 + k^2}$ in the limit of $k \ll 1/a$. In the vacuum, the correlators of the $\hat{\varphi}_k$ and $\hat{\pi}_k$ operators are given by

$$\langle \hat{\varphi}_k \hat{\varphi}_{k'} \rangle_{\text{vac}} = \delta_{k,-k'} \frac{1}{2a\,\omega_k^{\text{latt}}} \,,$$

$$\langle \hat{\pi}_k \hat{\pi}_{k'} \rangle_{\text{vac}} = \delta_{k,-k'} \frac{a\,\omega_k^{\text{latt}}}{2} \,. \tag{4.20}$$

Since the TWA is a semi-classical approximation, it is formulated in terms of operators that are not normal-ordered. Hence, to treat (4.16) as a semi-classical Hamiltonian, the operator $: \hat{\varphi}_j^4 :$ must be rewritten as

$$: \hat{\varphi}_j^4 := \hat{\varphi}_j^4 - \hat{\varphi}_j^2 \frac{\lambda a}{4 N_s} \sum_k \frac{1}{2a\,\omega_k^{\text{latt}}} + \text{const.}, \tag{4.21}$$

where the sum runs over momentum modes $k = 2\pi n/L$, $n = 0, \pm 1, \pm 2, ..., \pm N_s/2$, and the second term accounts for the vacuum expectation value $\langle \hat{\varphi}_k \hat{\varphi}_{k'} \rangle_{\text{vac}}$. Defining the bare mass

$$m_{\text{bare}}^2 = m^2 - \frac{\lambda}{4 N_s a} \sum_k \frac{1}{\omega_k^{\text{latt}}}, \tag{4.22}$$

the Hamiltonian (4.16) can be written in terms of non-renormalised operators:

$$H_{\text{latt}} = \sum_{j=1}^{N_s} \left(\frac{\hat{\pi}_j^2 + (\hat{\varphi}_j - \hat{\varphi}_{j-1})^2}{2a} + \frac{m_{\text{bare}}^2 a}{2} \hat{\varphi}_j^2 + \frac{\lambda a}{4!} \hat{\varphi}_j^4 \right). \tag{4.23}$$

4.2.2 Approximating the time evolution

The semi-classical TWA approximates out-of-equilibrium expectation values and correlations through phase space averages of an ensemble of classical trajectories [112, 113]. Closely related to the mean-field approximation, it approximates the time evolution by solving the classical equations of motion for the phase space coordinates $\{\varphi_j, \pi_j\}$. However, the TWA goes significantly beyond the mean field approximation by considering the quantum fluctuations in the initial state, incorporating them in the time evolution. This is done by sampling random initial coordinates $\{\varphi_j^{(0)}, \pi_j^{(0)}\}$ distributed accordingly to some relevant probability

distribution containing the quantum fluctuations of the initial state, determining the classical trajectories for these fluctuation initial conditions and averaging over this ensemble. A more formal construction of the TWA is given by a systematic expansion of the Keldysh path integral [112, 113].

To implement the TWA for the lattice Hamiltonian (4.23), it is favourable to introduce the notations $|\varphi\rangle_j$ and $|\pi\rangle_j$ for the eigenvectors of the operators $\hat{\varphi}_j$ and $\hat{\pi}_j$, respectively. That is, they are defined so they satisfy the completeness relation

$$\mathbb{I}_j = \int \frac{d\pi}{2\pi} |\pi\rangle_{j\,j}\langle\pi| = \int d\varphi \, |\varphi\rangle_{j\,j}\langle\varphi| \tag{4.24}$$

for any site j. We introduce a more compact vector notation

$$\underline{\varphi} = \{\varphi_j \,|\, j = 1, ..., N_s\} \tag{4.25}$$

for the full set of eigenvalues, with analogous notation for the eigenvalues of the canonical conjugate operators $\hat{\pi}_j$.

An initial state corresponding to the density matrix $\hat{\rho}_0$ can be characterised by the Wigner function, a quasi-probability distribution in phase space:

$$W(\underline{\varphi}, \underline{\pi}) = \frac{1}{(2\pi)^{2N_s}} \int d\underline{\varphi}' \, \langle \underline{\varphi} + \underline{\varphi}'/2| \, \hat{\rho}_0 \, |\underline{\varphi} - \underline{\varphi}'/2\rangle \, e^{-i\underline{\varphi}'\underline{\pi}}. \tag{4.26}$$

An arbitrary observable $\hat{\mathcal{O}}$ can be represented as a function over phase space coordinates similarly by its Wigner transform defined as

$$O_W(\underline{\varphi}, \underline{\pi}) = \int d\underline{\varphi}' \, \langle \underline{\varphi} - \underline{\varphi}'/2| \, \hat{\mathcal{O}} \, |\underline{\varphi} + \underline{\varphi}'/2\rangle \, e^{i\underline{\varphi}'\underline{\pi}}. \tag{4.27}$$

As a result, the TWA is formulated in terms of the phase space distribution W and the phase space functions O_W. Quantum fluctuations of the initial state are incorporated by sampling random initial coordinates $\{\underline{\varphi}^0, \underline{\pi}^0\}$ according to the Wigner quasi-distribution W. Time evolution is computed by solving the classical equations of motion

$$\begin{aligned}
\partial_t \pi_j &= -\frac{1}{a}(\varphi_{j+1} + \varphi_{j-1} - 2\varphi_j) - m_{\text{bare}}^2 a\, \varphi_j - \frac{\lambda a}{6}\varphi_j^3\,, \\
\partial_t \varphi_j &= \frac{1}{a}\pi_j\,,
\end{aligned} \tag{4.28}$$

for the classical trajectories $\{\underline{\varphi}(t), \underline{\pi}(t)\}$, and obtaining the contribution of these trajectories to the expectation value of $\hat{\mathcal{O}}$ by substituting $\{\underline{\varphi}(t), \underline{\pi}(t)\}$ into O_W. The TWA expectation value $\langle\hat{\mathcal{O}}\rangle_{TW}$ is computed by averaging over a large ensemble of initial states $\{\underline{\varphi}^{(0)}, \underline{\pi}^{(0)}\}$:

$$\langle\hat{\mathcal{O}}\rangle_{\text{TW}}(t) = \iint d\underline{\varphi}^{(0)} d\underline{\pi}^{(0)} \, W(\underline{\varphi}^{(0)}, \underline{\pi}^{(0)}) \, O_W(\underline{\varphi}(t), \underline{\pi}(t))\,, \tag{4.29}$$

which expresses the time-evolved expectation value of the observable as a phase space average over classical trajectories, distributed according to the Wigner quasi-probability distribution of the initial state.

The TWA is first validated by performing mass quenches with the quartic coupling set to zero, where the method is exact, similar to the SCA.

4.2.3 TWA for the sine-Gordon model

The TWA for the sine-Gordon model time evolution is implemented similarly to the (1+1)-dimensional φ^4 theory discussed previously. Here, we restrict ourselves to pointing out the key differences and introducing the matching of observables between the lattice and continuum theories.

As discussed before in Section 3.3, the sine-Gordon model is given by the Hamiltonian

$$\hat{H}_{\text{sG}} = \int_0^L dx : \left(\frac{1}{2}(\partial_t\hat{\varphi})^2 + \frac{1}{2}(\partial_x\hat{\varphi})^2 - \lambda\cos\beta\hat{\varphi} \right) :, \tag{4.30}$$

where the theory is now formulated in a finite volume L. The TWA is implemented in terms of the lattice regularised Hamiltonian of the sine-Gordon model:

$$\hat{H}_{\text{Lat}} = \frac{a}{2}\sum_{j=1}^N \left((\partial_t\hat{\varphi}_j)^2 + \frac{(\hat{\varphi}_j - \hat{\varphi}_{j-1})^2}{a^2} \right) - \frac{\lambda a}{\mathcal{N}}\sum_{j=1}^N \cos\beta\hat{\varphi}_j, \tag{4.31}$$

where $a = L/N$ is the lattice constant and the discretised phase field $\hat{\varphi}_j$ is related to the continuum field through $\hat{\varphi}_j = \hat{\varphi}(x = aj)$. The discretised canonical momentum is defined as

$$\hat{\pi}_j = a\partial_t\hat{\varphi}_j \tag{4.32}$$

to satisfy

$$[\hat{\varphi}_j, \hat{\pi}_{j'}] = i\delta_{j,j'}. \tag{4.33}$$

The semi-classical TWA is formulated using the non-renormalised operators. The normal ordering of the cosine in Eq. (4.30) is accounted for by relating

$$\cos\beta\hat{\varphi}_i = \mathcal{N} : \cos\beta\hat{\varphi}_i :, \tag{4.34}$$

via the coefficient $\mathcal{N}$, determined from the Baker-Campbell-Hausdorff formula [115]:

$$\mathcal{N} = \exp\left(-\frac{\pi h}{N}\right) \prod_{n=1}^{N/2-1} \exp\left(-\frac{2\pi h}{N\sin\frac{\pi n}{N}}\right). \tag{4.35}$$

In the continuum theory, the two-point function

$$\langle\hat{\varphi}_k\hat{\varphi}_{-k}\rangle \tag{4.36}$$

has an expectation value

$$\langle 0|\hat{\varphi}_k\hat{\varphi}_{-k}|0\rangle = \frac{1}{4\pi k}, \tag{4.37}$$

that can be matched with the TWA definition by defining the Fourier transform of the discredited fields $\hat{\varphi}_j$ as

$$\hat{\varphi}_{k\neq 0} = \frac{1}{N}\sum_{j=1}^N e^{i\frac{2\pi}{N}kj}\hat{\varphi}_j \tag{4.38}$$

and computing the vacuum expectation value of their correlator:

$$\langle 0|\hat{\varphi}_k\hat{\varphi}_{-k}|0\rangle = \frac{1}{4N\sin(\pi k/N)}\,, \tag{4.39}$$

which in the continuum limit $N \to \infty$ reduces to the definition used in the continuum correlator (4.36).

As discussed before in this section, the time evolution of expectation values of observables in the TWA is computed through an ensemble of solutions of the classical equations of motion, averaged over the fluctuating initial state distributed according to the Wigner quasi-probability distribution given by

$$W(\underline{\varphi},\underline{\pi}) = \frac{1}{(2\pi)^{2N}}\int d\underline{\varphi}'\,\langle\underline{\varphi}-\underline{\varphi}'/2|\hat{\rho}|\underline{\varphi}+\underline{\varphi}'/2\rangle\,e^{-i\underline{\varphi}'\cdot\underline{\pi}}\,. \tag{4.40}$$

Here we introduced the same vector notation as before

$$\underline{\varphi} = \{\varphi_j|j = 1, ..., N\}\,, \quad \underline{\pi} = \{\pi_j|j = 1, ..., N\}\,. \tag{4.41}$$

for the phase space coordinates, and $\hat{\rho}$ is the density operator corresponding to a given initial state $|\Psi_0\rangle$ of the system:

$$\hat{\rho}_{\Psi_0} = |\Psi_0\rangle\,\langle\Psi_0|\,. \tag{4.42}$$

The Wigner function is usually positive semi-definite, allowing for the proper generation of random initial conditions $\{\underline{\varphi},\underline{\pi}\}$ distributed according to W. Averaging over these fluctuating initial conditions can be obtained by Monte Carlo simulations of the classical trajectories. However, in the case of negative regions occurring in W, the method becomes less efficient due to the emergent sign problem.

4.3 The truncated Hamiltonian approach

In contrast to semi-classical methods, the truncated Hamiltonian approaches (THA) provide a more controlled approach, a family of non-perturbative methods used to study strongly interacting quantum field theories. Originally called the truncated conformal space approach (TCSA), it was developed by Yurov and Zamolodchikov [116] to study relevant perturbations of conformal field theories numerically. The method can be considered a field theoretical version of the Rayleigh-Ritz variational method used in ordinary quantum mechanics. The main idea behind the THA is to put the system in finite volume, which discretises the spectrum. As a next step, applying a global (upper) energy truncation restricts the Hilbert space to some low-energy subspace, and the Hamiltonian and observables can be represented by finite matrices that are easily diagonalisable. The finite matrix formalism also enables studying the (non-perturbative) non-equilibrium time evolution of perturbed field theories via appropriate exponentiation of the Hamiltonian, and has been applied in various scenarios and systems [115, 117–122]. The THA results however depend on the system size, and differ from the exact results by the so-called truncation error. These errors usually tend to zero as the energy cutoff is increased, which can be computationally expensive, requiring other procedures, such as the leading order renormalisation group improvement [82, 83].

A general requirement of the THA is to have an eigenbasis of a finite volume (unperturbed) Hamiltonian for which the spectrum and eigenstates are known, together with the corresponding matrix elements of the perturbing Hamiltonian of interest. Consequently, there are various versions of the THA differentiated by their computational basis: in their seminal work [116], Yurov and Zamolodchikov used the conformal basis to express the perturbed Hamiltonian and compute the spectrum, which is referred to as the truncated conformal space approach (TCSA). In the work [123], the authors used the free massive fermion basis for the THA, which is subsequently called the truncated free fermion space approach (TFFSA). Similarly, THA versions using massive [81–83, 89] and massless [124] free bosonic eigenstates as a basis are also available. The method has been used extensively to study non-equilibrium dynamics of strongly interacting many-body systems [115, 117–122], as well as boundary [125, 126] and defect problems [127][1]. In the work [81], the THA was also extended to dimensions higher than one.

In the following, we discuss the implementation of the THA for two interacting (1+1)-dimensional quantum field theories. In Section 4.3.1, we focus on the φ^4 theory both in $\mathbb{Z}_2$-symmetric and $\mathbb{Z}_2$-broken phase, where the THA is built upon the Fock space of the free massive boson. In the symmetry-broken phase (Section 4.3.1), the THA is implemented using a mini-superspace treatment of the zero mode [83]. In Section 4.3.2, we discuss the TCSA built upon the free massless boson basis and the mini-superspace-based THA to study the dynamics of the sine-Gordon model. In both cases, we start by considering the finite volume theory and then discuss the truncation protocols characteristic of the appropriate THA version. A number of technical details are relegated to Appendix A.

4.3.1 THA for the (1+1)d φ^4 theory

The $\mathbb{Z}_2$-symmetric phase

The (1+1)d φ^4 theory in a finite volume L is given by the Hamiltonian

$$\hat{H} = \int_0^L dx : \left[\frac{1}{2}(\partial_t\hat{\varphi})^2 + \frac{1}{2}(\partial_x\hat{\varphi})^2 + \frac{1}{2}m^2\hat{\varphi}^2 + \frac{\lambda}{4!}\hat{\varphi}^4 \right] : \qquad (4.43)$$

where the free part is the massive Klein-Gordon Hamiltonian

$$\hat{H}_{\mathrm{KG}}^m = \int_0^L dx : \left[\frac{1}{2}(\partial_t\hat{\varphi})^2 + \frac{1}{2}(\partial_x\hat{\varphi})^2 + \frac{1}{2}m^2\hat{\varphi}^2 \right] : \qquad (4.44)$$

describing a free boson with mass m through the scalar field $\hat{\varphi}$ and canonical momentum

$$\hat{\pi} = \partial_t\hat{\varphi} \qquad (4.45)$$

satisfying the usual equal-time canonical commutation relation

$$[\hat{\varphi}(t,x), \hat{\pi}(t,y)] = i\delta(x-y) . \qquad (4.46)$$

---

[1]For a recent review c.f. [128]

We use periodic boundary conditions $\hat{\varphi}(t, x + L) = \hat{\varphi}(t, x)$. As a result, the Klein-Gordon spectrum is discretised, and the allowed Fourier modes are integer multiples of $2\pi/L$. Regularisation of the Hamiltonians is done by normal ordering with respect to the free boson modes with mass m, denoted by the semicolons. From now on, we focus on the $\mathbb{Z}_2$−symmetric phase, characterised by $m^2 > 0$ and employ units in which $m = 1$ and define the dimensionless volume parameter $l = Lm$ and measure the quartic coupling λ in units of m^2.

The finite volume formulation of the theory is a general requirement of the truncated Hamiltonian approach and results in a discrete spectrum. Though it is possible to directly formulate the theory in infinite volume through light-cone quantisation [129,130], the method outlined here is better-tailored to studying the dynamics of the system, and although it limits us to work in finite volume, it is adequate for our later calculations.

As a next step, a UV cutoff is introduced to limit the dimension of the Hilbert space to a finite size, allowing for a finite matrix representation of the Hamiltonians and observables. Here we work on the eigenbasis of the massive Klein-Gordon Hamiltonian corresponding to a mass $m = 1$, and we parametrise the volume L via the dimensionless parameter $l = Lm$. Since the Hamiltonian (4.43) is translationally invariant, the Hilbert space can be restricted to the zero-momentum subspace. As a result, the energy cutoff Λ can be parameterised as

$$\frac{\Lambda}{m} = 4\pi n_{\max}/l \tag{4.47}$$

where $n_{\max}$ is the quantum number of the maximum momentum mode that can be excited in the massless limit. Keeping only the low-lying Klein-Gordon eigenstates as a basis reduces the computation of observables to simple arithmetics (for details, see Appendix A). Expectation values and eigenvalues of the truncated operators can be evaluated by manipulations of finite matrices. However, these results depend on the cutoff Λ and differ from the exact results by what is called the truncation error. Since the φ^4 theory is a relevant perturbation of the massive Klein-Gordon model, these truncation errors tend to zero as the cutoff is increased to infinity. However, increasing the cutoff is computationally expensive, warranting clever ways to increase the precision. One of the simplest approaches is the widely used leading order renormalisation group improvement, consisting of defining an effective theory by summing up the high-energy contributions and incorporating them into the running couplings of the effective theory [82]:

$$\hat{H}_{\mathrm{eff}} = \hat{H} + \kappa_0 \hat{V}_0 + \kappa_2 \hat{V}_2 + \kappa_4 \hat{V}_4 \tag{4.48}$$

where

$$\hat{V}_n = \int_0^L dx \; : \hat{\varphi}^n : \tag{4.49}$$

and the running couplings κ_n are defined to leading order as [82]

$$\kappa_0 = -\int_\Lambda^\infty \frac{dE}{E - \epsilon_*} [g_4^2 \mu_{440}(E) + g_2^2 \mu_{220}(E)]$$

$$\kappa_2 = -\int_\Lambda^\infty \frac{dE}{E - \epsilon_*} [g_4^2 \mu_{442}(E) + g_2 g_4 \mu_{422}(E)] \tag{4.50}$$

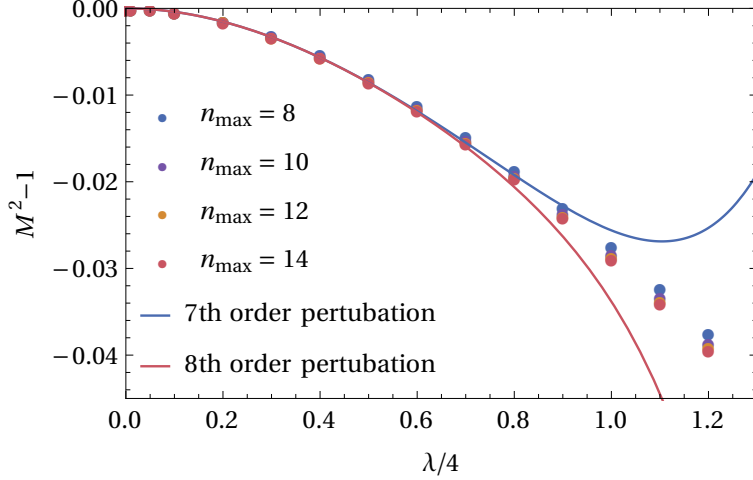$$\kappa_4 = -\int_\Lambda^\infty \frac{dE}{E - \epsilon_*} g_4^2 \mu_{444}(E)$$

Figure 4.1: The gap as a function of the quartic coupling λ for $l = 10$ in the perturbative regime using units $m = 1$, for different values of the cutoff parameter $n_{\max}$ computed using the leading order RG improvement Eq. (4.48). The solid lines show the 7th and the 8th order perturbative results [78].

where the g_n are the coupling of the $\hat{V}_n$ term corresponding to the infinite cutoff as appearing in (4.43), i.e.

$$g_2 = 0, \qquad g_4 = \frac{\lambda}{4!}, \tag{4.51}$$

ϵ_* is a reference energy [82] which we choose to be zero, and the functions determining the renormalisation group flow of the running couplings are given by [82]

$$\mu_{220}(E) = \frac{1}{\pi E^2}, \quad \mu_{422} = \frac{12}{\pi E^2}, \quad \mu_{444}(E) = \frac{36}{\pi E^2}$$

$$\mu_{440}(E) = \frac{1}{E^2} \left[\frac{18}{\pi^3} (\log E/m)^2 - \frac{3}{2\pi} \right] \tag{4.52}$$

$$\mu_{442}(E) = \frac{72 \log E/m}{\pi^2 E^2}.$$

To test the accuracy of the renormalised THA, we first compute the mass gap and compare the results to perturbation theory (3.22) [78], as demonstrated in Fig. 4.1. The correspondence between the results demonstrates the accuracy of the THA and illustrates the effectiveness of the leading order renormalisation group improvement for eliminating cutoff dependence from the spectrum.

The symmetry-broken phase

Now we turn to the symmetry-broken phase of the (1+1)d φ^4 theory, characterised by the negative sign of the mass term in the Hamiltonian. Additionally, we include a term proportional to an explicitly symmetry-breaking external field ε, which will later allow us to study the false vacuum decay in the theory:

$$\hat{H}_\varepsilon = H_{\mathrm{KG}}^m + \int dx : \left(-m^2 \hat{\varphi}^2 + \frac{g}{6} \hat{\varphi}^4 - \varepsilon \hat{\varphi} \right) :_m, \tag{4.53}$$

29

with

$$\hat{H}_{\mathrm{KG}}^m = \int dx : \left(\frac{1}{2}\hat{\pi}^2 + \frac{1}{2}(\partial_x \hat{\varphi})^2 + \frac{m^2}{2}\hat{\varphi}^2 \right) :_m \qquad (4.54)$$

denoting the Klein-Gordon Hamiltonian describing free bosons of mass m, with the canonical field satisfying the equal time canonical commutation relations

$$[\hat{\pi}(t, x), \hat{\varphi}(t, x')] = -i\delta(x - x'). \qquad (4.55)$$

The semicolons $: \cdots :_m$ denote normal ordering with respect to the free massive bosonic modes of mass m. The THA is formulated in finite volume L with periodic or antiperiodic boundary conditions. We work in units $m = 1$, and therefore, the system can be parametrised by the dimensionless combination of parameters

$$l = mL, \quad \bar{g} = \frac{g}{m^2} \quad \text{and} \quad \bar{\varepsilon} = \frac{\varepsilon}{m^2}. \qquad (4.56)$$

In finite volume L, the Klein-Gordon Hamiltonian takes the form

$$\hat{H}_{\mathrm{KG}}^m(L) = \int_0^l dx : \left(\frac{1}{2}\hat{\pi}^2 + \frac{1}{2}(\partial_x \hat{\varphi})^2 + \frac{m^2}{2}\hat{\varphi}^2 \right) :_{m,L} + E_0(l), \qquad (4.57)$$

where the semicolons $: \cdots :_{m,L}$ (with an additional subscript L) denote normal ordering with respect to the free bosonic modes of mass m defined in a finite volume L. (c.f. App. A) The last term is a shift in the ground state energy density, defined as [89]

$$E_0(l) = \int_{-\infty}^{\infty} \frac{d\theta}{2\pi} \cosh\theta \log\left(1 - e^{-l\cosh\theta}\right). \qquad (4.58)$$

The Hamiltonian of the perturbed theory in finite volume can be expressed as

$$\hat{H}_\varepsilon(L) = \hat{H}_{\mathrm{KG}}^m(L) + \int_0^l dx : \left[g_0(l) + g_2(l)\hat{\varphi}^2 + g_4(l)\hat{\varphi}^4 - \bar{\varepsilon}\hat{\varphi} \right] :_{m,L}. \qquad (4.59)$$

Here, the couplings $g_i(l)$ are related to the infinite volume couplings of the theory (defined in (4.53)) as [89]

$$g_0(l) = -m^2 z^\pm(l) - m^2 \frac{3\log 2}{8\pi} + \frac{g}{2}\tilde{z}^\pm(l)^2, \qquad g_2(l) = g\tilde{z}^\pm(l) - m^2, \qquad g_4 = \frac{g}{6} \qquad (4.60)$$

together with

$$z^+(l) = \int_0^\infty \frac{d\theta}{\pi} \frac{1}{e^{l\cosh\theta} - 1}, \qquad z^-(l) = 2z^+(2l) - z^+(l), \qquad \tilde{z}^\pm(l) = z^\pm(l) + \frac{\log 2}{4\pi} \qquad (4.61)$$

where the superscript $\pm$ refers to periodic (+) and antiperiodic (-) boundary conditions $\hat{\varphi}(x + L) = \pm\hat{\varphi}(x)$, respectively. When the symmetry is spontaneously broken, the Hilbert space of the theory consists of states corresponding to particle excitations above the degenerate vacua. Consequently, in order to develop an effective version of the THA, it is crucial to select a variational basis that qualitatively reflects the physical properties of the vacuum

30

structure of the theory. Therefore, we implement the so-called *mini-superspace* approach, consisting of separating and pre-diagonalising the zero mode of the field to take into account the main effect of the symmetry breaking:

$$\hat{\varphi}(x) = \hat{\varphi}_0 + \tilde{\varphi}(x), \quad \hat{\varphi}_0 = \frac{1}{L} \int_0^L dx \hat{\varphi}(x) \tag{4.62}$$

where the zero (homogeneous) mode is denoted by $\hat{\varphi}_0$, while the non-zero modes (inhomogeneities) are contained in $\tilde{\varphi}(x)$. The Hilbert space can be separated accordingly by writing

$$\mathcal{H} = \mathcal{H}^{\mathrm{mini}} \otimes \tilde{\mathcal{H}}, \tag{4.63}$$

resulting in a factorised form of the Hamiltonian (4.59):

$$\hat{H}_\varepsilon = \tilde{H}_{\mathrm{KG}}^m + H_\varepsilon^{\mathrm{mini}} +$$
$$\int_0^L dx \left[g_0 + g_2 : \tilde{\varphi}(x)^2 : + g_4 \left(: \tilde{\varphi}(x)^4 : + 6 : \tilde{\varphi}(x)^2 : \hat{\varphi}_0^2 + 4 : \tilde{\varphi}(x)^3 : \hat{\varphi}_0 \right) \right] \tag{4.64}$$

with the mini-superspace Hamiltonian governing the zero mode in the single-mode limit written as

$$\hat{H}_\varepsilon^{\mathrm{mini}} = L \left[\frac{1}{2} : \hat{\pi}_0^2 : + \frac{m^2}{2} : \hat{\varphi}_0^2 : + g_2 : \hat{\varphi}_0^2 : + g_4 : \hat{\varphi}_0^4 : - \varepsilon : \hat{\varphi}_0 : \right]. \tag{4.65}$$

Here, $\tilde{H}_{\mathrm{KG}}^m$ is the free massive Klein-Gordon Hamiltonian with the zero mode subtracted, and $\hat{\pi}_0$ is the zero mode conjugate momentum satisfying

$$[\hat{\pi}_0, \hat{\varphi}_0] = i. \tag{4.66}$$

Also, given that the allowed Fourier modes of the field $\hat{\varphi}$ in the case of antiperiodic boundary condition are $\pm \frac{1}{2} \frac{2\pi}{l}, \pm \frac{3}{2} \frac{2\pi}{l}, \pm \frac{5}{2} \frac{2\pi}{l}, \ldots$, the mini-superspace approach is only necessary in the case of periodic boundary conditions.

The matrix elements of the Hamiltonian (4.64) can be explicitly calculated on the Fock space of the free Klein-Gordon model of mass m in finite volume L with (anti)periodic boundary conditions. The space is made finite by introducing a UV cutoff in both $\mathcal{H}_{\mathrm{mini}}$ and $\tilde{\mathcal{H}}$. In the mini-superspace, this is carried out by numerically diagonalising $\hat{H}_{\varepsilon=0}^{\mathrm{mini}}$ and retaining a sufficient number of low-lying eigenstates so that the energy eigenvalues kept can be considered numerically exact. The space of the non-zero modes $\tilde{\mathcal{H}}$ decomposes into sectors of finite total momentum. We only kept the sector with zero total momentum in our subsequent calculations. As a result, the UV cutoff for the non-zero Hilbert space can be parametrised as previously (4.47):

$$\frac{\Lambda}{m} = \frac{4\pi n_{\mathrm{max}}}{l}, \tag{4.67}$$

where $n_{\mathrm{max}} \in \mathbb{Z}^+$ is a dimensionless number, which can be interpreted as the largest momentum mode present in the theory in the limit of zero mass m. The Hamiltonian and other observables are finite matrices on the truncated Hilbert space. However, expectation values

of observables and the spectrum still depend on the value of Λ and, therefore, differ from the exact results by the truncation error. The leading order contribution to the truncation error can be eliminated by appropriate renormalisation of the Hamiltonian [83]:

$$\hat{H}_\varepsilon^{\mathrm{RG}} = \hat{H}_\varepsilon + \int_0^L dx \left[\kappa_0 + \kappa_2 : \tilde{\varphi}(x)^2 : + \kappa_4 \left(: \tilde{\varphi}(x)^4 : + 6 : \tilde{\varphi}(x)^2 : \hat{\varphi}_0^2 + 4 : \tilde{\varphi}(x)^3 : \hat{\varphi}_0 \right) \right] \quad (4.68)$$

where the κ_n are given by the formulae (4.50)-(4.52). However, the zero-mode part of the Hamiltonian can be considered numerically exact by construction, given that the zero-mode UV cutoff is chosen sufficiently large.

4.3.2 THA for the sine-Gordon model

The sine-Gordon model gives a partial low-energy effective description to a pair of Josephson-coupled one-dimensional quasi-condensates: the antisymmetric bosonised degrees of freedom that incorporate the tunnelling between the condensates are formulated in terms of a relativistic bosonic field that obeys the sine-Gordon dynamics (see App. B). Therefore, studying the non-equilibrium time evolution of the condensate pair can be reduced to investigate that of the sine-Gordon model, for which many approaches are available, such as the truncated Wigner approach [115] or the time-dependent self-consistent Hartree Fock (mean-field) approximation [110]. Here, we discuss two different implementations of the truncated Hamiltonian approach to study the dynamics of the theory.

To start off, we briefly describe the sine-Gordon theory in finite spatial volume L. The time evolution is governed by the Hamiltonian

$$\hat{H}_{\mathrm{sG}} = \int_0^L dx : \left(\frac{1}{2}(\partial_t \hat{\varphi})^2 + \frac{1}{2}(\partial_x \hat{\varphi})^2 - \lambda \cos \beta \hat{\varphi} \right) : . \quad (4.69)$$

Here, the semi-colons denote normal ordering with respect to the modes of the compactified $\lambda = 0$ massless free boson in finite volume L, corresponding to the free part of the Hamiltonian:

$$\hat{H}_{\mathrm{FB}} = \frac{1}{2} \int_0^L dx : \left[(\partial_t \hat{\varphi})^2 + (\partial_x \hat{\varphi})^2 \right] :, \quad (4.70)$$

where the phase field $\hat{\varphi}$ is defined mod 2π. In the condensate literature, (4.70) corresponds to an infinite barrier between the two condensates, with zero tunnelling rate between them. The value of λ in (4.69) can be determined in relation to the mass of the lightest breather m_1 (for details about the sine-Gordon spectrum see Section 3.3) [103]:

$$\lambda = \left(2 \sin \frac{\pi \xi}{2} \right)^{2h-2} \frac{2\Gamma(h)}{\pi \Gamma(1-h)} \left(\frac{\sqrt{\pi} \Gamma \left(\frac{1}{2-2h} \right) m_1}{2\Gamma \left(\frac{h}{2-2h} \right)} \right)^{2-2h} \quad (4.71)$$

where

$$\xi = \frac{\beta^2}{8\pi - \beta^2}, \quad (4.72)$$

and

$$2h = \frac{\beta^2}{4\pi} \quad (4.73)$$

32

is the anomalous dimension of the cosine operator. In the following, we parametrise the Hamiltonian and physical parameters in $m_1 = 1$ units.

Considering the cosine potential, the sine-Gordon field $\hat{\varphi}$ represents an angular variable of period $\frac{2\pi}{L}$. Therefore, it is natural to choose quasi-periodic boundary conditions in the form

$$\hat{\varphi}(x + L, t) = \hat{\varphi}(x, t) + \frac{2\pi}{\beta}m, \tag{4.74}$$

where $m \in \mathbb{Z}$ is the so-called winding number (topological charge). In the following, we only need the sector corresponding to zero topological charge $m = 0$, so Eq. (4.74) reduces to the ordinary periodic boundary condition of the field.

Expanding the boson field $\hat{\varphi}$ in (4.70) in Fourier modes

$$\hat{\varphi}(x, t) = \hat{\varphi}_0 + \frac{1}{L}\hat{\pi}_0 t + \frac{i}{\sqrt{4\pi}}\sum_{k \neq 0}\frac{1}{k}\left[a_k e^{i\frac{2\pi}{L}k(x-t)} + \bar{a}_k e^{-i\frac{2\pi}{L}k(x+t)}\right], \tag{4.75}$$

results in the second-quantised form of the free massless boson Hamiltonian (4.70)

$$\hat{H}_{\mathrm{FB}} = \frac{2\pi}{L}\left(\frac{\hat{\pi}_0^2}{4\pi} + \sum_{k>0}a_{-k}a_k + \sum_{k>0}\bar{a}_{-k}\bar{a}_k - \frac{1}{12}\right). \tag{4.76}$$

with the zero mode of the field $\hat{\varphi}_0$ and the zero mode of the canonical conjugate momentum $\hat{\pi}_0$:

$$\hat{\pi}(x, t) = \partial_t\hat{\varphi}(x, t); \quad \hat{\pi}_0 = \int_0^L dx\,\hat{\pi}(x, t) \tag{4.77}$$

satisfying

$$[\hat{\varphi}_0, \hat{\pi}_0] = i. \tag{4.78}$$

The a_k and $\bar{a}_k$ are the left and right-moving canonical bosonic annihilation (creation) operators with positive (negative) momentum k, respectively, that satisfy the canonical commutation relations

$$[a_k, a_l] = [\bar{a}_k, \bar{a}_l] = k\delta_{k+l,0}. \tag{4.79}$$

As a result, the sine-Gordon Hamiltonian (4.69) takes the form

$$\hat{H}_{\mathrm{sG}} = \frac{2\pi}{L}\left(\frac{\hat{\pi}_0^2}{4\pi} + \sum_{k>0}a_{-k}a_k + \sum_{k>0}\bar{a}_{-k}\bar{a}_k - \frac{1}{12}\right) - \frac{\lambda}{2}\int_0^L : \left(e^{i\beta\hat{\varphi}} + e^{-i\beta\hat{\varphi}}\right) : . \tag{4.80}$$

Truncated conformal space approach (TCSA)

The usual formulation of the truncated Hamiltonian approach (THA) to studying the spectrum and time evolution of the sine-Gordon model is given by truncated conformal space approach (TCSA) [115, 124, 131, 132]. It uses the eigenstates of the massless free boson in finite volume L as a discrete variational basis, truncated by a UV energy cutoff to reduce the computation of the spectrum and the time evolution of expectation values of observables to simple finite matrix manipulation. Similarly to the THA discussed in Section 4.3.1, the results provided by the TCSA are subject to truncation errors, leading to deviations from the

exact results. For relevant perturbations such as the cosine potential appearing in 4.80, the truncation errors tend to zero as the energy cutoff increases. The convergence of the TCSA depends on the conformal weight 4.73 of the perturbing operator and can be improved by applying appropriate renormalisation group methods [133–135]. However, while powerful in general, we found that these do not alter the results of our numerical simulations, nor do they improve the rate of convergence with respect to the cutoff.

As already mentioned, the standard TCSA is built upon the Hilbert space of the free massless boson in a finite volume L, consisting of Fock modules $\mathcal{F}_\nu$:

$$\mathcal{H}_{\mathrm{FB}} = \bigoplus_{\nu \in \mathbb{Z}} \mathcal{F}_\nu, \tag{4.81}$$

with each Fock module

$$\mathcal{F}_\nu = \left\{ |\psi\rangle = \prod_{k>0} a_{-k}^{r_k} \bar{a}_{-k}^{\bar{r}_k} |\nu\rangle \,\middle|\, r_k, \bar{r}_k \in \mathbb{N}^+ \right\} \tag{4.82}$$

constructed upon the zero mode plain wave basis

$$|\nu\rangle = e^{i\nu\beta\hat{\varphi}_0} |0\rangle. \tag{4.83}$$

The Hilbert space can be further deconstructed into different sectors of finite momentum $s \in \mathbb{Z}$:

$$\mathcal{F}_\nu = \bigoplus_{s \in \mathbb{Z}} \mathcal{F}_\nu^{(s)} \tag{4.84}$$

where the module

$$\mathcal{F}_\nu^{(s)} = \left\{ |\psi\rangle = \prod_{k>0} a_{-k}^{r_k} \bar{a}_{-k}^{\bar{r}_k} |\nu\rangle \,\middle|\, \sum k r_k - \sum k \bar{r}_k = s \right\}, \tag{4.85}$$

corresponds to free many-boson states with total spatial momentum $p = \frac{2\pi s}{L}$. In our following calculations, we only study homogeneous quantum quenches, and therefore we can restrict ourselves to work within a single momentum sector of $s = 0$.

As a next step, the Hilbert space 4.81 is truncated by imposing an upper energy cutoff e_{cut}, limiting the truncated Hilbert space to a finite number of low-energy free boson eigenstates [124]:

$$\mathcal{H}_{\mathrm{FB}}^{\mathrm{trun.}} = \mathrm{span}\left\{ \prod_{k>0} a_{-k}^{r_k} \bar{a}_{-k}^{\bar{r}_k} |\nu\rangle \,\middle|\, \frac{(\nu\beta)^2}{4\pi} + \sum_{k>0} k(r_k + \bar{r}_k) < e_{\mathrm{cut}} \right\}. \tag{4.86}$$

Though effective for large values of β, the above truncation procedure has the disadvantage that in the semi-classical limit corresponding to small β, it includes a large number of Fock modules, limiting its effectiveness in the experimentally relevant parameter regime.

The mini-superspace-based truncated Hamiltonian approach (MSTHA)

To improve on the procedure outlined in the previous section, it is favourable to decompose the bosonic field $\hat{\varphi}$ into homogeneous (zero mode) and inhomogeneous (non-zero modes, a.k.a. oscillator modes) parts:

$$\hat{\varphi}(x,t) = \hat{\varphi}_0(t) + \tilde{\varphi}(x,t). \tag{4.87}$$

Omitting the contribution coming from the oscillator modes reveals the single-mode dynamics of the sine-Gordon model describing a quantum pendulum (for details on the volume dependence, refer to App. A):

$$\hat{H}_{\text{QP}} = \frac{1}{2L}\hat{\pi}_0^2 - \lambda L \left(\frac{2\pi}{L}\right)^{2h} \cos(\beta\hat{\varphi}_0).$$ (4.88)

Accordingly, the full model containing the zero mode and the oscillator modes describes a quantum pendulum coupled to a set of non-linearly interacting phononic degrees of freedom:

$$\hat{H}_{\text{sG}} = \frac{1}{2}\int_0^L : \left[(\partial_t\hat{\varphi}_0)^2 + (\partial_t\hat{\tilde{\varphi}})^2 + (\partial_x\hat{\tilde{\varphi}})^2\right] : -\frac{\lambda}{2}\int_0^L dx : \left[e^{i\beta\hat{\varphi}_0}e^{i\beta\tilde{\varphi}} + e^{-i\beta\hat{\varphi}_0}e^{-i\beta\tilde{\varphi}}\right] : \quad (4.89)$$

The above decomposition is useful if we consider that in the experimentally relevant parameter regime, the inter-mode interactions are weak (β is small), and therefore, it is viable to treat the theory as a quantum pendulum weakly coupled to a set of non-linear phonons. The periodic nature of the potential and, therefore, the field is encapsulated in the zero mode, requiring precise representation of the quantum pendulum in the THA. Therefore, we first solve the zero mode dynamics numerically exactly and couple the non-zero modes to the quantum pendulum in the next step. The usefulness of this approach also becomes apparent when considering the THA as a variational method: optimizing the variational basis results in a better convergence rate, allowing for the more precise computation of the spectrum and time evolution of the expectation values of observables.

To start off, we construct the quantum pendulum quantum mechanics on the plane wave basis ($\{|\nu\rangle\}$) (4.83) with an appropriate truncation so that the diagonalised eigenvalues

$$\hat{H}_{\text{QP}}|n\rangle = \varepsilon_n|n\rangle \quad n \in \mathbb{N}$$ (4.90)

converge to the exact results. In the next step, the finite matrices of the operators $\hat{\pi}_0^2$ and $e^{\pm i\beta\hat{\varphi}_0}$ appearing in (4.88) are constructed on the truncated quantum pendulum eigenbasis $\{|n\rangle\}$. The non-zero mode part of the Hamiltonian can be easily implemented [115, 124, 131, 132] on the non-zero mode free boson basis. Using the fact that the Hamiltonian 4.80 factorises with respect to left and right moving modes, the matrix representation of the non-zero mode operators can be separately implemented in the left and right moving sectors, similarly to a previous procedure detailed in [131], reducing the memory requirement of the THA. Finally, the sine-Gordon Hamiltonian is put together from the finite matrices of zero and non-zero mode operators according to (4.80). As a result, the precision of the mini-superspace-based THA (MSTHA) is controlled via two separate truncation parameters: the zero mode cutoff n_{max} and the non-zero mode truncation ℓ_{max}:

$$\mathcal{H}_{\text{FB}}^{\text{trun.}} = \text{span}\left\{\prod_{k>0} a_{-k}^{r_k}\bar{a}_{-k}^{\bar{r}_k}|n\rangle \,\middle|\, n \leq n_{\text{max}} \text{ and } \sum_{k>0}k(r_k + \bar{r}_k) \leq \ell_{\text{cut}}\right\}.$$ (4.91)

For a given truncation ($n_{\text{max}}, \ell_{\text{max}}$), the time evolution of any initial state $|\Psi_0\rangle$

$$|\Psi(t)\rangle = e^{-i\hat{H}_{\text{sG}}t}|\Psi_0\rangle$$ (4.92)

can be straightforwardly computed by exponentiating the finite matrix of $\hat{H}_{\text{sG}}$ (4.80). Here we opt for the so-called Bessel-Chebyshev method [117, 131] and maintain its validity by monitoring the norm of the time-evolved state $|\Psi(t)\rangle$. Of course, the choice of the initial state $|\Psi_0\rangle$ depends on the quench protocol, which we discuss in Chapter 8.

To validate the MSTHA, the zero mode spectrum was cross-checked against the solution of the quantum pendulum Schrödinger equation solved numerically via the shooting method. The time evolution of the single-mode theory was also compared against the numerical solution of the coordinate Schrödinger equation of the quantum pendulum. The MSTHA containing all modes (up to the respective truncation) was validated first by comparing the truncated spectrum to exact results available from sine-Gordon S-matrix theory [136], and its time evolution was compared to previous implementations of TCSA, where available. For each simulation, we checked the convergence of the method by studying the cutoff dependence of the results.

Chapter 5

Weak integrability breaking in the XXZ spin chain

We investigate the weak integrability breaking of integrable spin chains, where integrability breaking occurs only at higher orders in the perturbation parameter g. Our approach consists of (numerical) exact diagonalisation of the spin-1/2 XXZ spin chain, perturbed by one of its generalised currents, associated with weak integrability breaking [137], and extracting the level spacing statistics, an indicator of integrability, to study the finite size scaling of the crossover from the Poissonian (integrable) to Wigner-Dyson (chaotic/non-integrable) statistics. We compare the results to a known strongly integrability breaking perturbation, the next-to-nearest-neighbour interaction, serving as a benchmark for differentiation between the two classes of integrability breaking.

We start by introducing the notion of weak integrability breaking in Section 5.1, then move on to discussing the Hamiltonian of the XXZ chain and its perturbations in Section 5.2. Section 5.3 contains the introduction and definitions of the level spacing distribution, which serves as the indicator for integrability and its breakdown. In Section 5.2, we briefly discuss the failure of perturbation theory for differentiating between the two types of integrability breaking and present our (numerical) results concerning the crossover in Section 5.5. We give our conclusions in Sec. 5.6.

5.1   Weak integrability breaking

One of the cornerstones of the modern theory of quantum many-body physics is provided by exactly solvable models of quantum systems. In particular, one-dimensional integrable models are at the forefront of interest due to the rapidly emerging field of generalised hydrodynamics, which provides a hydrodynamical description of the non-equilibrium dynamics at the mesoscopic scale [138, 139]. An integrable system is characterised by an infinite number of local conserved charges and corresponding generalised currents given through the respective continuity equations. In this context, one of the main questions is the construction of these charges and generalised currents and their expectation values in equilibrium, with many exact results in the thermodynamic limit [138–142] and finite volume [143] as well. In particular, a recent work by Pozsgay [76] led to the exact algebraic construction of the

current operators in integrable spin chains, including the XXZ model.

It was discovered in a recent work [137] that the existence of exact formulae for the current expectation values is connected to the so-called long-range deformation of integrable short-range spin chains (such as the XXZ model). Originating from the Ads/CFT correspondence [144–146], long-range spin chains are one-parameter deformations of short-range spin chains, that preserve integrability at every order of the deformation parameter by simultaneously increasing the interaction range. At the same time, a strong connection has been found [147] between long-range deformations and the so-called $T\bar{T}$-deformations of integrable quantum field theories [148–151], sharing the same algebraic origins that result in the preservation of integrability at finite orders in the deformation parameter and allows for the construction of the expectation values of the current operators.

More precisely, in [137], it has been observed that for each generalised current of an integrable short-range spin chain, there exists a long-range deformation of the model, such that the leading order perturbing operator is precisely that generalised current. As a result, perturbing an integrable spin chain via one of its generalised currents preserves integrability at the leading order in perturbation theory, with the integrability breaking occurring at higher orders. In contrast, the usual notion of integrability breaking takes place already at first order in perturbation theory, and the integrability of the model can not be maintained by adjusting the perturbing operator order-by-order. To differentiate the two types better, we call the former *weak* and the latter *strong* integrability breaking. Note that earlier works did not make the distinction between these two classes of integrability breaking [152], and in that context, the term 'weak' simply refers to the small value of the non-integrable coupling. Here, we use the term to describe the class of integrability breaking associated with current perturbations and $T\bar{T}$-deformations, where at first order in perturbation theory, the integrability of the model is maintained. The distinction between the two classes of integrability breaking has only come into view recently; in the work [153], the authors argue that systems with weak integrability breaking span the tangent space of integrable systems embedded in the full space of local many-body systems. Accordingly, weakly breaking the integrability is equivalent to following the tangent line of the manifold of integrable systems, and as a result, the onset of chaos is much slower as opposed to systems perturbed by a general integrability breaking perturbation, equivalent to 'radially' moving away from the integrable system. This is also supported by the observation done in [84], where the authors studied the thermalisation of a system induced by integrability breaking via current perturbation within the framework of generalised hydrodynamics. Contrary to a generic integrability breaking operator with coupling λ, the current perturbation does not thermalise the systems on the expected time scales $t \sim \lambda^2$, due to the 'weak' nature of integrability breaking. For this reason, weak integrability breaking is closely related to the out-of-equilibrium dynamics and relaxation of physical systems and warrants a deeper investigation.

5.2 The perturbed XXZ Hamiltonian

The spin-1/2 XXZ chain of finite length L is governed by the Hamiltonian

$$\hat{H}_{\text{XXZ}} = \sum_{i=1}^{L} \left[\hat{s}_i^x \hat{s}_{i+1}^x + \hat{s}_i^y \hat{s}_{i+1}^y + \Delta \hat{s}_i^z \hat{s}_{i+1}^z \right] \tag{5.1}$$

where the spin operators $\hat{s}^a$ are defined as

$$\hat{s}^x = \frac{1}{2} \begin{bmatrix} 0 & 1 \\ 1 & 0 \end{bmatrix} \quad \hat{s}^y = \frac{1}{2} \begin{bmatrix} 0 & -i \\ i & 0 \end{bmatrix} \quad \hat{s}^z = \frac{1}{2} \begin{bmatrix} 1 & 0 \\ 0 & -1 \end{bmatrix}. \tag{5.2}$$

Throughout this chapter, we apply periodic boundary conditions $\hat{s}_{L+1}^a \equiv \hat{s}_1^a$. As discussed before in Section 3.1, the XXZ model has three distinct phases, controlled by the anisotropy parameter Δ, corresponding to a gapless phase for $-1 < \Delta < 1$ and two phases with a finite gap for $|\Delta| > 1$. In the special points $\Delta = \pm 1$, the $U(1)$ symmetry generated by the conserved charge

$$\hat{S}^z = \sum_{i=1}^{L} \hat{s}_i^z \tag{5.3}$$

is enhanced to $SU(2)$. Accordingly, investigating the integrability breaking in these special points requires particular care, and therefore, in the following, we restrict our attention to parameters $|\Delta| \neq 1$.

Studying the effects of weak integrability breaking requires perturbing the XXZ chain via one of its generalised currents [137]. For the model, the first two charges $\hat{Q}_1 = \hat{S}^z$ and $\hat{Q}_2 = \hat{H}_{\text{XXZ}}$ correspond to the $U(1)$ symmetry and time translations, respectively, and are general symmetries of spin chain models studied here, independent of integrability. Therefore, the first non-trivial charge that contributes to integrability is $\hat{Q}_3$, given by

$$\hat{Q}_3 = \sum_{l=1}^{L} \hat{q}_{3,l} \tag{5.4}$$

with

$$\hat{q}_{3,l} = \hat{s}_{l-1}^x \hat{s}_l^z \hat{s}_{l+1}^y - \hat{s}_{l-1}^y \hat{s}_l^z \hat{s}_{l+1}^x + \Delta \left(-\hat{s}_{l-1}^z \hat{s}_l^x \hat{s}_{l+1}^y + \hat{s}_{l-1}^z \hat{s}_l^y \hat{s}_{l+1}^x - \hat{s}_{l-1}^x \hat{s}_l^y \hat{s}_{l+1}^z + \hat{s}_{l-1}^y \hat{s}_l^x \hat{s}_{l+1}^z \right). \tag{5.5}$$

The corresponding generalised current is defined through the continuity equation

$$\hat{j}_{3,l+1} - \hat{j}_{3,l} = i \left[\hat{q}_{3,l}, \hat{H}_{\text{XXZ}} \right] \tag{5.6}$$

and reads

$$\begin{aligned}
\hat{j}_{3,l} = -\frac{1}{2} \Big[& 2\Delta \big(\hat{s}_{l-2}^x \hat{s}_{l-1}^y \hat{s}_l^x \hat{s}_{l+1}^y + \hat{s}_{l-2}^x \hat{s}_{l-1}^z \hat{s}_l^x \hat{s}_{l+1}^z + \hat{s}_{l-2}^y \hat{s}_{l-1}^x \hat{s}_l^y \hat{s}_{l+1}^x + \hat{s}_{l-2}^y \hat{s}_{l-1}^z \hat{s}_l^y \hat{s}_{l+1}^z \\
& + \hat{s}_{l-2}^z \hat{s}_{l-1}^x \hat{s}_l^z \hat{s}_{l+1}^x + \hat{s}_{l-2}^z \hat{s}_{l-1}^y \hat{s}_l^z \hat{s}_{l+1}^y - \hat{s}_{l-2}^x \hat{s}_{l-1}^y \hat{s}_l^y \hat{s}_{l+1}^x - \hat{s}_{l-2}^y \hat{s}_{l-1}^x \hat{s}_l^x \hat{s}_{l+1}^y \big) \\
& - 2 \left(\hat{s}_{l-2}^x \hat{s}_{l-1}^z \hat{s}_l^z \hat{s}_{l+1}^x + \hat{s}_{l-2}^y \hat{s}_{l-1}^z \hat{s}_l^z \hat{s}_{l+1}^y \right) - 2\Delta^2 \left(\hat{s}_{l-2}^z \hat{s}_{l-1}^x \hat{s}_l^x \hat{s}_{l+1}^z + \hat{s}_{l-2}^z \hat{s}_{l-1}^y \hat{s}_l^y \hat{s}_{l+1}^z \right) \Big] \\
& - \frac{1+\Delta^2}{4} \left(\hat{s}_{l-1}^x \hat{s}_l^x + \hat{s}_{l-1}^y \hat{s}_l^y \right) - \frac{\Delta}{2} \hat{s}_{l-1}^z \hat{s}_l^z.
\end{aligned} \tag{5.7}$$

The current-perturbed XXZ Hamiltonian has the form

$$\hat{H}_J = \hat{H}_{\text{XXZ}} + g_3 \hat{J} \,, \tag{5.8}$$

with the perturbation

$$\hat{J} = \sum_{l=1}^{L} \hat{j}_{3,l} \,. \tag{5.9}$$

The system described by the perturbed Hamiltonian (5.8) is non-integrable. However, according to [137], integrability breaking only occurs at higher order in perturbation theory (in g_3). Therefore, we also consider the next-to-nearest-neighbour (NNNI) perturbation of (5.1) as a benchmark, given by the Hamiltonian

$$\hat{H}_{\text{NNNI}} = \hat{H}_{\text{XXZ}} + g_{\text{N}} \sum_{i=1}^{L} \hat{s}_i^z \hat{s}_{i+2}^z = \sum_{i=1}^{L} \left[\hat{s}_i^x \hat{s}_{i+1}^x + \hat{s}_i^y \hat{s}_{i+1}^y + \Delta \hat{s}_i^z \hat{s}_{i+1}^z + g_N \hat{s}_i^z \hat{s}_{i+2}^z \right] \,, \tag{5.10}$$

where the perturbing operator

$$\hat{O}_{\text{NNNI}} = \sum_{i=1}^{L} \hat{s}_i^z \hat{s}_{i+2}^z \,, \tag{5.11}$$

is known to break integrability already at first order, as also studied in [154] where the authors investigated the transport properties altered by the integrability breaking.

By definition, the weak (or strong) classes of integrability breaking is a property of the perturbing operator $\hat{O}$ of an integrable model and is independent of the value of the coupling $g_{\mathcal{O}}$. However, one usually characterises the strength of integrability breaking via the coupling of the integrability-breaking operator appearing in the Hamiltonian. Therefore, to accurately compare the two classes of perturbations $\hat{J}$ and $\hat{O}_{\text{NNNI}}$, we introduce the effective coupling g_{eff} of an operator $\hat{O}$ as

$$g_{\text{eff}} = g_{\mathcal{O}} n_{\mathcal{O}} \,, \tag{5.12}$$

where again the $g_{\mathcal{O}}$ is the coupling appearing in the Hamiltonian

$$\hat{H}_{\text{non-integrable}} = \hat{H}_{\text{integrable}} + g_{\mathcal{O}} \hat{O} \,, \tag{5.13}$$

and $n_{\mathcal{O}}$ is defined as the coefficient of the leading order asymptotic term in the norm of $\hat{O}$:

$$||\hat{O}||_2 = n_{\mathcal{O}} L + \dots \,, \qquad ||\hat{O}||_2 = \sup_{||x||=1} ||\hat{O}x|| \,. \tag{5.14}$$

To leading order, the norm $||\hat{O}||_2$ is linear in the volume since $\hat{O}$ is expressed as a translationally invariant sum of localised terms (see the definitions (5.9) and (5.11)). This parametrisation allows for directly comparing the classes of the two perturbing operators.

Some explicit values of the norms of $\hat{J}$ and $\hat{O}_{\text{NNNI}}$ are shown in Table 5.1. As expected, the norm of the current perturbation is dependent on the anisotropy parameter Δ, as opposed to the NNNI operator. Also, in Fig 5.1, the operator norms are presented as a function of the length L of the chain. Indeed, the norms are extensive with the volume, changing linearly with L apart from some fluctuations in $||\hat{J}||_2$ caused by the fact that L is changed in steps of 2, while the terms $\hat{j}_{3,l}$ in Eq. (5.9) are localised to four sites. The norm $n_{\mathcal{O}}$ can be obtained straightforwardly by linear curve-fitting on the data. Some values are presented in the last column of Table 5.1.

	L	10	12	14	16	18	20	$n_{\mathcal{O}}$
	$\Delta = 0.2$	0.742	1.306	1.232	1.841	1.772	2.346	0.143
$\left\|\hat{J}\right\|_2$	$\Delta = -1.2$	2.376	3.115	3.357	4.614	4.726	6.023	0.348
	$\Delta = 1.2$	2.274	3.115	3.455	4.614	4.412	6.023	0.340
$\left\|\hat{\mathcal{O}}_{\mathrm{NNNI}}\right\|_2$		1.500	2.000	2.500	3.000	3.500	4.000	0.250

Table 5.1: The norms of the perturbing operators J and $\hat{\mathcal{O}}_{NNNI}$
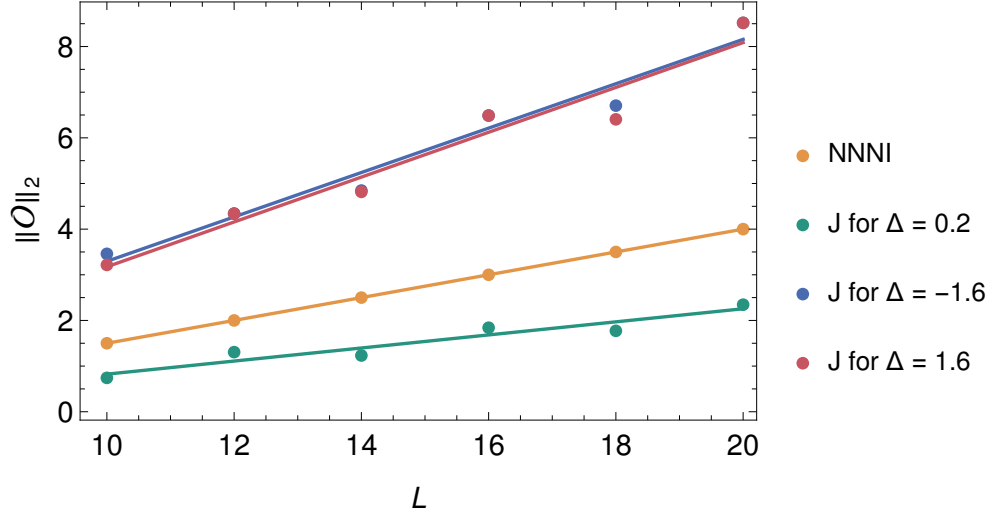
Figure 5.1: Norm of $\hat{J}$ and $\hat{\mathcal{O}}_{\mathrm{NNNI}}$ as a function of the system size L in the three phases.

5.3 The level spacing statistics

The onset of quantum chaos (breaking of integrability) in quantum many-body systems can be studied via the statistics of energy eigenvalues and eigenvectors [155–166] Generally, a physical quantum system is described by a Hermitian Hamiltonian $\hat{H}$ that has real eigenvalues (energy levels) $\{E_j\}$. The level spacing of such a system is given by the difference between consecutive energy levels

$$S_j = E_{j+1} - E_j \qquad E_1 \leq E_2 \leq \dots , \tag{5.15}$$

that are monotonically increasingly ordered. The level spacing distribution $P(s)$ of the system is defined as the distribution of the normalised level spacings

$$s_j = S_j / \bar{S} \tag{5.16}$$

where $\bar{S}$ is the mean level spacing. Random matrix theory predicts that the level spacing distribution of integrable systems is exponential:

$$P(s)_{\mathrm{I}} = e^{-s} , \tag{5.17}$$

while for non-integrable systems, the level spacing statistics take the form of the Wigner-Dyson distribution[1]:

$$P(s)_{\mathrm{NI}} = \frac{\pi}{2} s e^{-\frac{\pi}{4}s^2}. \tag{5.18}$$

As a result, the level spacing distribution is a direct indicator of (non-)integrability. For an integrable model, the different energy levels do not interact due to the presence of a large number of conserved charges. Their value follows a Poissonian distribution, which results in the exponential statistics of the level spacings. When integrability is broken, the charges are no longer conserved, and the interaction between the energy levels results in level repulsion that suppresses the energy differences close to zero. Considering the system as a function of a parameter such as a volume, the energy levels in an integrable system as a function of the volume simply cross while introducing integrability-breaking terms in the Hamiltonian results in repulsion between the levels, opening up additional non-zero level spacings. In the thermodynamic limit, corresponding to infinite systems size (in random matrix theory, infinite matrix size), the change between exponential and the Wigner-Dyson distribution is sudden for any non-zero value of the non-integrable coupling g. In finite system size (finite random matrix size), the distribution is a continuous function of the coupling g, and the change of the statistics from Poissonian to Wigner-Dyson is a continuous crossover that becomes sharper for larger volumes [155, 159].

Additionally, in a finite physical system, the level spacing statistics differ from the random matrix predictions: due to the locality of the Hamiltonian, the structure of the low-energy (and high-energy for lattice systems) part of the spectrum is dictated by quasi-particle excitations. Therefore, when considering the level spacing statistics of the systems introduced in Section 5.2, we discard the low- and high-energy parts and only consider the middle two-thirds of the full spectrum to construct the level spacing distribution. Further care needs to be taken to eliminate degeneracies originating from trivial symmetries of the model [167, 168]. In the following, we restrict ourselves to working in the sector corresponding to zero total momentum, even spatial parity and a fixed non-zero value of $S^z = 2$. Note that in the sector where $S^z = 0$, there is an additional spin-flip symmetry to consider. We obtained similar results in the sectors $S^z = 1$ and 3.
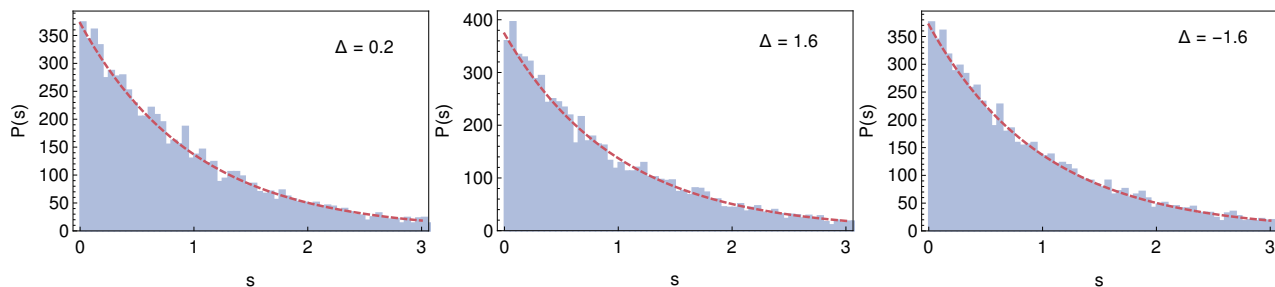

Figure 5.2: Level spacing distribution of the XXZ spin chain for a chain length of $L = 22$ and anisotropy parameters (left to right) $\Delta = 0.2, 1.6, -1.6$ with the exponential distribution fitted (dashed red line).

---

[1]The specific form of the Wigner-Dyson distribution depends on the random matrix ensemble. Here we work with real and symmetric matrices corresponding to the orthogonal Gaussian ensemble.

In Figure 5.2, the level spacing statistics of the unperturbed $g = 0$ XXZ chain are shown for a volume $L = 22$ in the three distinct phases. The exponential fit (shown by red dashed lines) has a single fitting parameter corresponding to the overall normalisation of the distribution and describes the statistics very well.

To illustrate that the perturbations introduced in Section 5.2 indeed break integrability, we switch on a suitably large coupling g and compute the level spacing distribution, shown in Fig. 5.3. The statistics take the form of the Wigner-Dyson distribution, indicated by the matching fitting of (5.18). As before, the only fitting parameter here is the overall normalisation of the distribution.
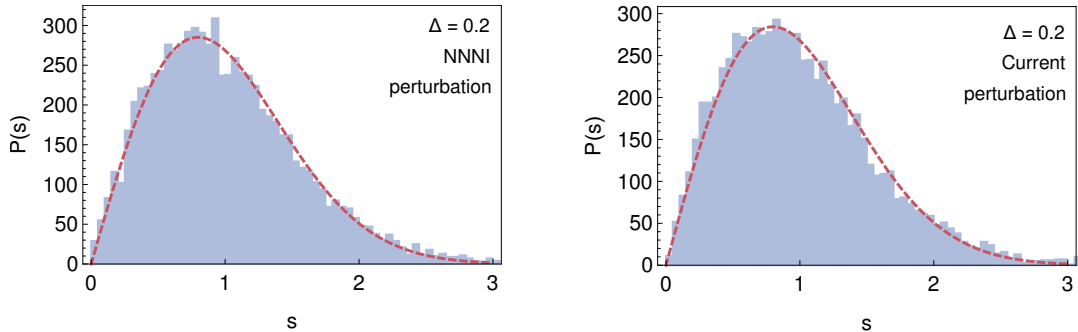

Figure 5.3: Typical level spacing statistics of a non-integrable system with the Wigner-Dyson distribution fitted (red dashed line). *left*: $\hat{H}_{\text{NNNI}}$ with $L = 22$ $\Delta = 0.2$ and $g_{\text{eff}} = 0.1$. *right*: $\hat{H}_J$ with $L = 22$, $\Delta = 0.2$ and $g_{\text{eff}} = 0.42$.

5.4   The failure of perturbation theory

By definition, weak integrability differs from the usual strong integrability breaking as it retains the integrable properties of the system at first order in perturbation theory. Therefore, an attractive (and very simple) way of determining the order of integrability breaking is to consider the spectrum as computed from first-order perturbation theory in the coupling g to construct the level spacing statistics. However, it turns out that this route falls short, as illustrated in Fig 5.4, where the level spacing distribution of H_{NNNI} is shown as computed by first-order perturbation theory. Clearly, the statistics remain exponential even for very large values of the coupling g.
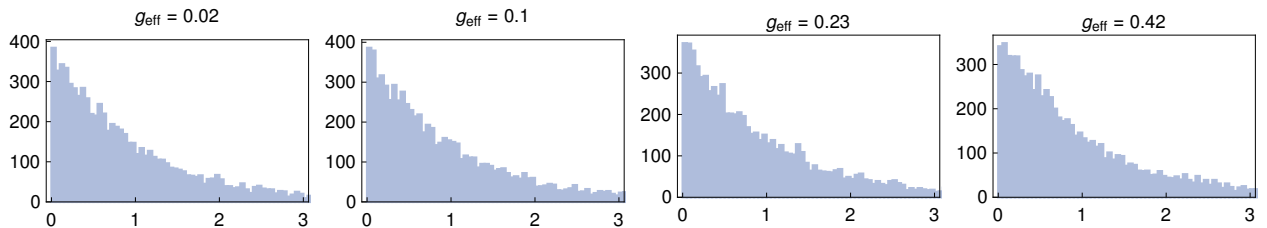

Figure 5.4: The level spacing statistics of $\hat{H}_{\text{NNNI}}$ computed from first-order perturbation theory for the case $L = 22$, $\Delta = 0.2$, and different values of the coupling.

To gain a more detailed picture, we consider the two-level subsystem of an integrable theory as a function of the volume L (continued to real values), for which the breaking of integrability introduces level repulsion:

$$\begin{bmatrix} a_1(L) & 0 \\ 0 & a_2(L) \end{bmatrix}, \tag{5.19}$$

where the unperturbed energy levels are denoted by $a_{1,2}(L)$. A general perturbation of the subsystem takes the form

$$\begin{bmatrix} a_1(L) + g\Delta a_1(L) & g\epsilon(L) \\ g\epsilon(L) & a_2(L) - g\Delta a_2(L) \end{bmatrix}. \tag{5.20}$$

parametrised by the diagonal and off-diagonal elements of the perturbation $\Delta a_{1,2}(L)$ and $\epsilon(L)$, with the integrability-breaking coupling g. For the unperturbed system, corresponding to integrability, the level crossing happens for L_0 for which

$$a_1(L_0) = a_2(L_0). \tag{5.21}$$

At first order in perturbation theory in g, the two-level spectrum is computed by diagonalising

$$\begin{bmatrix} a_1(L) + g\Delta a_1(L) & 0 \\ 0 & a_2(L) - g\Delta a_2(L) \end{bmatrix}, \tag{5.22}$$

which simply shifts the level crossing to a position L_* that can be computed from

$$a_1(L_*) + g\Delta a_1(L_*) = a_1(L_*) - g\Delta a_2(L_*), \tag{5.23}$$

and up to first order in g takes the form

$$L_*(g) = L_0 - g\frac{\Delta a_1(L_0) - \Delta a_1(L_0)}{a_1'(L_0) - a_2'(L_0)} + O\left(g^2\right). \tag{5.24}$$

As a result, first-order perturbation theory does not account for level repulsion, and the level spacing statistics remain exponential.

As first-order perturbative corrections did not introduce repulsion between the energy levels, it is tempting to move on to second-order perturbation theory. The exact diagonalisation of the perturbed subsystem (5.20) results in level repulsion due to the off-diagonal terms $\varepsilon(L)$. However, perturbative expansion of the perturbed energy levels up to second order in g is numerically unstable in the vicinity of two close energy levels

$$E_{1,2} = a_{1,2}(L) + g\Delta a_{1,2}(L) \pm g^2\frac{2\epsilon(L)^2}{a_1(L) - a_2(L)} + O\left(g^3\right) \tag{5.25}$$

due to the energy difference appearing in the denominator, which diverges when the energy levels $a_1(L)$ and $a_2(L)$ are close, as is the case for an integrable system. Therefore, the order of integrability breaking can not be concluded by perturbatively computing the spectrum to construct the level spacing statistics.
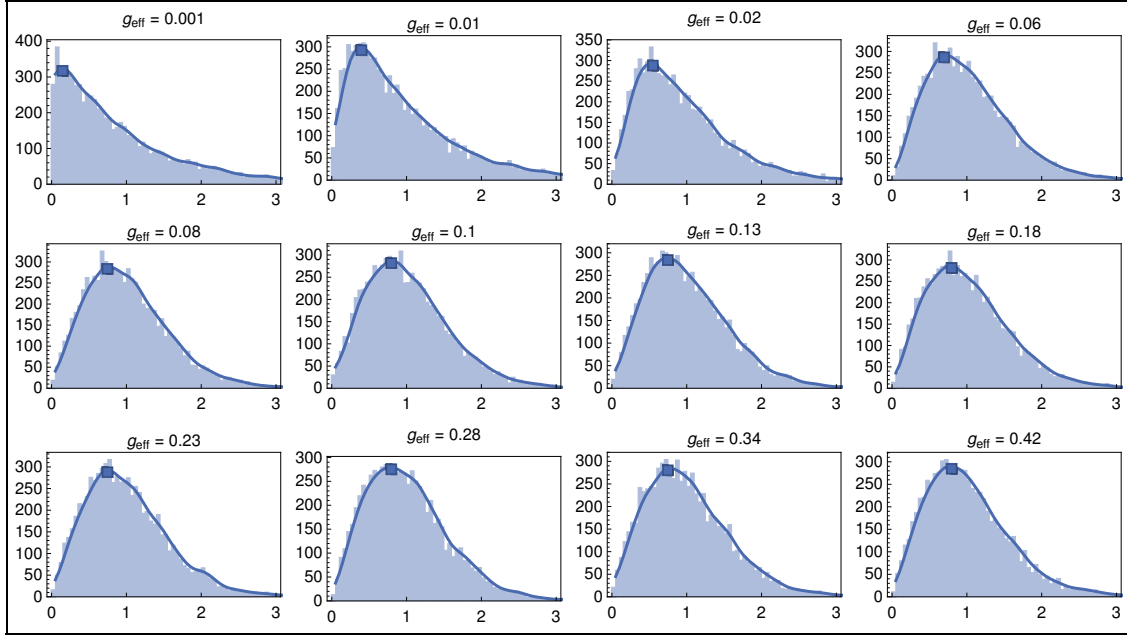
(a) NNNI perturbation
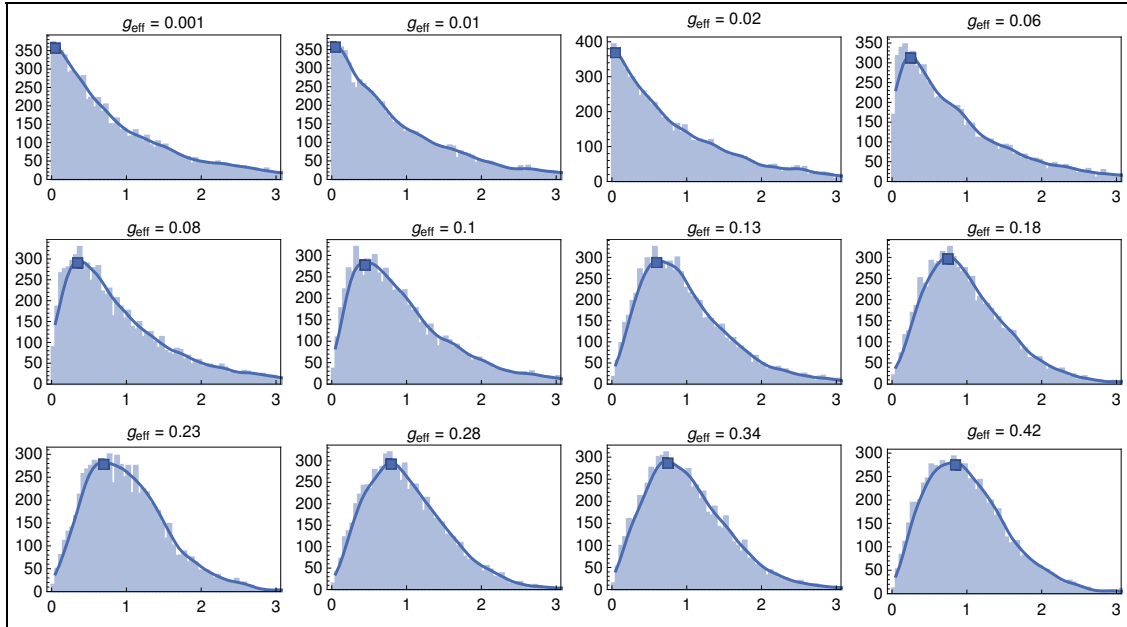
(b) Current perturbation

Figure 5.5: Determination of the dependence of the peak position on g_{eff} for the NNNI (a) and current (b) perturbations for $L = 22$, $\Delta = 0.2$. The blue solid lines correspond to the Gaussian-filtered data. The extracted peak positions are denoted by blue markers.

5.5 The crossover from Poissonian to Wigner-Dyson statistics

Seeing the failure of perturbation theory, we apply (numerical) exact diagonalisation to the perturbed XXZ model introduced above and extract the level spacing statistics from the numerically obtained spectrum. In finite volume, varying the integrability-breaking coupling g results in a smooth crossover between the exponential and Wigner-Dyson statistics. To characterize the crossover, we obtain the peak of the intermediate distributions that move from zero to the final value of $\sqrt{2/\pi}$ characteristic to the Wigner-Dyson function (5.18).

The normalised level spacings are sorted into bins of width 0.5 for chain lengths $L = 16, 18$ and 20 and of width 0.1 for $L = 22$ and 24. The resulting distribution is subject to fluctuations due to the finite bin size, which we smooth out by applying a Gaussian filter of kernel radius $r = 6$ for $L = 16$ and 18 and $r = 4$ for $L \geq 20$. We note that the number of level spacings for chain lengths below $L \leq 16$ is insufficient to yield suitable statistics. Fig 5.5 displays the crossover from exponential to Wigner-Dyson statistics, together with the obtained peaks of the appropriate crossover distributions for $\Delta = 0.2$ and a chain length of $L = 22$. It is clear that for the NNNI perturbation, the crossover takes place at smaller couplings than for the current perturbation, suggesting the difference between the two classes of integrability breaking of the operators.
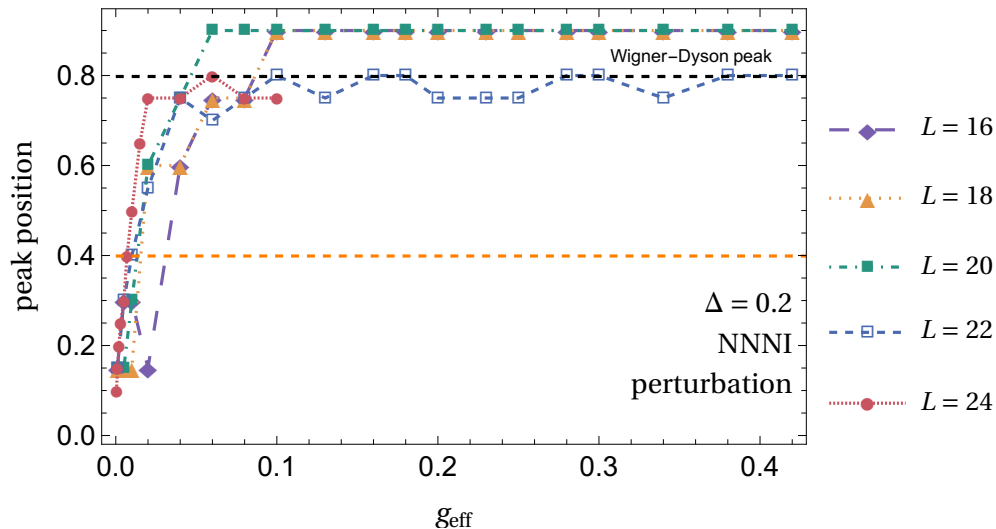

Figure 5.6: The obtained peak positions as a function of the effective coupling g_{eff} for the case of $\hat{H}_{\text{NNNI}}$ for $\Delta = 0.2$ and different chain lengths L. The dashed black line marks the peak position of the Wigner-Dyson distribution (5.18) $\sqrt{2/\pi}$, and the orange line corresponds to the crossover peak position $\sqrt{1/2\pi}$. As expected, the transition from Poissonian to Wigner-Dyson statistics is faster for longer chains.

Figs 5.6 and 5.7 display the g-dependence of the obtained peaks of the intermediate distributions in the gapless phase for $\Delta = 0.2$ and various chain lengths L. Though filtering allows for the determination of the peaks, the accuracy of their position is ultimately limited by the bin size, resulting in the observed fluctuations. According to expectations, the crossover
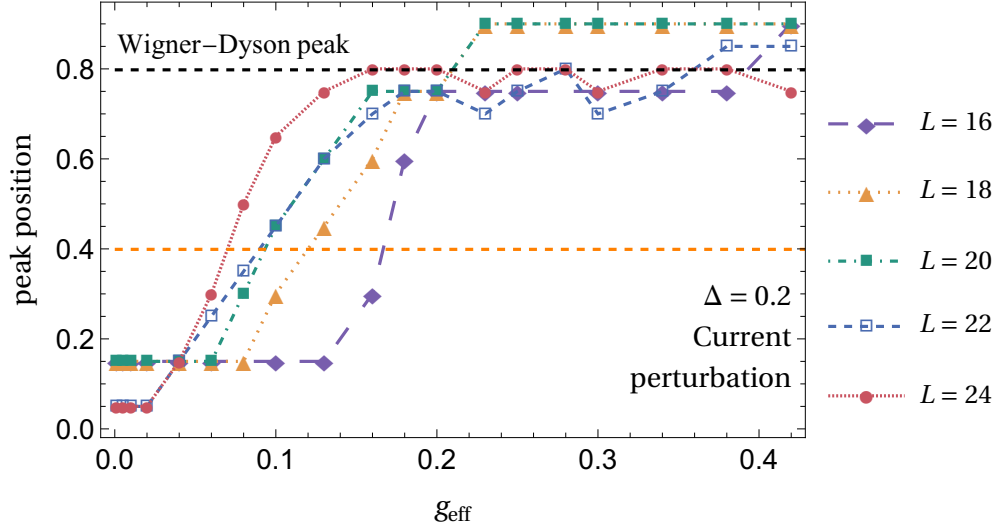
Figure 5.7: The obtained peak positions as a function of the effective coupling g_{eff} for the case of $\hat{H}_J$ for $\Delta = 0.2$ and different chain lengths L. The dashed black line marks the peak position of the Wigner-Dyson distribution (5.18) $\sqrt{2/\pi}$, and the orange line corresponds to the crossover peak position $\sqrt{1/2\pi}$. The transition from Poissonian to Wigner-Dyson statistics is faster for longer chains, as expected.

is faster for longer chains, and it is substantially slower for the current perturbation than for the NNNI case for all values of L, consistent with the idea that for the case of the current perturbation, integrability is broken at higher-than-first order in perturbation theory.

To obtain more decisive evidence that the current perturbation preserves integrability at first order, we define the crossover coupling g_{cr} as the effective coupling g_{eff} for which the peak of the intermediate distribution is exactly halfway between the location of the peaks of the limiting exponential and Wigner-Dyson distributions. That is, for $g_{\text{eff}} = g_{\text{cr}}$, the peak of the statistics is at x_0, where $2x_0 = \sqrt{2/\pi}$ is the position of the peak of the Wigner-Dyson distribution. Since for larger volumes L, the crossover is expected to occur faster (as already seen before), $g_{\text{cr}}(L)$ as a function of the volume should be a monotonically decreasing function of L. More precisely, in the gapless phase, we expect the crossover coupling to be described by a power-law [169, 170]:

$$g_{\text{cr}} \propto L^{-\alpha} \qquad \alpha > 0 \,, \tag{5.26}$$

whereas in the massive phase, it is expected to be an exponentially decaying function of the finite size L:

$$g_{\text{cr}} \propto e^{-\beta L} \qquad \beta > 0 \,. \tag{5.27}$$

Note, however, that since the crossover is a smooth function of the effective coupling, other definitions of the crossover scale are also perfectly possible [169, 170]. In the work [170], the authors defined g_{cr} as the fitting parameter (coupling scale) of a hyperbolic function fitted to the transition of the intermediate peak positions. Indeed, for the case of the NNNI perturbation, they obtained the exponent $\alpha = 3$, which we also recover using our definition outlined above.

5.5.1 The gapless phase

Here we discuss the results obtained by performing the above-described procedure for both the current and NNNI perturbations, focusing on the gapless phase for $\Delta = 0.2$.
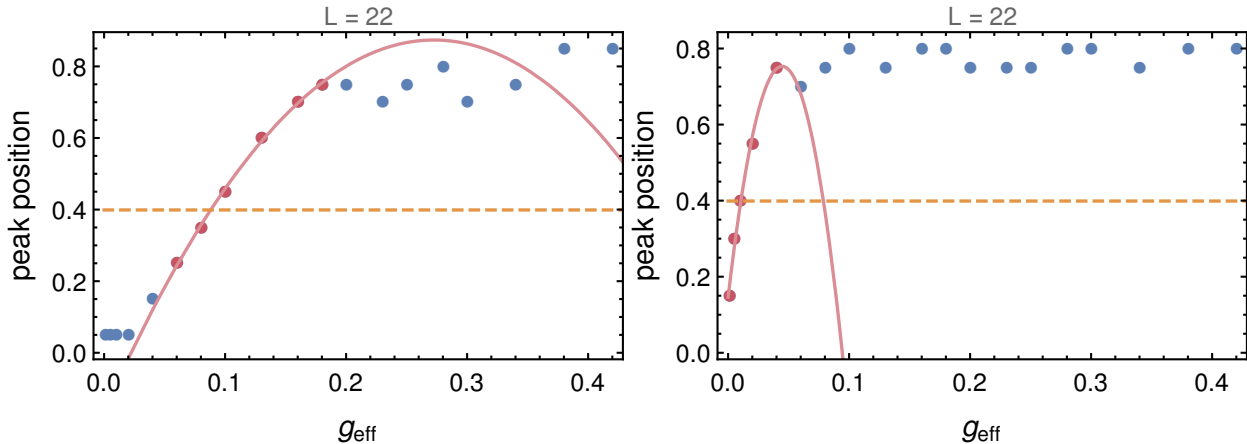

Figure 5.8: Computation of the crossover coupling g_{cr} from the peak positions for different effective couplings for the current (left) and NNNI perturbation (right) in the gapless phase ($\Delta = 0.2$). The parabola fitted around x_0 (indicated by the orange dashed line) is denoted by the red solid line.

In Fig. 5.8, the obtained peak positions for $L = 22$ can be seen (similarly to Fig. 5.7 and 5.6) with a parabola $f(g)$ fitted to the data around x_0. The crossover coupling g_{cr} can be obtained by simply solving

$$f(g_{\text{cr}}) = x_0 \tag{5.28}$$

for all values of the volume L, resulting in the function $g_{\text{cr}}(L)$, shown in Fig. 5.9 for both the current and NNNI perturbations, together with the logarithm of the crossover coupling $\log g_{\text{cr}}$. As expected, the results exhibit a power-like decay with the volume L, and the exponents can be simply determined by fitting a linear function on $\log g_{\text{cr}}(L) = a + b \log L$ to the results, yielding

$$\begin{aligned} b_J &= -1.99 \pm 0.18 \\ b_{\text{NNNI}} &= -3.11 \pm 0.27 \end{aligned} \tag{5.29}$$

As mentioned before, for the case of the NNNI perturbation, we recover the previously obtained exponent of -3, claimed to be universal for integrability at first order in gapless spin chains [169, 170]. Also, the exponent b_J, corresponding to the current perturbation, supports the idea that the current perturbation only breaks integrability at higher orders in perturbation theory in g.

5.5.2 The massive phase

Now, we turn to the results obtained in the gapped phase, where the crossover coupling is expected to be an exponentially decaying function of the volume. Due to the finite correlation
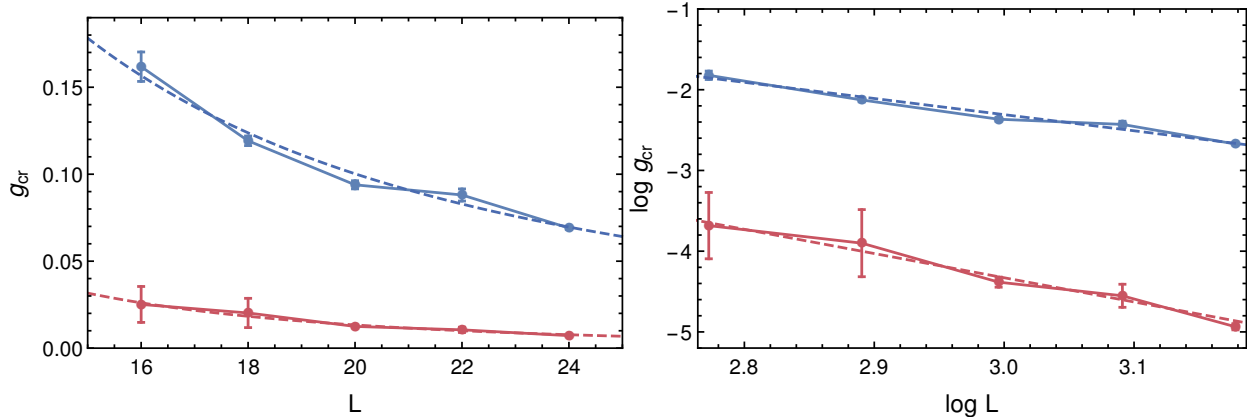
Figure 5.9: The crossover coupling g_{cr} as a function of the volume for the $\hat{J}$ (blue markers) and NNNI perturbations (red markers) on normal (left) and log-log scale (right) in the gapless phase ($\Delta = 0.2$). Dashed lines correspond to the fitted AL^{-3} (red) and BL^{-2} (blue), respectively.

length, correlations typically decay exponentially, and as a result, the finite size effects are also expected to decay exponentially with the volume [171, 172].

Figs. 5.10 and 5.11 display the crossover coupling and its logarithm as a function of the volume L for $\Delta = 1.6$ and -1.6, respectively, corresponding to the two gapped phases. To demonstrate the exponential behaviour, we fit a linear function $c + dL$ on $\log g_{cr}$. For $\Delta = 1.6$, the resulting scaling exponents are given by

$$
\begin{aligned}
d_J &= -0.056 \pm 0.014 \\
d_{NNNI} &= -0.157 \pm 0.020 \,,
\end{aligned}
\tag{5.30}
$$

while for $\Delta = -1.6$ the obtained exponents are

$$
\begin{aligned}
d_J &= -0.063 \pm 0.014 \\
d_{NNNI} &= -0.137 \pm 0.043 \,.
\end{aligned}
\tag{5.31}
$$

Again, there is a substantial difference between the strength of integrability breaking for the two operators. For the current perturbation, the crossover coupling is a magnitude larger than for the NNNI perturbations for all values of the volume, hinting at the difference between the classes of integrability breaking. The conclusive evidence again, however, is that the coefficient d describing the decay of the crossover coupling with the volume is much smaller for J than for the NNNI perturbation, in agreement with the conjecture that the current perturbation preserves integrability at first order in perturbation theory.

5.6   Summary

We presented our results concerning the weak integrability breaking of the XXZ spin chain, induced by perturbing it via one of its generalised currents of the conserved charges that imply integrability. In contrast with the usual ('strong') class of integrability breaking, where
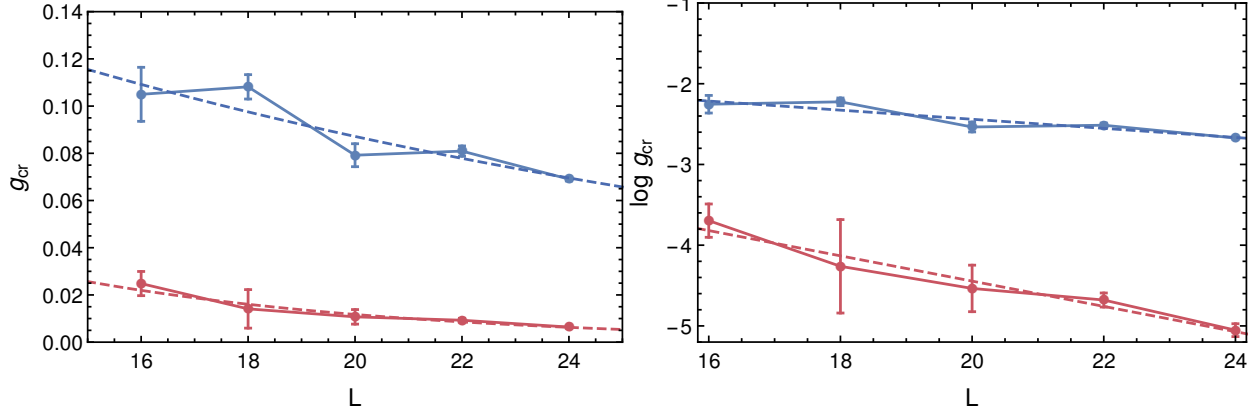
Figure 5.10: The crossover coupling g_{cr} as a function of the volume for the $\hat{J}$ (blue markers) and NNNI perturbations (red markers) on normal (left) and log-log scale (right) in the antiferromagnetic gapped phase ($\Delta = 1.6$). The fitted exponentials are shown in dashed lines.

Figure 5.11: The crossover coupling g_{cr} as a function of the volume for the $\hat{J}$ (blue markers) and NNNI perturbations (red markers) on normal (left) and log-log scale (right) in the ferromagnetic gapped phase ($\Delta = -1.6$). The fitted exponentials are shown in dashed lines.

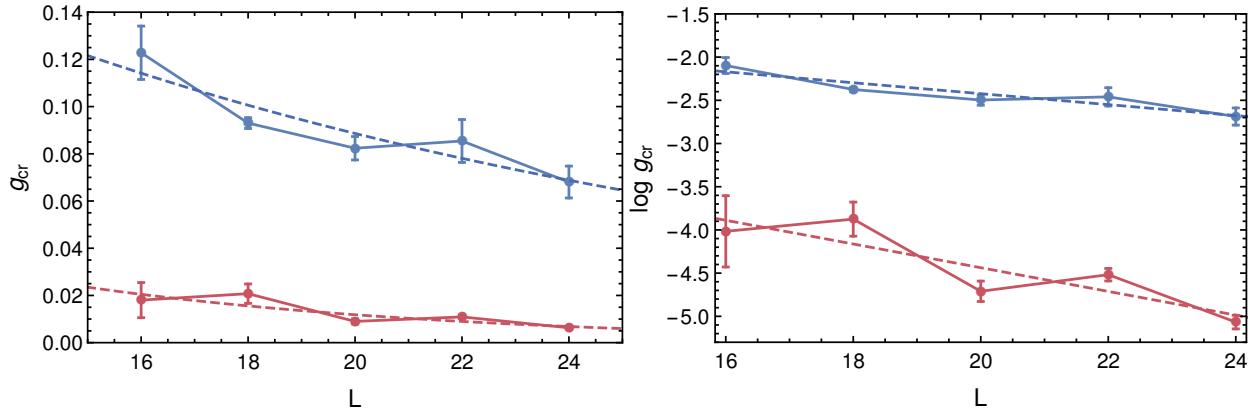integrability is broken already at first order in perturbation theory in the integrability breaking coupling g, a system with weakly broken integrability preserves its integrable properties at first order, and the onset of chaos takes place only at higher orders.

Our approach consisted of perturbing the (integrable) spin-1/2 XXZ spin chain via its first generalised current $\hat{J}$, which is supposed to break integrability only weakly [137], and evaluating the level spacing statistics as a proxy of the presence of integrability using exact diagonalisation. We compared the results to a well-known strongly integrability-breaking perturbation, the next-to-nearest neighbour (NNNI) perturbation, serving as a benchmark. Comparison between the two perturbations independently of their normalisation requires rescaling the integrability-breaking couplings g by the operator norms per unit volume.

In finite volume, the onset of quantum chaos can be characterised by the level spacing distribution, which exhibits a smooth crossover from the Poissonian (integrable) to Wigner-

Dyson statistics (chaotic/non-integrable) as the integrability-breaking parameter g is increased. In accordance with expectations [137], for the current perturbation $\hat{J}$, we find that the crossover values of the rescaled couplings were markedly higher for any fixed value of the volume L, and their behaviour with L exhibited a much slower decay than for that of the NNNI perturbation. Specifically, we found that in the gapless phase, the scaling of the NNNI crossover coupling with the volume goes as $1/L^3$, a law previously claimed to be universal in gapless spin chains with strongly broken integrability [170], albeit without analytical evidence. In contrast, in the case of the current perturbation, the crossover values of the coupling display a slower scaling with an exponent ≈ 2 (5.29), supporting the idea that the current perturbation only breaks integrability at higher orders in perturbation theory, resulting in a slower onset of quantum chaotic behaviour.

The nature of the exponents is still an open question; in the work [170], the exponent -3 is claimed to be universal for gapless spin chains, albeit without analytical support. Nevertheless, it is natural to speculate that the value of the exponent is ultimately dependent on the order in which integrability is broken. Sadly, as discussed above in Section 5.4, the crossover in the level spacing statistics can not be resolved by perturbation theory, given the breaking of integrability is generic in the sense that the onset of chaos happens through the introduction of repulsion between two energy levels of the integrable system. Here we note, however, that in non-integrable quantum field theories obtained as perturbations of conformal field theories, the onset of chaos (crossover to the Wigner-Dyson statistics) occurs already in the perturbative regime [165].

Chapter 6

Non-equilibrium dynamics in the φ^4 theory

Generally, strongly interacting quantum field theories can not be solved exactly, and one has to resort to approximate or numerical methods to compute the dynamics. Typically, their dynamics is studied in some semi-classical limit by neglecting higher-order correlations. As discussed previously in Chapter 4, semi-classical methods are generally uncontrolled and require careful testing against other, more controlled methods.

Here we consider the non-equilibrium dynamics of the (1+1)d φ^4 theory in the $\mathbb{Z}_2$-unbroken phase, serving as a testing ground for two widely used semi-classical methods: the truncated Wigner approximation (TWA) and the (Gaussian) self-consistent method (SCA), also known as the mean field approximation. To test the validity of the semi-classical approximations, we also apply a flavour of the truncated Hamiltonian approach (THA), built upon a massive free boson basis. To study the time evolution of observables, we perform general quenches where the system is initially in the ground state of a free boson with mass m_0 and at $t = 0$, it is quenched to the massive interacting theory with post-quench (renormalised) mass m and quartic coupling $\lambda/4!$.

6.1 The quench protocol

For the (1+1)d φ^4, a detailed discussion is given in Section 3.2. The finite volume theory is presented in Section 4.3.1 together with the detailed implementation of the THA.

A general quantum quench in the φ^4 theory consists of changing the initial (pre-quench) parameters m_0 and λ_0 to some post-quench values m and λ. Therefore, the finite volume Hamiltonian describing the system before the quench is given by the pre-quench Hamiltonian

$$\hat{H}_0 = \int_0^L dx : \left[\frac{1}{2}(\partial_t\hat{\varphi})^2 + \frac{1}{2}(\partial_x\hat{\varphi})^2 + \frac{1}{2}m_0^2\hat{\varphi}^2 + \frac{\lambda_0}{4!}\hat{\varphi}^4 \right] :, \tag{6.1}$$

while after $t = 0$, it is governed by the post-quench Hamiltonian

$$\hat{H} = \int_0^L dx : \left[\frac{1}{2}(\partial_t\hat{\varphi})^2 + \frac{1}{2}(\partial_x\hat{\varphi})^2 + \frac{1}{2}m^2\hat{\varphi}^2 + \frac{\lambda}{4!}\hat{\varphi}^4 \right] :, \tag{6.2}$$

where L is the finite volume and we use periodic boundary conditions. In our protocol, the initial state is taken to be the ground state of $\hat{H}_0$, that is $\hat{H}_0 |\Psi_0\rangle = E_0 |\Psi_0\rangle$ with the smallest eigenvalue E_0. After $t = 0$ the time evolution is generally out-of-equilibrium and is governed by (6.2):

$$|\Psi(t)\rangle = e^{-i\hat{H}t} |\Psi_0\rangle. \tag{6.3}$$

Presently, we focus on the Fourier modes of the two-point function

$$C_2(x,t) = \langle : \hat{\varphi}(x,t)\hat{\varphi}(0,t) : \rangle \tag{6.4}$$

given (in Schrödinger picture) by

$$C_2(n,t) = \langle : \hat{\varphi}_k(t)\hat{\varphi}_{-k}(t) : \rangle = \langle \Psi(t)| : \hat{\varphi}_k\hat{\varphi}_{-k} : |\Psi(t)\rangle, \qquad k = \frac{2\pi n}{l}. \tag{6.5}$$

Due to the periodic boundary conditions, the available Fourier modes become discrete and can be characterised by an integer n:

$$k = \frac{2\pi n}{l}, \qquad n \in \mathbb{Z}. \tag{6.6}$$

For our discussions, we can set the post-quench mass $m = 1$ and the pre-quench coupling $\lambda_0 = 0$ without the loss of generality. We choose the initial state $|\Psi_0\rangle$ as the ground state of the free massive boson corresponding to m_0 and simultaneously turn on the quartic coupling and change the mass to $m = 1$. To compute (6.5), we apply the THA built on the eigenbasis of the free massive boson of mass $m = 1$, which is consequently equal to the post-quench mass. (The reader is referred to Section 4.3.1 for the implementation details.) Generally, it is not required to choose the post-quench mass to be the unit mass. However, the choice of $m = 1$ is well-suited for the current THA as the modes corresponding to the post-quench mass are already incorporated in the basis. The initial state can be constructed exactly in terms of the post-quench modes through Bogolyubov transformation; however, its normalisation must be adjusted to ensure that the vector has a unit norm on a truncated basis.

In Fig. 6.1, the cutoff dependence of the renormalised THA time evolution is shown for two different (mild and strong) quenches. The results show negligible truncation effects, even with the large differences between the various computational basis dimensions used. Generally, the precision of the THA can be arbitrarily refined by increasing the cutoff, given sufficient computational power is available. In the following, we set the cutoff parameter $n_{\max}$ so that the maximum difference between the time curves corresponding to the two largest cutoff values is in the fourth digit (or smaller). Therefore, the precision of the THA can be (crudely) estimated to be of order $\approx 0.1\%$. As a result, in the quenches studied here, the THA results can be considered converged and essentially numerically exact up to this precision, allowing for the THA to serve as a direct test to determine the accuracy and validity of semi-classical approaches.

We also mention that THA results for $t \geq L$ are expected to differ from the infinite volume dynamics due to finite size effects originating from particles travelling around the volume. However, we are mainly interested in the short and intermediate times and determining the applicability of semi-classical methods, and therefore, we can focus our attention on short times $t \leq L$, where deviations from the well-established THA are already expected to occur.
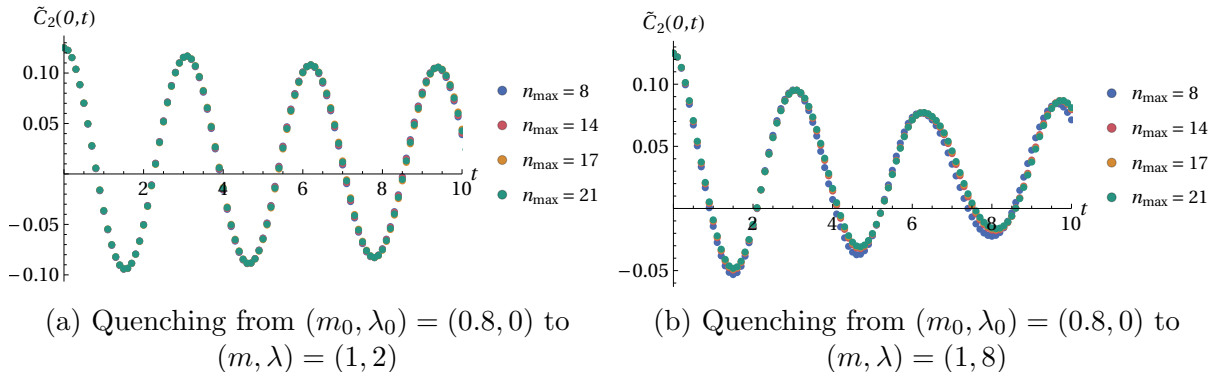
(a) Quenching from $(m_0, \lambda_0) = (0.8, 0)$ to $(m, \lambda) = (1, 2)$

(b) Quenching from $(m_0, \lambda_0) = (0.8, 0)$ to $(m, \lambda) = (1, 8)$

Figure 6.1: Time evolution of the zero-mode of the two-point function $\tilde{C}_2(n = 0, t)$ for (a) a mild and (b) a strong quench computed by the THA for different values of the cutoff and volume $l = 10$. Different colors denote different values of n_{max}, corresponding to $n_{\mathrm{max}} = 8$, 14, 17, and 21 resulting in Hilbert space dimensions cc. 400, 16000, 90000 and 700000 states, respectively.

6.2 SCA vs. THA

The self-consistent approximation, discussed in Section 4.1, was developed by Cardy and Sotiriadis [111]. In this approach, the interacting dynamics are approximated by Gaussian time evolution of free bosonic modes with a time-dependent effective mass that is computed from a self-consistency equation (4.7):

$$m_{\mathrm{eff}}^2(t) = m^2 + \frac{\lambda}{2} \sum_k \left(\langle \hat{\varphi}_k(t) \hat{\varphi}_{-k}(t) \rangle - \frac{1}{2\omega_k} \right) . \tag{6.7}$$

with $\omega_k^2 = m^2 + k^2$. The renormalisation procedure is equivalent to normal ordering with respect to the bosonic modes corresponding to mass m and, therefore, matches that of the THA. Furthermore, by choosing the post-quench mass m as the unit mass, we can directly compare the SCA to the THA when performing quantum quenches.

To compare the SCA time evolution to the THA results, we work in a finite volume $l = Lm = 10$, which discretises the allowed Fourier modes $k = 2\pi n/L$ with $n \in \mathbb{Z}$. The set is made finite by introducing an upper cutoff N_{max} so that $|n| \leq N_{\mathrm{max}}$. We choose the cutoff N_{max} so that the results converge. However, choosing the cutoff too high introduces instabilities and needs to be avoided. We remark that the maximum momentum mode number N_{max} included in the SCA is independent of the cutoff parameter of the THA. Moreover, in the following, the time-discretisation parameter dt is chosen so that the time evolution can be considered continuous.

To test the validity of the SCA and the THA time evolution, we performed mass quenches (λ set to zero) for which the mean-field theory becomes exact and the truncated Hamiltonian approach yielded practically exact results.

In Fig. 6.2, the time evolution of the correlator (6.5) can be seen following a general quantum quench where the initial mass is changed from $m_0 = 0.8$ to $m = 1$ while simultaneously switching on the quartic coupling from zero to some finite value λ. We present

(a) $(m_0, \lambda_0) = (0.8, 0) \to (m, \lambda) = (1, 2)$

(b) $(m_0, \lambda_0) = (0.8, 0) \to (m, \lambda) = (1, 4)$

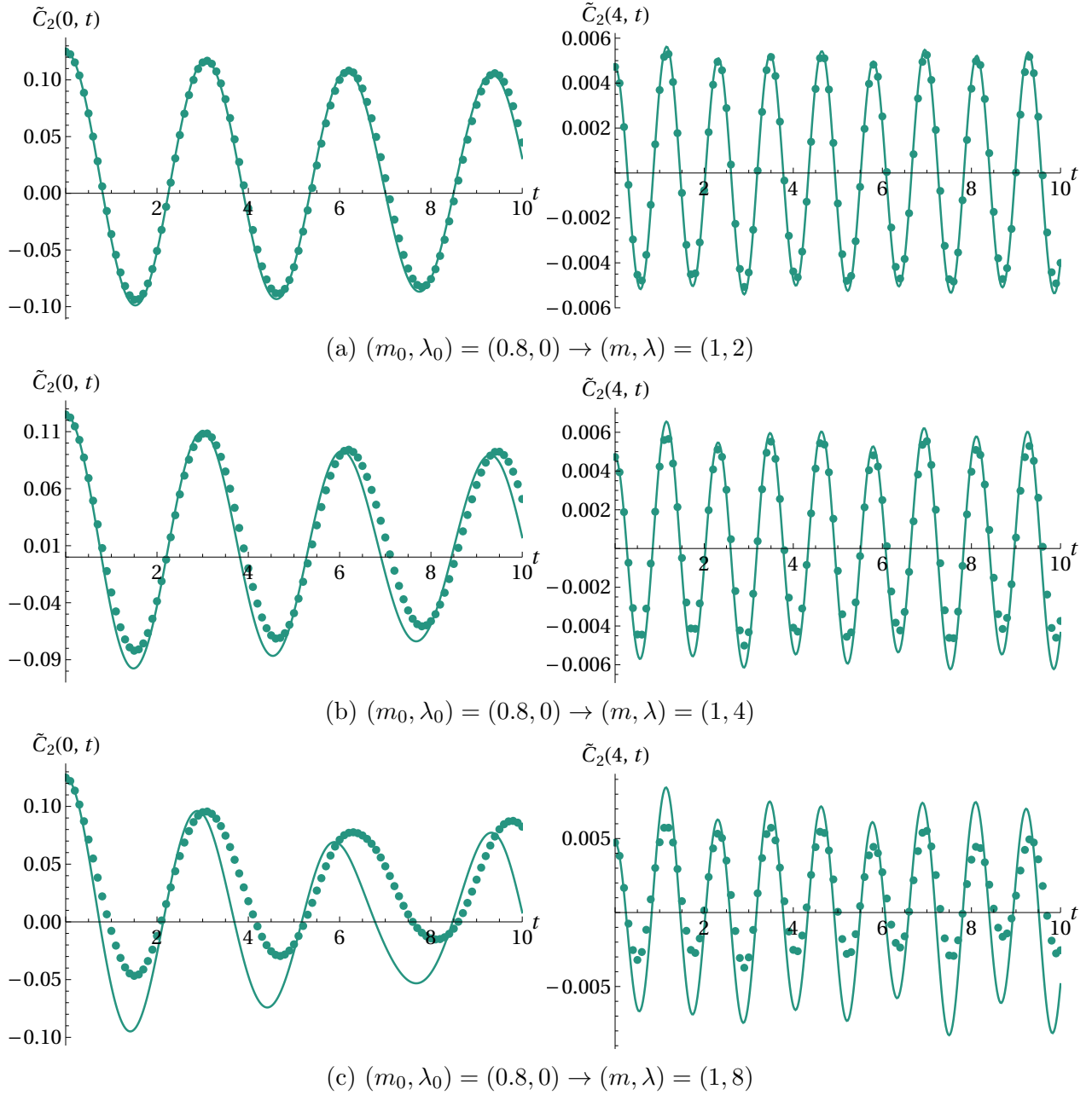(c) $(m_0, \lambda_0) = (0.8, 0) \to (m, \lambda) = (1, 8)$

Figure 6.2: Time evolution of the $n = 0$ and $n = 4$ modes of C_2 following quenches with the mass changed from 0.8 to 1 and different post-quench interactions in volume $l = 10$. Dots denote the THA data computed using the renormalisation improvement (4.48), at a cutoff value of $n_{\max} = 21$. The solid line denotes the results of the self-consistent approach.
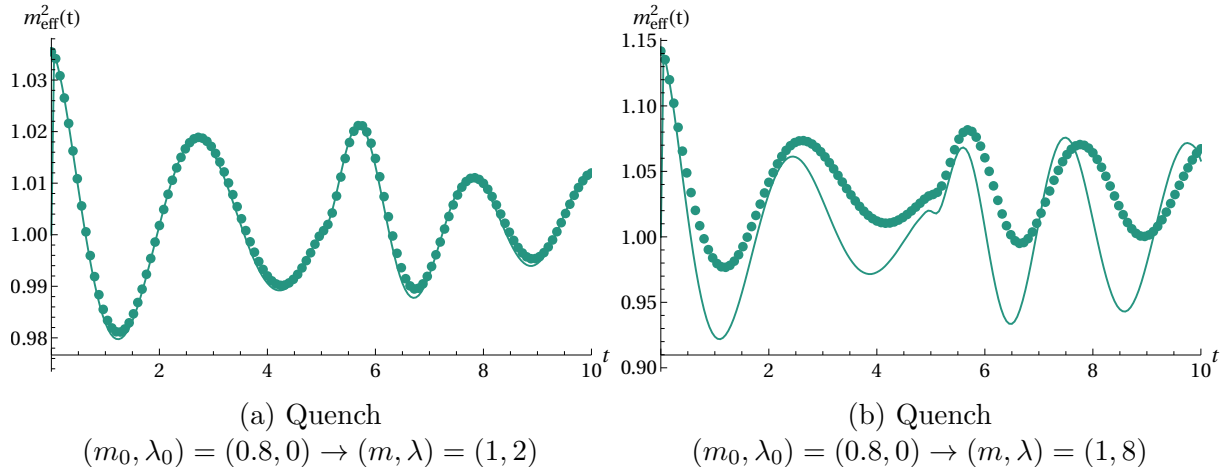
(a) Quench
$(m_0, \lambda_0) = (0.8, 0) \to (m, \lambda) = (1, 2)$

(b) Quench
$(m_0, \lambda_0) = (0.8, 0) \to (m, \lambda) = (1, 8)$

Figure 6.3: The effective mass in the THA (markers) and SCA (solid line) approximations, calculated using the largest value of $n_{\mathrm{max}} = 21$ for a volume parameter $l = 10$. (a) In the perturbative regime, the two methods agree and reproduce the exact evolution of the effective mass, which stays close to the renormalised mass $m = 1$. (b) For a stronger quench, the effective mass deviates from 1, and the SCA fails to predict the correct time evolution.

the results for the zero mode of the correlator $C_2(0, t)$ alongside a higher-mode component $C_2(4, t)$ as computed by both the SCA and the THA. The results show a progressively increasing discrepancy between the methods, showcasing the imminent failure of the SCA as the coupling increases. As seen in Fig. (6.5), the main source of the difference can be attributed to the mean-field theory failing to reproduce the post-quench frequencies, an effect that is increasing with the coupling. Moreover, this effect gives rise to a discrepancy between the amplitudes as well, as suggested by (4.14). However, looking at the higher-mode component, we can see that the frequencies match quite well irrespective of the value of the coupling, suggesting that the disagreement can be attributed to the difference in mass scales between the two methods. That is, for a given effective mass m_{eff}, the temporal frequency corresponding to a Fourier mode k is of the form

$$\Omega_k \sim \sqrt{m_{\mathrm{eff}}^2 + k^2} \,, \tag{6.8}$$

and thus, the mass scale m_{eff} mostly determines the low-frequency end of the spectrum. For high wavenumbers k, the dominating contribution to the temporal frequencies comes from the mode k, relaxing the importance of a precise mass scale m_{eff}. Indeed, the two methods produce different mass scales, as illustrated in Fig. 6.3. While for the SCA, the effective mass is obtained self-consistently from (6.7) using the mean field value of the two-point function, in the THA computation of m_{eff} requires substituting of the exact (truncated) correlator to (6.7), leading to different results. As seen in Fig. 6.3a, for small couplings, the effective mass resulting from the two methods match but begins to grow apart with increasing coupling as shown in Fig. 6.3b. This leads to a noticeable difference in the temporal modes for smaller Fourier modes, while it becomes less pronounced for higher wavenumbers, in accordance with Fig. 6.2c.
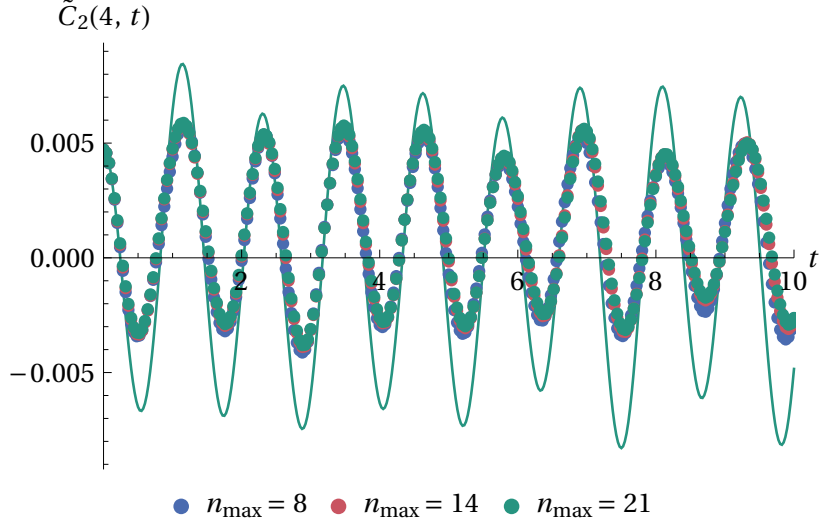
56

Figure 6.4: THA and SCA results of $\tilde{C}_2(4, t)$ for the quench $(m_0, \lambda_0) = (0.8, 0) \rightarrow (m, \lambda) = (1, 8)$ for $l = 10$. Different coloured markers denote the (renormalisation group improved) THA results corresponding to different values of n_{max}. The THA shows minimal truncation effects. The continuous line denotes the SCA, which fails to predict the amplitudes of the oscillations correctly.

Note, however, that despite the good agreement between the temporal frequencies in the case of higher Fourier modes, there is still some discrepancy present between the amplitudes of the correlator. A possible source of the difference can be the truncation errors of the THA since it is expected that the method becomes unreliable whenever the time evolution of an observable contains high frequencies close to energy cutoff Λ. To rule out this possibility, we show the cutoff dependence of $C_2(4, t)$ in Fig. 6.4 and see that the amplitudes of the correlator are minimally subjected to truncation effects. The only alternative option remains the lack of higher-order correlations in the SCA calculations, leading to an overshoot in the amplitudes.

These findings can be further demonstrated by considering quenches with a larger change in the mass parameter, shown in Fig. 6.5. The setting can be considered a stronger quench because the post-quench energy density is higher, in principle reducing the effectiveness of the truncated Hamiltonian approach [117]. However, as discussed previously in Sec. 6.1, for the quenches studied here, the THA can be considered to have converged, providing practically exact results for the time evolution. The SCA is exact for pure mass quenches (λ_0 and λ set to zero), and we do not expect very different results from before. Indeed, looking at Fig. 6.5, we see a similar behaviour, with the two methods agreeing for small values of the coupling and the SCA providing less reliable results for both the temporal frequencies and amplitudes as the strength of the quartic interaction is increased.
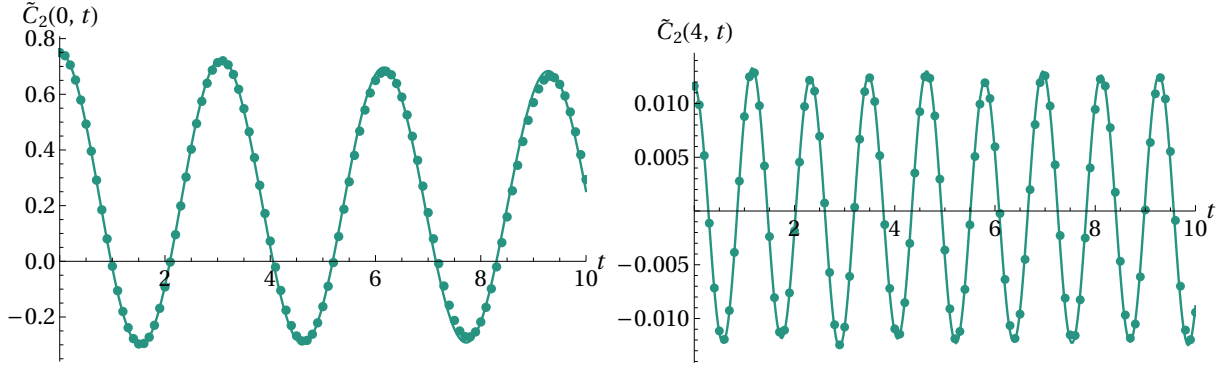
(a) $(m_0, \lambda_0) = (0.4, 0) \rightarrow (m, \lambda) = (1, 1)$
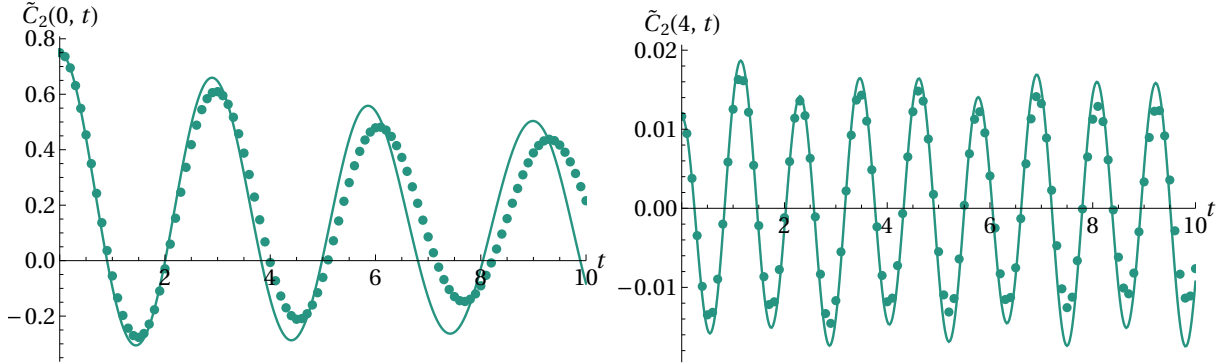
(b) $(m_0, \lambda_0) = (0.4, 0) \rightarrow (m, \lambda) = (1, 4)$
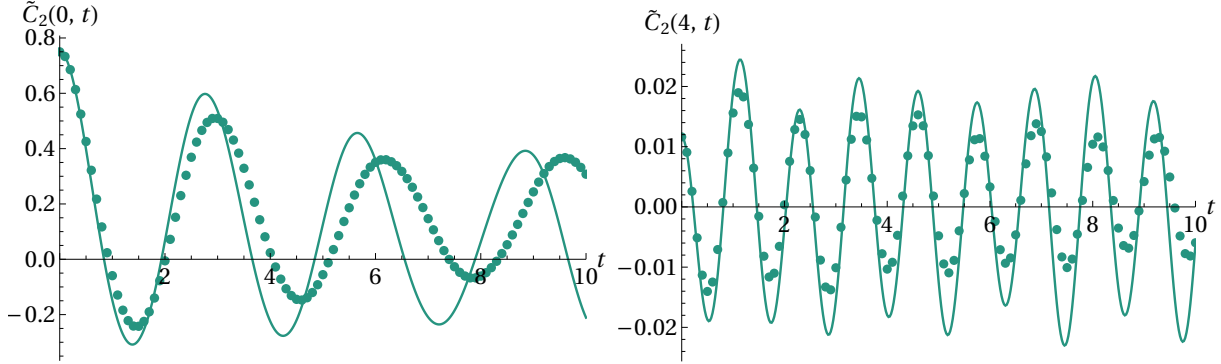
(c) $(m_0, \lambda_0) = (0.4, 0) \rightarrow (m, \lambda) = (1, 7)$

Figure 6.5: Same as 6.2 but for stronger quenches $m_0 = 0.4 \rightarrow m = 1$ with different values of the post-quench coupling for $l = 10$. The THA data is computed using $n_{\max} = 21$ together with the renormalisation group improvement and is displayed by dots. The SCA results are denoted via continuous lines.

6.3 TWA vs. THA

For the quenches considered here, the initial state is the ground state of the massive free boson with $\lambda = 0$, which is described by a simple Gaussian Wigner function:

$$W = \prod_{k=0,\pi/a} \frac{1}{\pi} \exp\left(-\frac{\varphi_k^2}{2\sigma_k^2} - 2\sigma_k^2 \pi_k^2\right) \prod_{0<k<\pi/a} \frac{4}{\pi^2} \exp\left(-\frac{\varphi_k \varphi_{-k}}{\sigma_k^2} - 4\sigma_k^2 \pi_k \pi_{-k}\right) . \quad (6.9)$$

Here σ_k denotes the variance appearing in Eq. (4.20),

$$\sigma_k = \frac{1}{2\,a\,\omega_{k,0}^{\text{latt}}} \,,$$

and $\omega_{k,0}^{\text{latt}}$ is given by

$$\omega_k^{\text{latt}} = \sqrt{\left(\frac{2}{a}\sin\frac{ka}{2}\right)^2 + m_0^2} , \quad (6.10)$$

calculated with the initial (renormalised) mass m_0.

As before, we focus on the correlator

$$C_2(k,t) = a\,\langle : \hat{\varphi}_k(t)\hat{\varphi}_{-k}(t) : \rangle = a\,\langle \hat{\varphi}_k(t)\hat{\varphi}_{-k}(t)\rangle - \frac{1}{2\,\omega_k^{\text{latt}}} \quad (6.11)$$

with ω_k^{latt} given in Eq. (6.10), using the renormalised post-quench mass m. The lattice constant a is inserted to match the dimensions of the continuum theory, which is necessary for comparing the TWA with the THA. The Wigner transform of the correlator can be computed trivially by simply substituting the operators with the classical variables:

$$C_{2,W}(k,t) = \varphi_k(t)\varphi_{-k}(t) - \frac{1}{2\,\omega_k^{\text{latt}}} \,. \quad (6.12)$$

Comparison of the TWA to the THA was carried out similarly to the previous Section: we performed general mass and coupling quenches in the φ^4 model, with the initial coupling set to $\lambda = 0$ and the post-quench mass set to $m = 1$ in volume $Lm = 10$. In all results going forward, the THA can be considered practically exact and serve as a good benchmark for validating the TWA results.

For small enough values of λ, the TWA produces good results that agree with the THA, as shown in Fig. 6.6a, displaying the zero mode of the correlator $C_2(0,t)$ for a quench $(m_0 = 0.4, \lambda_0 = 0) \to (m = 1, \lambda = 1)$. However, increasing the strength of the interactions λ, notable deviations appear between the TWA and the THA, pointing to the breakdown of the semi-classical method. Contrary to the reliable results of the THA, the TWA data shows strong damping in the oscillations and a relaxation of the correlator zero mode to some non-zero value. Besides leading to faster damping, the stationary value also increases with the coupling λ, as shown in Figs. 6.6c and 6.6e for quenches with $\lambda = 1$ and 8. For the largest value of the coupling $\lambda = 8$ studied here, the TWA significantly overestimates the damping to the point where the correlator practically relaxes completely to a steady state. Similar behaviour can be found for quenches with a larger change in the mass parameter
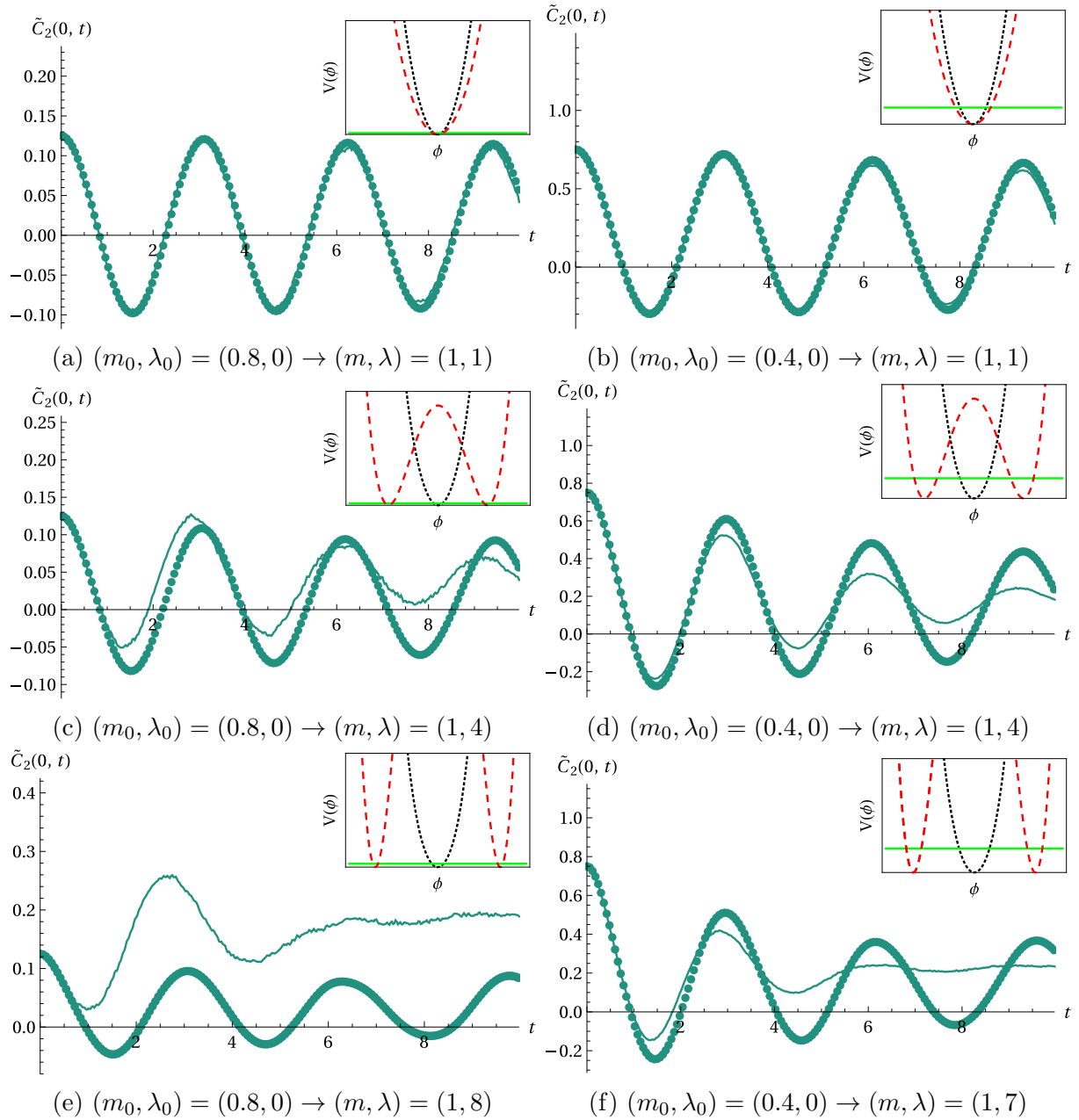
Figure 6.6: THA (dots) and TWA (solid lines) results for the time evolution of the correlator $\tilde{C}_2(k=0,t)$ for quenches corresponding to weak/intermediate/strong interactions and two different values for the mass shift and $l = 10$. The TWA results were computed using $N_s = 400$. In the THA we applied a cutoff $n_{\max} = 21$ (including the leading RG improvement). The insets compare energy density injected by the quench (green solid line) with the THA (dotted black line) and the TWA potential (dashed red line). The injected energy density is computed as $\Delta \mathcal{E} = (\langle \psi_0 | H | \psi_0 \rangle - E_0^{(1)})/L$ where $E_0^{(1)}$ is the vacuum energy of H.

60

$m_0 = 0.4 \rightarrow m = 1$, corresponding to a larger post-quench energy density that, in theory, should benefit the semi-classical TWA. Though true to some extent in light of the previous results, the systematic over-damping is still present in the TWA data, with a quick relaxation to some non-zero value of the correlator, as seen in Figs. 6.6b, 6.6d and 6.6f for the cases of $\lambda = 1, 4$ and 7.

The systematic overdampening and the general failure of the TWA for sufficiently large values of λ can be traced back to the sensitivity of the time evolution to mass renormalisation. As described previously in Section 4.2, the semi-classical TWA is formulated in terms of the bare mass m_{bare}^2

$$m_{\mathrm{bare}}^2 = m^2 - \frac{\lambda}{4N_s a} \sum_k \frac{1}{\omega_k^{\mathrm{latt}}}, \tag{6.13}$$

as opposed to the renormalised post-quench mass m. For large enough values of λ, m_{bare}^2 becomes negative, corresponding to a symmetry-broken theory with the classical vacuum expectation value $\varphi_j = -6m_{\mathrm{bare}}^2/\lambda$ as shown in the insets of Figs. 6.6c to 6.6f. The equations of motion (4.28) predict a fast relaxation of the correlator C_2 to some finite value, causing the emergence of a symmetry-broken classical steady state in the dynamics. This is contrasted to the THA, where the mass term entering the equations governing the time evolution is given by the (positive) renormalised mass m^2, Consequently giving rise to much weaker relaxation in the dynamics. Besides the strength of interactions, this effect also depends on the post-quench energy density $\Delta\mathcal{E}$, which can be tuned by varying the pre-quench mass m_0 while keeping the post-quench mass m and coupling λ fix to preserve the shape of the post-quench potentials within the methods. For smaller values of $\Delta\mathcal{E}$, the classical trajectories in the TWA are localised closer to the vicinity of the non-physical minima of the potential, as shown in the insets of Figs. 6.6c to 6.6f, resulting in the emergence of the symmetry-broken classical steady state. For larger values of the post-quench energy density, a higher number of classical trajectories further from the minima contribute to the TWA averaging, somewhat obscuring the effects of the classical symmetry breaking.

This effect can be investigated more closely by considering the time-averaged correlator

$$\langle \tilde{C}_2(k,t) \rangle_t = \frac{1}{T} \int_0^T \mathrm{d}t\, \tilde{C}_2(k,t), \tag{6.14}$$

where T is chosen as the total time of the first three full oscillations of the correlator $C_2(k,t)$. Fig. 6.7 shows results for $\langle \tilde{C}_2(0,t) \rangle_t$ as a function of the bare mass (6.13) for quenches with a fix value of m_0 and m and varying λ. For the smaller quenches presented in Fig. 6.7a, the TWA agrees well with the THA as long as m_{bare}^2 is positive, with a progressively growing difference between the two methods as the m_{bare}^2 increasingly negative, corresponding to the non-physical classical symmetry breaking within the TWA. Similar agreement can be found for positive values of m_{bare}^2 for quenches corresponding to higher post-quench energy density. However, the two methods show different behaviour for $m_{\mathrm{bare}}^2 < 0$, with the correlator average growing in the TWA and steadily decreasing in the THA. These findings strongly support the idea that the over-dampening present in the TWA is due to the negative bare mass entering the classical equations of motion and as such, a non-physical artefact driven by the mass renormalisation, rendering the TWA unreliable whenever λ is sufficiently large.
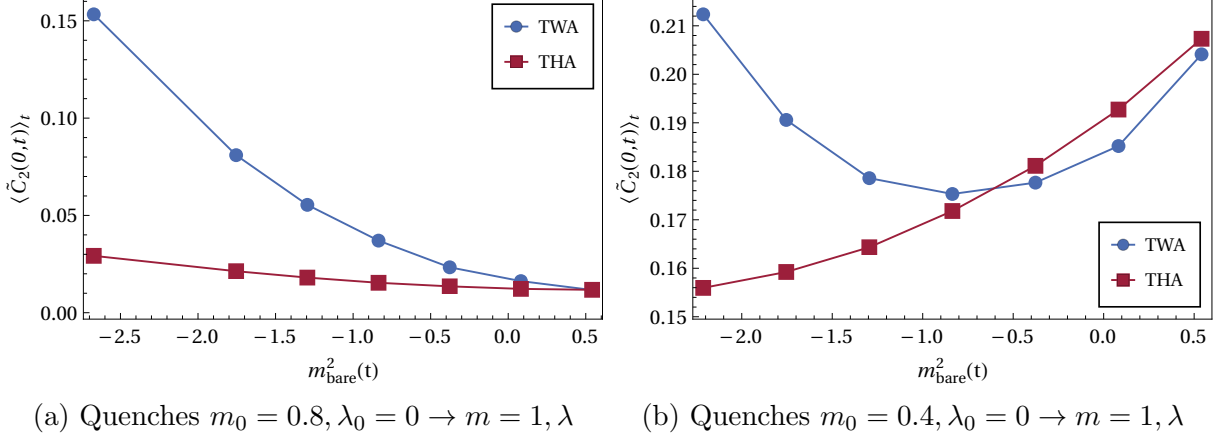
(a) Quenches $m_0 = 0.8, \lambda_0 = 0 \to m = 1, \lambda$ (b) Quenches $m_0 = 0.4, \lambda_0 = 0 \to m = 1, \lambda$

Figure 6.7: The time-averaged correlator $\langle \tilde{C}_2(k = 0, t) \rangle_t$ as a function of the bare mass m_{bare}^2 (6.13), calculated using the TWA (blue circles) and THA (red squares), for $l = 10$ and different values of the coupling λ. For $m_{\mathrm{bare}}^2 > 0$, the methods show a good agreement but start to deviate when $m_{\mathrm{bare}}^2 > 0$ becomes negative due to the increasing λ. The TWA results are computed using $N_s = 400$. The THA cutoff was set to the largest available value $n_{\mathrm{max}} = 21$ (including the leading RG improvement).

Here we briefly mention that the TWA has also been applied to the sine-Gordon model [173], and more importantly, it has been compared to the truncated Hamiltonian approach [115,174]. In those studies, the instability to the mass renormalisation in the TWA is entirely absent. This is because in the sine-Gordon model, renormalisation works very differently than in the φ^4 theory. The sine-Gordon model is given by the Hamiltonian:

$$\hat{H}_{\mathrm{sG}} = \int dx \left(\frac{1}{2} \hat{\pi}^2 + \frac{1}{2} (\partial_x \hat{\varphi})^2 - \lambda : \cos \beta \hat{\varphi} : \right) \tag{6.15}$$

and the normal ordering corresponding to renormalisation is done with respect to the free massless boson modes, described by the first two terms of the Hamiltonian. Therefore, instead of the addictive mass shift (6.13) present in the φ^4 theory, in the sine-Gordon model, normal ordering leads to the multiplicative renormalisation of the coupling λ [115]. This procedure keeps the shape of the potential fixed, admitting no change in the sign of the mass term, and as a result, the TWA stays stable against the effects of renormalisation.

6.4   Summary

We investigated the out-of-equilibrium dynamics in the $\mathbb{Z}_2-$symmetric phase of the φ^4 theory by simulating quantum quenches using three distinct methods: the truncated Hamiltonian approach (THA), the self-consistent approximation (SCA) and the truncated Wigner approximation (TWA). We considered quench protocols where the system is initially prepared in the ground state of the free massive boson with pre-quench mass m_0 and then is evolved in time by the interacting Hamiltonian with some different post-quench mass m and non-zero interaction strength λ. The methods were compared by computing the time evolution of the Fourier modes of the two-point function (6.5).

The truncated Hamiltonian approach used here is formulated in a finite volume L, built upon the Fock space of the massive free boson with $m = 1$, concurrently chosen as the post-quench value. The method shows very little dependence on the large cutoff values studied, and together with the leading order renormalisation group improvement, it is considered converged, practically yielding exact results for the dynamics. The observables studied here exhibit very slow relaxation, consistent with the observation [84] that the φ^4 interaction is a weakly integrability breaking perturbation [84, 85].

The self-consistent approximation is expected to provide reliable results whenever the interaction strength λ is sufficiently small but breaks down when the value of the coupling becomes high, and the connected part of the four-point correlations can not be neglected anymore to reproduce the quantum evolution. Accordingly, our SCA simulations break down for relatively small values of the coupling $\lambda \gtrsim 4$ (indeed, according to Fig. 4.1, this is just outside of the range validity of the perturbation theory). In the literature, the SCA is applied to systems with much larger coupling parameters [111], where it fails to reproduce the temporal frequencies and amplitudes present after the quench: the post-quench frequencies show signs of strong $k-$dependence, with the deviations becoming smaller for high modes k, pointing to the incorrect determination of the effective mass. Here, we remark that since the SCA is formulated as a semi-classical approximation of quantum field theories, an obvious improvement is taking into account higher-order quantum correlations using an approach such as the 2PI effective action [109], a promising direction for which the THA demonstrated here can serve as an efficient tool for validation.

The truncated Wigner approximation is formulated using the lattice regularised form of the theory. The TWA equations of motion contain the bare mass, which is renormalised by quantum fluctuations via normal ordering of the Hamiltonian. By comparing the TWA to the THA, we found that the former fails to correctly reproduce the exact quantum time evolution whenever the bare mass m_{bare}^2 becomes negative, resulting in an overestimated relaxation to a symmetry-broken classical steady state. This observation is relevant for other models that exhibit phase transitions and additive renormalisation of the control parameter, such as other Ginzburg-Landau theories.

These results establish the THA as a very accurate and powerful tool for studying out-of-equilibrium dynamics in interacting low-dimensional quantum field theories, such as the φ^4 model, and provide a point of reference for the validity of semi-classical approaches in interacting quantum field theories.

Chapter 7

False vacuum decay in the φ^4 model

After the out-of-equilibrium dynamics of the φ^4 model in the $\mathbb{Z}_2$-symmetric phase, we now focus on the symmetry-broken phase. Classically, whenever the sign of the mass term in the Hamiltonian

$$H = \int dx \left[\frac{1}{2}(\partial_t \varphi)^2 + \frac{1}{2}(\partial_x \varphi)^2 - \frac{1}{2}m^2\varphi^2 + \frac{g}{6}\varphi^4 \right] \tag{7.1}$$

becomes negative, the theory admits two degenerate minima of the potential

$$\varphi_\pm = \pm\sqrt{\frac{3m^2}{2g}} \, . \tag{7.2}$$

In the quantum regime, the scalar field φ turns into the scalar operator $\hat{\varphi}$ and the change in the sign of the mass term in (7.1) corresponds to spontaneous symmetry breaking, resulting in two degenerate vacua upon which the Hilbert space of the theory is built.

Perturbing the system with an odd function of the field $\hat{\varphi}$ breaks the $\mathbb{Z}_2$ symmetry explicitly, lifting the degeneracy between the minima of the potential. Though stable classically against small perturbations, the local minimum with the higher energy in the quantum regime corresponds to a metastable state of the system, called the *false vacuum*, susceptible to decay via quantum mechanical tunnelling [175, 176]. The decay is driven through nucleation of bubbles of *true vacuum* (the true ground state of the theory) via tunnelling across the volume and expanding propelled by the energy difference between the true and the false vacuum. The released energy (latent heat) excites a sea of particles above the true ground state, filling the domains of the volume with the true vacuum present.

The decay of the false vacuum has gained considerable attention lately due to indications of the metastability of the Higgs vacuum [77, 177]. Apart from its significance in cosmology and high-energy physics, recent advances in ultracold atomic experiments opened the possibility of directly observing the phenomenon in experimental condensed matter settings [178–183]. The main quantity of interest is the tunnelling or decay rate of the false vacuum, with theoretical results available with multiple degrees of precision, depending on the approximation used, the microscopic details and the dimensionality of the system [175–177, 184–188].

We simulate the false vacuum decay in the $\mathbb{Z}_2$-broken (1+1)-dimensional φ^4 model by performing quantum quenches and analysing the subsequent time evolution of the order

parameter. Studying the real-time quantum evolution non-perturbatively via the truncated Hamiltonian approach (THA) allows us to numerically determine the bubble nucleation rate and compare it to existing analytical formulae in the literature. Subsequently, the results establish the THA as a powerful tool to study strongly non-perturbative phenomena far from equilibrium in interacting quantum field theories, such as false vacuum decay.

Here, we briefly introduce the elements of false vacuum decay necessary for later discussions in Section 7.1. Then, we discuss the quench setup applied to study the false vacuum decay in Section 7.2 and present our results in Section 7.3. We close by giving our conclusions in Section 7.4.

7.1 Semi-classical treatment of false vacuum decay

Now, we briefly review the false vacuum decay necessary for our investigation. Though applicable to higher dimensions, we formulate the theory with a specific focus on (1+1)d quantum field theories. A system stuck in the false vacuum decays through nucleation of predominantly spherical bubbles of true vacuum induced by quantum fluctuations. Bubbles not reaching a critical size only appear as short-lived quantum fluctuations due to the finite energy (a.k.a. surface tension) of the bubble walls. However, bubbles with sizes exceeding the critical size are energetically favourable and form long-lived field configurations. Due to the excess energy, they begin to expand, accelerating rapidly and converting more and more of the false vacuum into the true ground state, giving rise to an abundance of quasi-particle excitations above the true vacuum in the process. Following Coleman's ground-breaking works, [175, 176] a semi-classical treatment of the process starts with a potential $U(\varphi)$ with a local and a global minimum, corresponding to the false and true vacua, respectively. The nucleation of the critical bubble can be described in terms of the instanton bounce, a non-perturbative and spherically symmetric field configuration satisfying the Eucledian equation of motion:

$$\left(\frac{\partial^2}{\partial \tau^2} + \nabla^2 \right) \varphi = \frac{\partial U}{\partial \varphi} \tag{7.3}$$

with appropriate boundary conditions. This treatment allows for the expression of the bubble nucleation rate per unit volume γ

$$\gamma = \frac{\Gamma}{L} = A \exp\left[-\frac{1}{\hbar} S_{\mathrm{E}} \right] \tag{7.4}$$

as a function of the Euclidean action of the instanton bounce S_{E}. The prefactor A can be written as a fraction of determinants of the quantum fluctuations on the instanton background with special care of the zero mode. To simplify the calculation, it is useful to restrict our attention to the limit when the bubble walls' thickness is much smaller than the bubble radius, which is called the thin-wall approximation. It allows for the expansion of the potential $U(\varphi)$ as

$$U(\varphi) = U_0(\varphi) + \varepsilon \Delta U(\varphi) , \tag{7.5}$$

with the potential U_0 being symmetric, with two degenerate local minima corresponding to quantum mechanical ground states with equal energy density. When ε is greater than zero,

65

the second term explicitly breaks the symmetry of the theory, lifting the degeneracy between the vacua. The thin-wall limit corresponds to the limit of small $\varepsilon > 0$ [175]. In (1+1)d, the bubble is formed by a kink-antikink pair, extrapolating between two points of false vacua with the true vacuum in the inside region. Simple energy conservation leads to the size of the critical bubble:

$$a_* = \frac{2M}{\mathcal{E}} \, , \tag{7.6}$$

where M is the mass of the (anti)kink, corresponding to the energy stored in the walls of the bubble, and $\mathcal{E}$ is the energy density difference between the false and true vacua:

$$\mathcal{E} = \frac{1}{L} \left(E_{\mathrm{FV}} - E_{\mathrm{TV}} \right) . \tag{7.7}$$

In the thin-wall limit, the action corresponding to a bubble with diameter a is given by [175]

$$S(a) = \pi a M - \frac{\pi a^2}{4} \mathcal{E} \, . \tag{7.8}$$

The stationary point of (7.8) is exactly at the critical radius $a = a_*$, meaning that bubbles of the size around the critical size have the highest chance of nucleation. As a result, the instanton action determining the tunnelling rate can be semi-classically approximated by

$$S_{\mathrm{E}} = \frac{\pi M^2}{\mathcal{E}} \, . \tag{7.9}$$

Coleman eventually went beyond the semi-classical limit by including quantum corrections up to leading order [176]. Moreover, fluctuations up to all orders were summed up in 1+1 dimensions independent of microscopical parameters by Voloshin [184]:

$$\gamma = \frac{\mathcal{E}}{2\pi} \exp\left[-\frac{\pi M^2}{\mathcal{E}} \right] , \tag{7.10}$$

where M is the exact (renormalised) mass of the kink and $\mathcal{E}$ is the exact energy density difference between the false and true vacua.

7.2   Quench setup for false vacuum decay

In the symmetry broken phase, the φ^4 theory is described by the Hamiltonian

$$\hat{H} = \int dx : \left[\frac{1}{2}(\partial_t \hat{\varphi})^2 + \frac{1}{2}(\partial_x \hat{\varphi})^2 - \frac{1}{2}m^2 \hat{\varphi}^2 + \frac{g}{6} \hat{\varphi}^4 \right] : \tag{7.11}$$

with $m^2, g > 0$. Spontaneous symmetry breaking corresponds to the emergence of a pair of degenerate ground states $|\Psi\pm\rangle$. Perturbing the system by applying an external field ε coupled to $\hat{\varphi}$

$$\hat{H}_\varepsilon = \int dx : \left[\frac{1}{2}(\partial_t \hat{\varphi})^2 + \frac{1}{2}(\partial_x \hat{\varphi})^2 - \frac{1}{2}m^2 \hat{\varphi}^2 + \frac{g}{6} \hat{\varphi}^4 - \varepsilon \hat{\varphi} \right] : \tag{7.12}$$

explicitly breaks the $\mathbb{Z}_2$ symmetry, lifting the degeneracy between the ground states. Note, however, that the positions of the local minima are also shifted due to the perturbation.

To study the false vacuum decay in the φ^4 theory, we perform quantum quenches and study the subsequent time evolution. In our protocol, we initialise the system in the ground state $|\Psi_-\rangle$ of $\hat{H}$, corresponding to the false vacuum when the symmetry breaking parameter $\varepsilon > 0$ is switched on:

$$|\Psi(0)\rangle = |\Psi_-\rangle$$
$$\hat{H}|\Psi_-\rangle = E_0|\Psi_-\rangle \quad , \quad \langle\Psi_-|\varphi|\Psi_-\rangle < 0 \,. \tag{7.13}$$

At $t = 0$, $\varepsilon > 0$ is switched on, resulting in unitary time evolution starting from the close vicinity of the false vacuum, governed by the post-quench Hamiltonian $\hat{H}_\varepsilon$:

$$|\Psi(t)\rangle = e^{-iH_\varepsilon t}|\Psi(0)\rangle \,. \tag{7.14}$$

In the following, we focus on the time evolution of the order parameter, that is, the expectation value of the field $\hat{\varphi}$. To gain a better proxy for the decay, we use the parameterization

$$F(t) = \frac{\langle\hat{\varphi}_0(t)\rangle + \langle\hat{\varphi}_0(0)\rangle}{2\langle\hat{\varphi}_0(0)\rangle} = \frac{\langle\Psi(t)|\hat{\varphi}_0|\Psi(t)\rangle + \langle\Psi(0)|\hat{\varphi}_0|\Psi(0)\rangle}{2\langle\Psi(0)|\hat{\varphi}_0|\Psi(0)\rangle} \,, \tag{7.15}$$

with

$$\hat{\varphi}_0 = \frac{1}{L}\int_0^L dx\,\hat{\varphi}(x) \,, \tag{7.16}$$

following a study of a similar setting in spin chains [189]. The decay of the false vacuum roughly corresponds to the change of $F(t)$ from 1 to 0 (neglecting the shift in the vacuum expectation values due to the external field ε), making $F(t)$ a convenient indicator of the decay process.

During the decay $F(t)$ is expected to decrease exponentially:

$$F(t) \propto e^{-\Gamma t} \,, \tag{7.17}$$

Studying the real-time decay of the false vacuum allows us to directly (numerically) obtain the decay rate Γ as a function of the external field ε and compare it with the theoretical prediction (7.10). We apply the THA introduced in Section 4.3.1 built upon the massive free boson eigenstates with mass $m = 1$, complemented by a mini-superspace and identify the decay in the real-time evolution of $F(t)$ via the corresponding linear regime in $\log F(t)$. The slope is proportional to the decay rate Γ and can be obtained via a simple linear fit.

7.3   Results

Here we give our results for the time evolution of the order parameter (7.15) following quantum quenches initiated in the false vacuum using the truncated Hamiltonian approach. Identifying the linear regime in the real-time evolution of $\log F(t)$ allows for the numerical determination of the decay rate for a range of external fields $\bar{\varepsilon}$, which can be compared to the formula (7.10). However, evaluation of (7.10) requires the renormalised (exact) kink mass

67

M and vacuum energy density difference (latent heat) $\mathcal{E}$. Therefore, we first present the THA results for these quantities and then later move on to studying the real-time dynamics. As before, we work in units of $m = 1$ (where m is the mass of the Klein-Gordon field appearing in (7.12) and use periodic boundary conditions when not specified otherwise. The dimensionless parameters (denoted by a 'bar', e.g. $\bar{g}$) are defined in Section 4.3.1.

7.3.1 The kink mass

To obtain the kink mass M we set $\bar{\varepsilon} = 0$ and compute the lowest energy levels in the antiperiodic and periodic boundary conditions within the THA, corresponding to the stationary kink and the vacuum state, respectively:

$$M^{\mathrm{THA}}(\bar{g}) = E_0^{\mathrm{APBC}}(\bar{g}) - E_0^{\mathrm{PBC}}(\bar{g}) \,. \tag{7.18}$$

The $\bar{g}$-dependence of the THA data can be checked against the semi-classical prediction (3.16) [87]

$$M = \frac{\sqrt{2}m^3}{g} - \sqrt{2}m\left(\frac{3}{2\pi} - \frac{1}{4\sqrt{3}}\right) + O(g)\,, \tag{7.19}$$

demonstrated in Fig. 7.1. For small coupling, the kink mass is large; therefore, its value is comparable to the cutoff Λ, making the THA determination less precise. For larger values of $\bar{g}$, the THA provides a very good approximation for the renormalised kink mass.
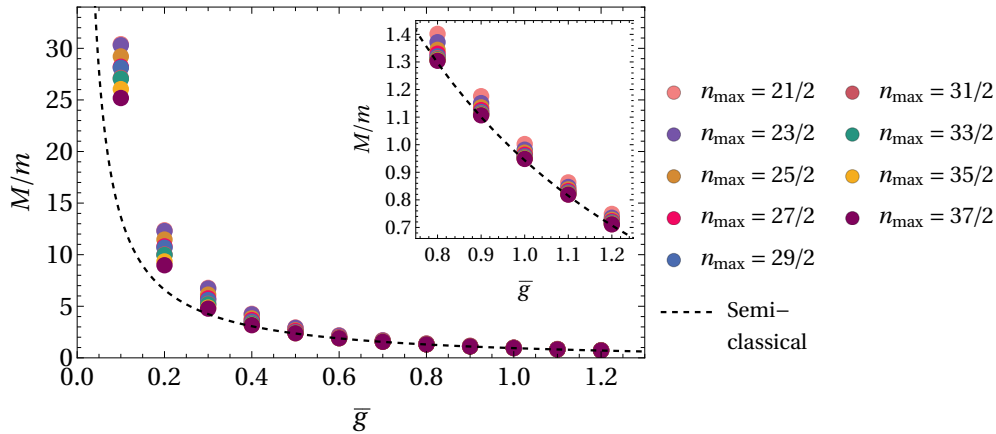

Figure 7.1: The kink mass as computed by the THA (markers) together with the semi-classical prediction (3.16) as a function of the coupling $\bar{g}$. Different colours correspond to different cutoff values $n_{\mathrm{max}} = 21/2, ...37/2$ corresponding to cc. 1000-100000 computational basis states.

7.3.2 The latent heat

The latent heat $\mathcal{E}$, defined as the energy density difference between the false and the true vacua (7.7), is easily obtainable from the THA by diagonalising $\hat{H}_\varepsilon$ (7.12). However, as the false vacuum is a metastable state, it is not an eigenstate of the Hermitian Hamiltonian $\hat{H}_\varepsilon$.
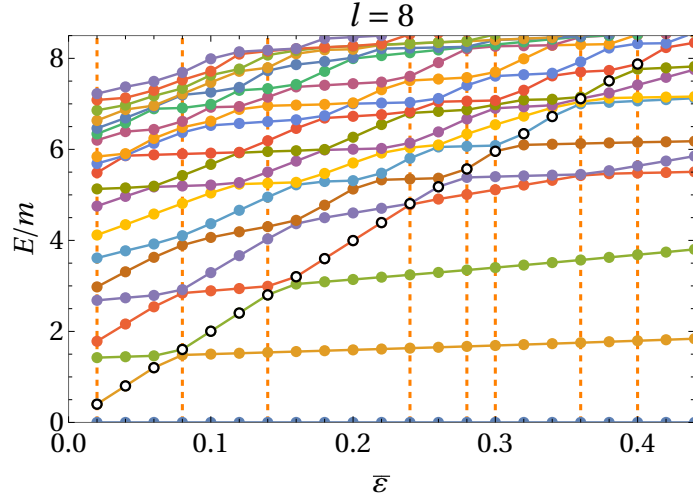
Figure 7.2: Representative spectrum of H_ε as a function of the symmetry breaking parameter for $l = 8$ and $\bar{g} = 1.1$ with the true vacuum energy substracted. The false vacuum is displayed by open black markers.

Accordingly, in order to compute its energy $E_{\text{FV}}(\varepsilon, L)$ it has to be identified by looking at the spectrum of $\hat{H}_\varepsilon$ for fixed volumes l and varying $\bar{\varepsilon}$, following the example shown in Fig. 7.2 for $\bar{g} = 1.1$ and $l = 8$. Computing $E_{\text{FV}}(\varepsilon, L)$ now requires repeating the above procedure for numerous values of the volume L. The energy of the true ground state $E_{\text{TV}}(\varepsilon, L)$ can also be straightforwardly obtained, given by the lowest-lying eigenvalue of $\hat{H}_\varepsilon$ for a fixed $\bar{\varepsilon}$ and different values of the volume. Taking the difference for a fixed value of $\bar{\varepsilon}$, it is extensive with the system size, and the latent heat (7.7) corresponds to the slope of the lines as a function of L, illustrated for $\bar{g} = 1, 1$ and a variety of $\bar{\varepsilon}$ values in Fig. 7.3. In Fig. 7.4, the latent heat can be seen as a function of $\bar{\varepsilon}$ for various quartic couplings $\bar{g}$. For the small values of $\bar{\varepsilon}$ studied here, the latent heat is linear in accordance with the first-order perturbation theory predictions. Therefore, the latent heat can be parametrised as

$$\mathcal{E} = A(\bar{g})\bar{\varepsilon} \tag{7.20}$$

by fitting a linear curve and extracting $A(\bar{g})$ for various values of $\bar{g}$. Our calculations were carried out with around 1000 non-zero modes and 11 mini-superspace basis states, providing adequate accuracy for our needs.

We note here that for larger values of ε, the latent heat is not expected to be linear in ε, as higher-order perturbative corrections come into play. However, the prediction (7.10) is only valid in the thin-wall limit corresponding to small values of $\bar{\varepsilon}$ in the setup considered here. Therefore, our computation is restricted to the perturbative regime where (7.20) is valid.

7.3.3 Time evolution and the decay rate

Now that we have the renormalised kink mass and latent heat required to evaluate (7.10), we turn our focus to acquiring the bubble nucleation rate γ through simulating the real-time
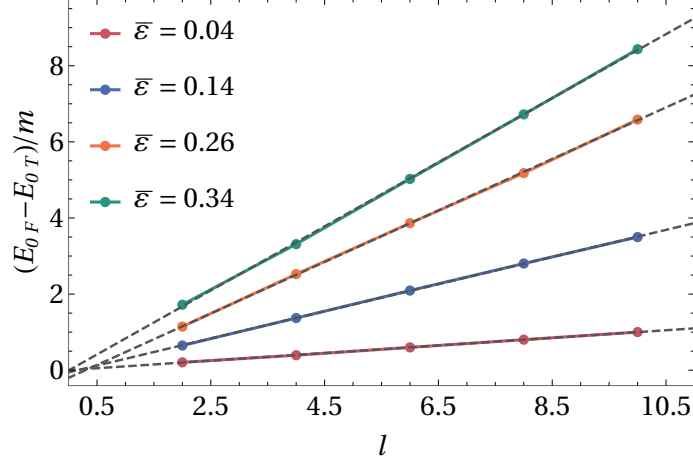
Figure 7.3: The energy difference between the false and true vacuum against the volume l for $\bar{g} = 1.1$. The slopes of the linear fitted curves correspond to the energy density difference (latent heat) $\mathcal{E}$ for various values of the symmetry breaking field ε.
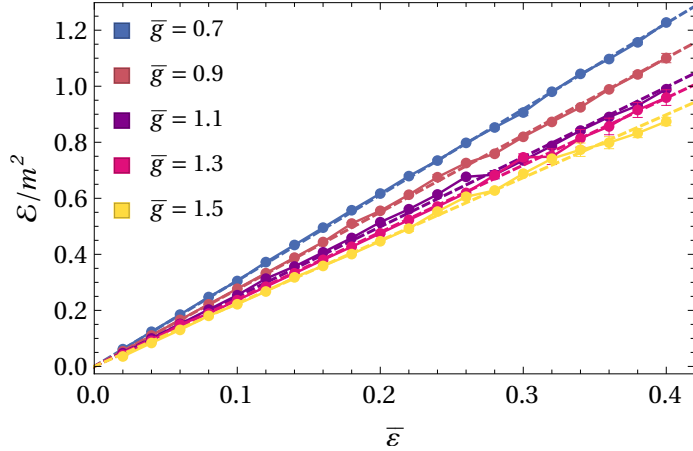

Figure 7.4: The energy density difference between the false and true vacuum (latent heat) $\mathcal{E}$ as a function of $\bar{\varepsilon}$ for various couplings $\bar{g}$ with the fitted linear dependence. The error bars are obtained from the parameter estimation uncertainty from the fits shown in Fig. 7.3 and only represent a crude estimate of the eventual errors.

quantum evolution via THA following the quench setup described in Section 7.2. However, executing the procedure requires some prior considerations due to the limited validity of the THA with regard to the values of $\bar{\varepsilon}$. Firstly, the value of $\bar{\varepsilon}$ must be chosen such that the size of the critical bubble (7.6) is smaller than the system size L by at least a couple of factors of the correlation length (in the order of $\sim 1/m$), to avoid finite size effects. This condition gives a lower bound for the values of $\bar{\varepsilon}$, limiting the available regime where the decay of the false vacuum can be studied, which depends on the self-interaction parameter $\bar{g}$. Secondly, to ensure that the false vacuum state is properly represented in the THA, it must fit below the UV cutoff Λ, limiting the available ε to values that fulfil $\mathcal{E} = A(\bar{g})\bar{\varepsilon} \ll \Lambda$ in our subsequent calculations, imposing an upper bound for $\bar{\varepsilon}$, which depends on the value of $\bar{g}$.
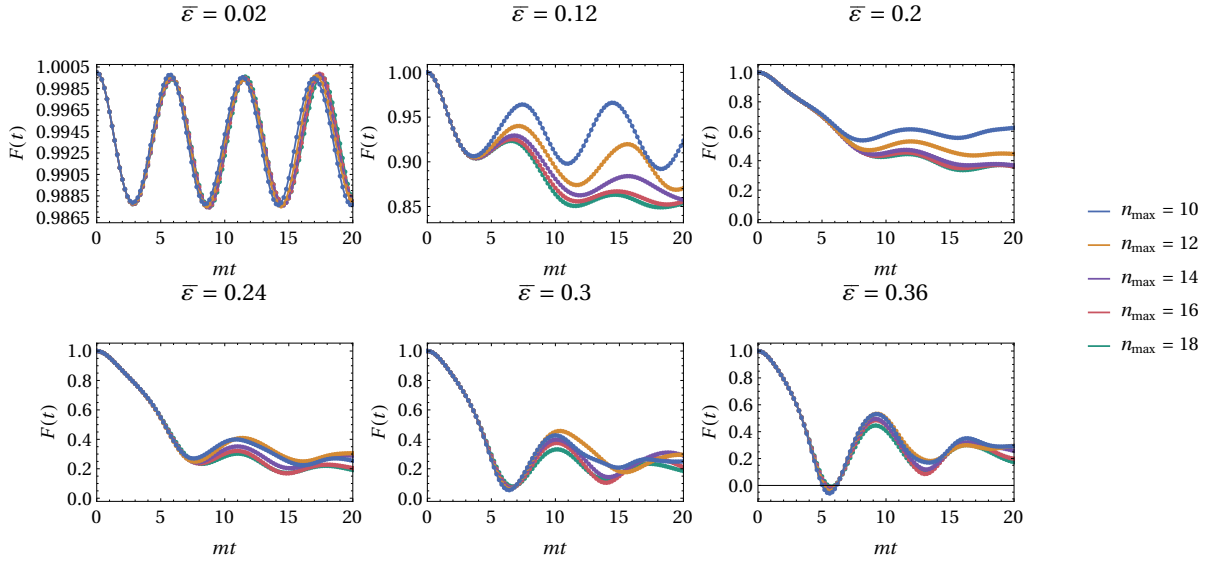
Figure 7.5: Time evolution of the order parameter $F(t)$ for $\bar{g} = 1.1$ and different values of ε. The different colours correspond to different cut-off values: $n_{\max} = 10, 12, 14, 16$ and 18 corresponding to cc. $4100 - 287000$ states.
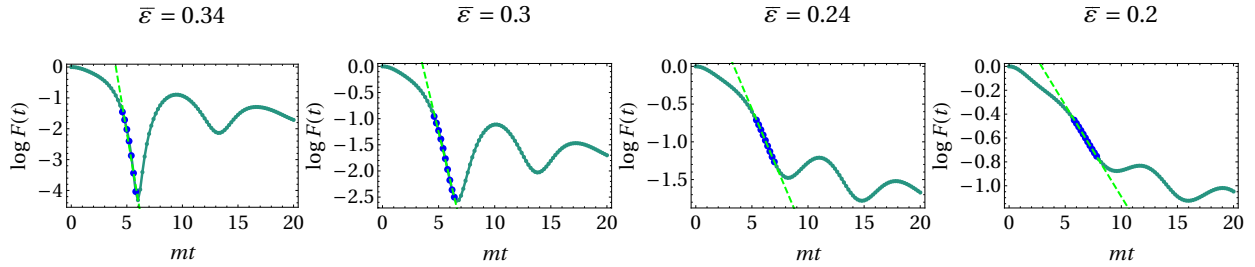
Figure 7.6: Obtaining the tunnelling rate Γ from the logarithm of $F(t)$ for $l = 20$ and $\bar{g} = 1.1$ obtained with the largest cut-off $n_{\max} = 18$. Fitting the tunnelling regimes indicated by the linear drop, the fitted slopes correspond to the tunnelling rate Γ.

In our simulations, we use a volume $l = 20$ and choose values of $\bar{g}$ such that the region of $\bar{\varepsilon}$ available is wide enough to study the dependence of the nucleation rate on $\bar{\varepsilon}$. We use a mini-superspace dimension of 41, for which the results converged and showed stable behaviour against increasing the cutoff. The non-zero mode cutoff $n_{\max}$ is chosen to be $n_{\max} = 10, 12, 14, 16$ and 18 to monitor better the validity of the THA, corresponding to Hilbert space dimensions up to cc. 4100 to 287000.

The time evolution of the order parameter $F(t)$ is presented in Fig. 7.5 for $\bar{g} = 1.1$ and a selection of values of the symmetry breaking parameter $\bar{\varepsilon}$ and cutoffs values. When $\bar{\varepsilon}$ is small, the resonant bubble size exceeds the volume, leading to dynamics exhibiting persistent oscillations dominated by the quasi-particles and sub-critical bubbles. Increasing the strength of the symmetry breaking $\bar{\varepsilon}$ changes the nature of the dynamics: at short times $t \geq 0$, the behaviour of $F(t)$ is quadratic, dominated by the Zeno effect [190, 191]. This is followed by a time window of exponential decay of the order parameter, as signalled by the linear descent of $\log F(t)$, shown in Fig. 7.6. However, the exponential behaviour is limited in time, and it is soon followed by oscillations exhibiting mild decay, corresponding to the oscillations above the true vacuum, though the limited time window restricts its thorough study. Note, however, that the exponential behaviour is limited even in the absence of the oscillating regime, as the finite volume formulation of the THA restricts us to only study the dynamics for $t \leq L$, as for $t > L$ particles travelling around the system results in unwanted finite size effects. At later times, further restrictions arise from the complicated dynamics involving the expansion and collision of nucleated bubbles and the subsequent thermalisation of the densely populated medium. Despite these effects, we can find a finite time window where the time evolution of $F(t)$ displays exponential behaviour, corresponding to simple bubble nucleation dynamics.

We determine the tunnelling rate γ by plotting the logarithm of $F(t)$ against t and determining the slope of the linear segment by curve fitting. This was performed for various values of $\bar{g}$ and $\bar{\varepsilon}$ to obtain γ as a numerical function of the parameters. Some representative plots are presented in Fig. 7.6 for $\bar{g} = 1.1$ and $l = 20$. For large values of the symmetry-breaking parameter, the linear segment is simple to identify, while for small values of $\bar{\varepsilon}$, the identification can be helped by following the time evolution by gradually changing $\bar{\varepsilon}$ from larger values to smaller ones. The obtained slopes correspond to the extensive nucleation rate Γ that can be divided by the volume L to acquire the nucleation rate per unit volume γ shown in Fig. 7.7 for $l = 20$ and various values of the coupling $\bar{g}$. Fig. 7.7 also contains the theoretical predictions, displayed as dashed lines

$$\gamma = C(\bar{g}) \frac{\mathcal{E}}{2\pi} \exp \left[-\frac{\pi M^2}{\mathcal{E}} \right], \tag{7.21}$$

where the renormalised kink mass M and exact latent heat $\mathcal{E}$ are extracted from the THA as discussed before in this section. The formula (7.21) differs from Voloshin's original prediction (7.10) [184] by an inclusion of a $\bar{g}$-dependent factor $C(\bar{g})$. $C(\bar{g})$ is essentially a fitting parameter used to translate the theoretical predictions to overlay the numerical results, which can be done independently of the value $\bar{\varepsilon}$. Subsequently, this procedure leaves the dependence on the symmetry-breaking parameter unchanged, which is very well reproduced by the THA. Also, the inclusion of a $\bar{g}$ dependent factor is eventually expected, following a similar study [189], where the false vacuum decay was investigated in the transverse field
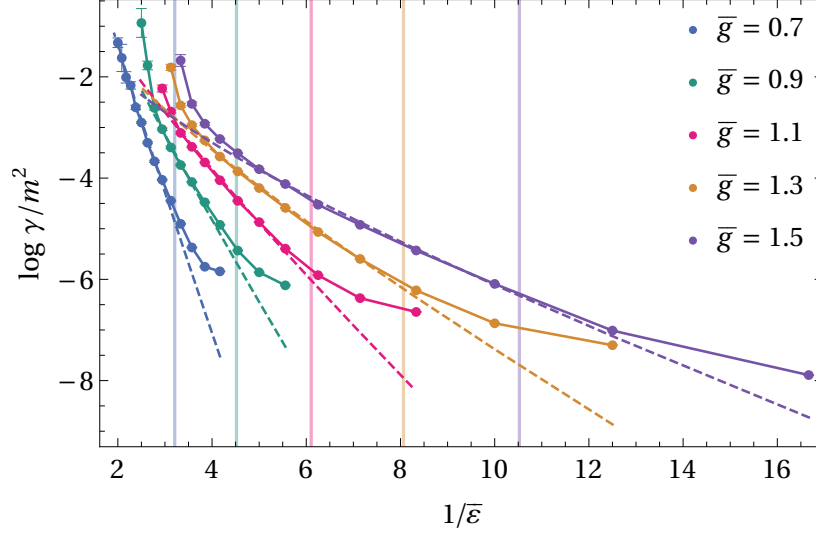
Figure 7.7: The logarithm of the tunneling rate per unit volume γ as a function of $1/\bar{\varepsilon}$ obtained from THA corresponding to the largest available cutoff $n_{\max} = 18$, for $l = 20$ and various values of the coupling $\bar{g}$. The dashed lines denote the theoretical predictions (7.10). The vertical lines correspond to $\bar{\varepsilon}$ values where the resonant bubble size is exactly half the system size $a_* = l/2$, and demonstrate that the difference between the numerical and theoretical results for small values of $\bar{\varepsilon}$ originates from finite size effects. The error bars are obtained from fitting errors (a representative sample of which is shown in Fig. 7.6) and represent a crude estimate.

Ising model, requiring a similar redefinition of the corresponding theoretical prediction [185] to match the numerical data.

As seen in Fig. 7.7, the matching between the THA and the theoretical predictions persists for a range of values of the interaction strength $\bar{g}$, which further supports the validity of the THA. For the cases studied, there is a range of $\bar{\varepsilon}$ where the THA can reproduce the theoretical dependence (apart from the additional factor $C(\bar{g})$), while deviations from the theoretical curve occur at each end of the studied interval of $\bar{\varepsilon}$. For small values of $\bar{\varepsilon}$ (large values of $1/\bar{\varepsilon}$), the difference between the results stems from finite size effects due to the large size of the critical bubble (7.6), comparable to the system size L. To illustrate this, in Fig. 7.7 we display values of $1/\bar{\varepsilon}$ for which the resonant bubble size a_* is equal to half the volume $L/2$ by colour-coded vertical lines. Indeed, the placement of these coincides with the narrow region where the THA deviates from (7.21).

For larger values of $\bar{\varepsilon}$ (small values of $1/\bar{\varepsilon}$), the disagreement between the numerical data and the theory can originate from two different sources. Firstly, formula (7.10) and subsequently the redefined formula (7.21) is valid only in the thin-wall limit [184], corresponding to relatively small values of the external field, although providing an estimation for the limit where the prediction is no longer valid is hard. Secondly, large values of $\bar{\varepsilon}$ result in strong symmetry-breaking and, therefore, a high energy injected into the system during the quench, which, if comparable to the UV cutoff Λ, can lead to truncation errors, ultimately spoiling the accuracy of the THA. Additionally, really large values of the symmetry-breaking field can renormalise the potential appearing in the Hamiltonian (7.12) to a point where the local
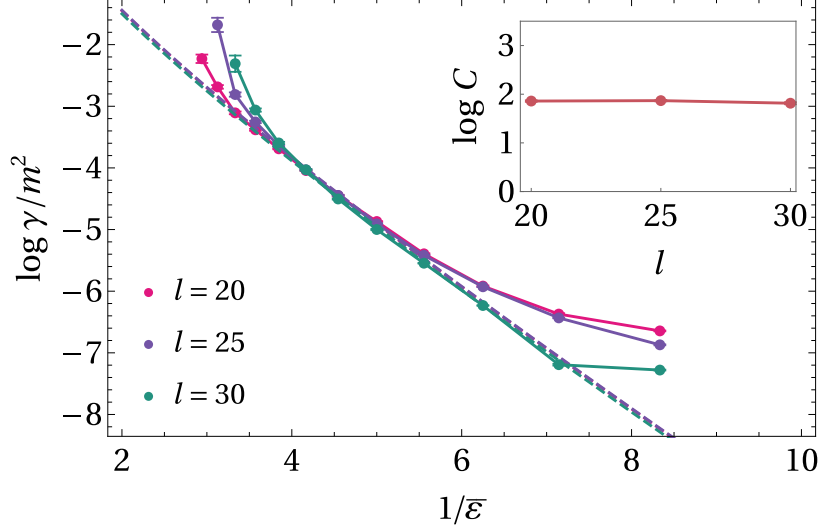
Figure 7.8: The logarithm of the nucleation rate per unit volume γ computed for different volumes l at interaction $\bar{g} = 1.1$ from the THA. The theoretical predictions (7.21) are denoted by dashed lines. In the inset the volume dependence of the fitting parameters $\log C$ is shown. The (barely visible) error bars represent the uncertainty of the fitting errors of the parameter estimation.

minima, corresponding to the false vacuum, disappears entirely, which massively changes the dynamics of the system.

Finally, we discuss the properties of the factor $C(\bar{g})$, starting by testing whether it depends on the volume. We perform simulations in additional system sizes $L = 25$ and 30. Convergence of the results required a mini-superspace dimension of 41 and a non-zero cutoff $n_{\max} = 18$, 22 and 24 corresponding to total Hilbert space dimensions of cc. 280000, 680000 and 680000 for $l = 20$, 25 and 30, respectively. The results, presented in Fig. 7.8, show no dependence of $C(\bar{g})$ on the volume. Additionally, our findings are consistent with the expectation that simulations in larger system sizes, where the simulation is mostly limited by finite size effects, extend the validity of the numerical data to larger values of $1/\bar{\varepsilon}$. Also, for small values of $1/\bar{\varepsilon}$, the disagreement grows with the volume. This suggests that instead of the validity of the thin-wall approximation, the deviations stem from truncation effects: the UV cutoff (4.67)

$$\Lambda = \frac{4\pi n_{\max}}{l} \tag{7.22}$$

is proportional to $1/l$ in units of m, decreasing with the increase of the system size. Finally, Fig 7.9 shows $C(\bar{g})$ for different values of the coupling $\bar{g}$, obtained in volume $l = 20$. The simulated results show that the prefactor appearing in the nucleation rate (7.21) depends on $\bar{g}$ non-perturbatively, hinting at the incompleteness of the original formula (7.10). Nevertheless, the appearance of the normalisation factor $C(\bar{g})$ is unclear to us at this point, warranting further investigation.
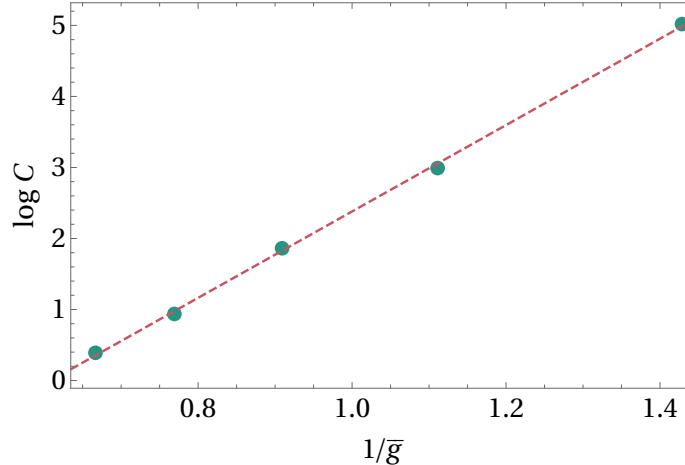
Figure 7.9: The logarithm of the normalisation factor C as a function of the inverse coupling $1/\bar{g}$ together with the appropriate linear fit. The data is computed using the THA in a volume $l = 20$ with a cutoff value of $n_{\mathrm{max}} = 18$.

7.4 Summary

The $\mathbb{Z}_2$-broken phase of the φ^4 theory is characterised by two degenerate minima of the classical potential, corresponding to two vacua in the quantum model with equal energy densities. An interesting setup is provided by including an explicitly symmetry-breaking term in the Hamiltonian, analogous to an external field ε coupled to the canonical field $\hat{\varphi}$, which lifts the degeneracy between the ground states. As a result, the theory admits a single ground state (the *true vacuum*) corresponding to the global minimum of the potential, while the other local minimum becomes a metastable state called the *false vacuum*. A system stuck in the false vacuum becomes unstable, eventually decaying through quantum mechanical tunnelling. First described by Coleman [175], this decay happens through nucleation of bubbles of true vacuum throughout the volume, that subsequently expands driven by the excess energy coming from the energy difference of the true and false vacua and converting the false into true vacuum throughout the medium. Consequently, the excess energy (also called latent heat) produced by the nucleation and expansion of the bubbles eventually gives rise to an abundance of particle excitations above the true ground state.

We focused on the decay of the false vacuum in the φ^4 theory, one of the simplest relativistic quantum field theories, to provide such a setup as a one-dimensional analogue of the Higgs particle in the Standard Model. We investigate the decay by setting up a particular quantum quench, where the system is initially prepared near the false vacuum. To study the time evolution of the order parameter $F(t)$ and to extract the decay rate, we apply a version of the truncated Hamiltonian approach (THA) constructed upon the massive free boson Fock space, together with a mini-superspace expansion, which encodes information about the symmetry breaking already in the basis.

Analytical expressions for the bubble nucleation rate per unit volume were first provided by Coleman [175] by considering a semi-classical approximation of quantum fluctuations on the instanton background. Later, a prediction containing all 1-loop corrections valid in generic one-dimensional systems was proposed by Voloshin [184], expected to hold in the

thin-wall limit, which serves as the basis of comparison for our numerical results. Identifying the exponential behaviour of $F(t)$, we find that THA results for the dependence of the nucleation rate on the latent heat agree well with the theoretical predictions by including an overall normalisation factor (fitting parameter) $C(\bar{g})$ for various values of the coupling $\bar{g}$. The appearance of such a factor is consistent with results obtained in a similar setup to study the false vacuum decay in spin chains [189]. In Voloshin's formula (7.10), the dependence on the latent heat $\mathcal{E}$ comes from the exponential of the instanton action and a prefactor proportional to $\mathcal{E}$ resulting from quantum fluctuations. Ultimately, we inspected the logarithm of the decay rate $\log\gamma$, whose dependence on $\mathcal{E}$ is dominated by the instanton action as $1/\mathcal{E}$, and this exact dependence (together with the factor within the exponential) is accurately reproduced by the THA. The prefactor, corresponding to the fluctuations, contributes a $\log\mathcal{E}$ dependence to $\log\gamma$. Although consistent with our results, the slowly changing nature of the logarithm restricts us to more accurately verify its presence. However, our results suggest that $C(\bar{g})$ is independent of the latent heat $\mathcal{E}$ and the volume L and depends solely on the coupling $\bar{g}$ in a highly non-perturbative way. The detailed origin of the prefactor is unknown to us at present, warranting thorough investigation.

Finally, as already mentioned, the decay of the false vacuum has been studied recently in a similar setup in quantum spin chains using tensor network methods [189]. Easily formulated directly in infinite volume, tensor network methods show a great advantage over the THA simulations. However, they are still limited in time due to the build-up of entanglement in the system. Additionally, time evolution in lattice models, such as the spin chains studied, can exhibit lattice-related effects, such as Bloch oscillations [192], that can prevent the expansion of the bubbles and therefore, the total conversion to the true vacuum throughout the system [193], as found recently. In contrast, the THA is formulated in terms of a field theory, resulting in the absence of such lattice effects, which provides a great advantage.

Chapter 8

Non-equilibrium dynamics in the sine-Gordon model

The (1+1)d φ^4 theory is an interacting relativistic quantum field theory with great significance in statistical mechanics and high-energy physics. Despite its importance, the model admits no condensed matter realisation that allows its study in a laboratory setting. Instead, now we turn our focus to the non-equilibrium dynamics of the sine-Gordon model, a paradigmatic example of an integrable relativistic quantum field theory that provides a low-energy effective description of many gapped one-dimensional systems through bosonisation (see App. B for a detailed example) [90–96, 98, 99]. Recent advances in ultracold-atomic experiments provided a realisation of the model [100] with two Josephson-coupled bosonic quasi-condensates [2, 4, 8, 101, 102], leading to a considerable rise in the interest for out-of-equilibrium dynamics of the sine-Gordon model.

Motivated by the success of the THA for the φ^4 model, we study the out-of-equilibrium dynamics of two coupled bosonic quasi-condensates described by the sine-Gordon model by performing quantum quench simulations using the truncated Hamiltonian space approach built upon the massless free boson eigenstates. To achieve better accuracy, we implement a mini-superspace treatment of the zero mode of the theory, describing a quantum pendulum. The mini-superspace-based truncated Hamiltonian approach (MSTHA), discussed in Section 4.3.2, also serves as a basis of comparison for the semi-classical truncated Wigner approximation (see Section 4.2), previously used to approximate the time evolution of the model [115, 173]. To understand the limitations and the validity of both approaches, we perform two types of quenches, characterised by their small (mild quench) and large (strong quench) injected energy densities. We do this for a large range of interaction parameters, from the strongly interacting quantum regime to the experimentally available semi-classical limit, where inter-mode interactions are expected to be less relevant.

8.1 Simulating the dynamics

A quantum quench in the sine-Gordon model is the unitary time evolution of some initial state $|\Psi_0\rangle$

$$|\Psi(t)\rangle = e^{-i\hat{H}_{\mathrm{sG}}t} |\Psi_0\rangle \tag{8.1}$$

governed by the sine-Gordon Hamiltonian

$$\hat{H}_{\mathrm{sG}} = \int_0^L dx : \left(\frac{1}{2}(\partial_t \hat{\varphi})^2 + \frac{1}{2}(\partial_x \hat{\varphi})^2 - \lambda \cos \beta \hat{\varphi} \right) : . \tag{8.2}$$

In the following simulations, we investigate the time evolution of the cosine of the phase field

$$\langle : \cos \beta \hat{\varphi} : \rangle , \tag{8.3}$$

characterising the strength of phase coherence between the coupled quasi-condensates, also accessible in experiments. Here, the expectation value $\langle . \rangle$ is taken in the time evolved state (8.1). We also study the time evolution of the Fourier transform of the phase-phase correlator

$$\langle \hat{\varphi}_k \hat{\varphi}_{-k} \rangle = \frac{1}{4\pi k^2} \langle a_{-k} a_k + \bar{a}_{-k} \bar{a}_k - a_k \bar{a}_k - a_{-k} \bar{a}_{-k} + k \rangle , \tag{8.4}$$

an experimentally available observable, corresponding to the mode-resolved occupation numbers, that allows for the identification of the momentum modes with relevant contributions to the dynamics.

In our subsequent calculations, we parametrise the strength of interactions (corresponding to the coupling β) via the Luttinger parameter K:

$$K = \frac{\pi}{\beta^2} , \tag{8.5}$$

with $K = 1$ corresponding to hard-core repulsions between the bosons forming the condensates. Increasing K decreases the sine-Gordon interaction strength, with large K corresponding to the semi-classical limit of the theory. We employ units in which $m_1 = 1$ and therefore define the dimensionless volume parameter as $l = Lm_1$. Time is characterised by the dimensionless parameter $t\nu_1$, associated to the frequency of the lightest breather $\nu_1 = m_1/2\pi$. To establish a connection with the experimental realisation of the sine-Gordon model using two Josephson-coupled one-dimensional bosonic quasi-condensates, the strength of the sine-Gordon interaction is characterised by the aforementioned Luttinger parameter K. In the following, we present simulations for various interaction strengths, from $K = 1$ to the more experimentally relevant semi-classical limit when K is large.

We simulate the dynamics in a volume of $l = 10$, which limits the observable dynamics to times $t\nu_1 < 10$. Even though simulation on longer time scales is theoretically possible, the dynamics for $t\nu_1 > 10$ differs from the infinite volume results due to finite size effects caused by excitations travelling around the circle. Also, lower volumes are less computationally demanding, and we found that the time scales provided by the choice of $l = 10$ did not impair the comparison of the two methods. As a cross-check, we performed simulations in larger volumes up to $l = 18$, the results of which did not alter the conclusions presented below.

We consider two types of quantum quenches, characterised by their injected energy density during the quench. First, in Section 8.1.1, we focus on weak quenches, generating a small energy density which subsequently limits the number of quasi-particle excitations. This generally means that quantum fluctuations contributing to the time evolution decohere to a

lesser extent (and on longer time scales), dominating the dynamics. As a result, this setup favours the MSTHA, and it is considered less optimal for the TWA. To achieve this setup, we initialise the system close to the ground state of the quantum pendulum in a way that it is naturally represented in the MSTHA basis, in contrast to previous implementations of the TCSA [115]. Indeed, we find that the MSTHA delivers accurate, well-converged results for the time evolution for a wide range of the interaction strength K considered here. Though not directly relevant to experiments, these findings substantially extend the quench setups available to Hamiltonian truncation and allow for the study of strongly coherent quantum phenomena in the out-of-equilibrium dynamics of the sine-Gordon model.

The out-of-equilibrium dynamics of the sine-Gordon model were previously studied in a work by Horvath et al. [115], where, along with the TWA, the authors employed the TCSA built upon the free massless boson eigenstates and studied the time evolution following quantum quenches initiated in the ground state of the compactified free massless boson. The protocol is the field theoretical equivalent to the switching on of the Josephson coupling (finite λ) between two initially decoupled one-dimensional bosonic quasi-condensates. Despite their choice of basis for the TCSA, which strongly caters to the initial state, the TCSA was found to be limited to the strongly interacting regime, where K is small. Here we revisit this quench setup and simulate the time evolution via the TWA and the MSTHA. In the case of the MSTHA, we find similar limitations, yielding well-converged results for small values of the Luttinger parameter but breaking down in the experimentally available parameter range. On the other hand, the large energy density induced by the quench favours the TWA, extending its validity to stronger interactions, with reliable results also in the weakly interacting regime accessible to experiments.

8.1.1 Quenches starting from the quantum pendulum ground state

Here, we present our results for the time evolution of the Fourier modes of the phase-phase correlator and the cosine of the phase field starting from the quantum pendulum ground state, corresponding to a mild quench with small injected energy density. The initial state is constructed such that the zero mode is in its ground state

$$|\Psi_{\mathrm{QP}}\rangle = |n = 0\rangle, \tag{8.6}$$

and the non-zero modes are prepared in the ground states of their respective massless oscillator. This scenario is optimal for the MSTHA, as the initial state can be naturally represented on the MSTHA basis. Also, the energy density induced by the quench is small, which further improves the effectiveness of the Hamiltonian truncation. The time evolution is governed by the sine-Gordon Hamiltonian (4.69) and can be interpreted as the sudden switching on of the coupling between the quantum pendulum and a bath of massless phononic degrees of freedom (the non-zero modes). Though this scenario is not directly relevant to experiments, a more experimentally realistic protocol can be provided by considering the phononic modes initiated in the ground state of the appropriate massive oscillators. The inclusion of massless oscillator modes employed here eventually overestimates their contributions but allows for some technical simplifications, motivating our choice. First, the gapless degrees of freedom are more simply represented in the MSTHA. Secondly, one of the most relevant experimental

setups is quenching from the free massless boson vacuum, which prohibits using a massive basis due to the presence of infrared divergences. Additionally, to gauge the relevance of the contribution of the oscillator modes to the quantum pendulum dynamics, the massless nature of the oscillators is secondary, and it is acceptable to consider a slightly unrealistic protocol where the contribution of the non-zero modes is overestimated.

To simulate the dynamics using the TWA, we construct the Wigner function corresponding to the initial state, which can be written up as a product of the zero and non-zero mode parts. The zero mode part can be simply calculated by numerically solving the quantum pendulum Hamiltonian (4.88)

$$\hat{H}_{\mathrm{QP}} = \frac{1}{2L}\hat{\pi}_0^2 - \lambda L \left(\frac{2\pi}{L}\right)^{2h} \cos(\beta\hat{\varphi}_0)\,. \tag{8.7}$$

for the wavefunction of the quantum pendulum ground state and reads

$$W_0\left(\varphi_0, \pi_0\right) = \frac{1}{2\pi} \int_{-\pi}^{\pi} d\varphi_0' \left\langle \varphi_0 - \varphi_0'/2 | n = 0 \right\rangle \left\langle n = 0 | \varphi_0 + \varphi_0'/2 \right\rangle e^{-iN\varphi_0'\pi_0}\,, \tag{8.8}$$

where the matrix element $\langle\varphi|n = 0\rangle$ is the coordinate space representation of the quantum pendulum ground state wavefunction. The contribution of the non-zero modes to the Wigner function is given by [115]

$$W_{\mathrm{osc}} = \prod_{k>0} \frac{4}{\pi^2} \exp\left\{-\sigma_k^2\varphi_k\varphi_{-k} - \frac{4\pi_k\pi_{-k}}{\sigma_k^2}\right\} \tag{8.9}$$

with

$$\sigma_k^2 = 4N \sin\frac{\pi k}{N} \to 4\pi k \quad \text{for } N \to \infty\,. \tag{8.10}$$

The MSTHA and TWA results for the time evolution of the phase-phase correlator and the cosine of the phase field can be seen in Fig. 8.1, starting from the initial state (8.6) for a dimensionless volume $l = 10$ and a wide range of the Luttinger parameter K. For the MSTHA we employed truncation values of $n_{\max} = 9, 7, 11$ and 7 and $\ell_{\max} = 20, 20, 20$ and 24, corresponding to Hilbert space dimensions of 32247, 25081, 39413 and 88536 for $K = 1, 1.56, 4$ and 27, respectively. Here K ranges from $K = 1$, corresponding to hard-core repulsion between the particles in the condensates, up to the experimentally relevant value of $K = 27$.

The MSTHA data presented in Fig. 8.1 is well-converged with respect to the truncation and can be considered essentially exact across all values of the Luttinger parameter. Due to the initial state (8.6), the method requires very few quantum pendulum basis states to converge even for the experimentally relevant $K = 27$, which is generally unobtainable for the usual formulation of the TCSA. On the other hand, the TWA provides reliable results when in the weakly interacting regime (large K), including $K = 27$, but breaks down when the coupling becomes large enough, as indicated by the deviations from the numerically exact MSTHA results. This is in agreement with the expectation that (given the semi-classical nature of the TWA) for strong interactions, the dynamics are dominated by quantum effects, which are generally inaccessible to semi-classical methods. Additionally, the choice of the
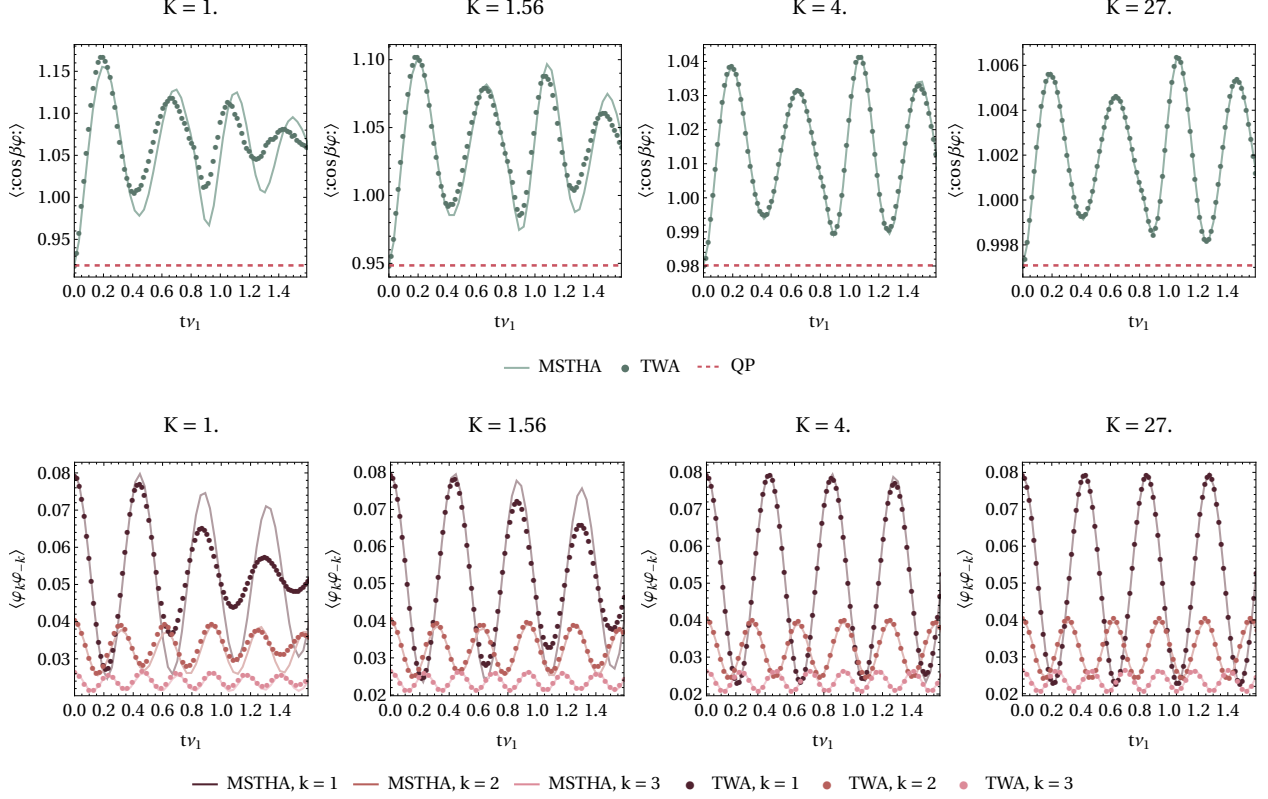
Figure 8.1: Time evolution of the expectation value of $: \cos \beta \hat{\varphi} :$ (top row) and the phase-phase correlator $\langle \hat{\varphi}_k \hat{\varphi}_{-k} \rangle$ (bottom row) for a wide range of the Luttinger parameter K and $l = 10$. During the quench, the system is initiated in the quantum pendulum ground state (8.6). The MSTHA is shown in solid lines, while the joined markers denote the TWA results. The difference between the two methods becomes invisible for the two largest values of K. The dashed red line denotes the (numerically) exact solution of the zero-mode (quantum pendulum) dynamics.

initial state (8.6) results in a small injected energy density that is insufficient to produce high excitation numbers in the non-zero modes, which also contributes to the strong quantum effects. As a result, for small K, the TWA substantially overestimates the dephasing of the condensates, as shown in Fig. 8.1.

Single-mode approximation of the Hamiltonian results in the Hamiltonian (8.7), leading to trivial time evolution, given the initial state (8.6) is its eigenstate. In this case, the importance of the oscillator modes on the quantum pendulum dynamics can be inferred from the amplitudes of the oscillations of the cosine expectation value, which decreases rapidly with growing K, becoming very small for the experimentally relevant $K = 27$, as can be seen in Fig. 8.1. This indicates that the zero mode is very weakly coupled to the oscillator modes in the semi-classical parameter range.

8.1.2 Quenches starting from the free massless boson ground state

Now we consider quenches starting from the vacuum of the $\lambda = 0$ free massless boson

$$|\Psi_{\mathrm{FB}}\rangle = |\nu = 0\rangle . \tag{8.11}$$

The setup is equivalent to quenching two initially decoupled bosonic quasi-condensates to some finite value of λ, which gives rise to non-equilibrium time evolution in the coupled system. This scenario was studied in detail in the previous work [115] using TWA and the original version of the TCSA introduced in Sec. 4.3.2. In this formulation of the TCSA, the initial state (8.11) can be naturally represented on the truncated basis, but this also comes with the drawback that the applicability of the TCSA was limited to small values of K far from the experimentally relevant regime.

In the MSTHA, the initial state (8.11) can be represented by expanding the plane wave state $|\nu = 0\rangle$ in the quantum pendulum eigenbasis (for details c.f. App. A) as

$$|\Psi_{\mathrm{FB}}\rangle = |\nu = 0\rangle = \sum_{n=-N}^{N} C_n |n\rangle \tag{8.12}$$

However, for large values of K, the state (8.11) corresponds to a highly excited state in the quantum pendulum eigenbasis, requiring a large number of zero mode eigenstates for accurate representation. This is a similar problem that arises in the TCSA; nevertheless, we found that the mini-superspace treatment of the zero mode still extended the validity of the MSTHA to higher values of K than previously available.

Turning to the TWA, the Wigner function corresponding to the ground state of the free massless boson can be simply calculated [115] and factorises into zero and non-zero mode parts. The contribution of the zero mode is given by

$$W_0\{\varphi_0, \pi_0\} = \frac{\theta(\varphi_0 + \pi)\theta(\pi - \varphi_0)}{2\pi}\delta_{\pi_0,0} , \tag{8.13}$$

corresponding to a uniform distribution of the initial phase φ_0 over the range $[-\pi, \pi]$ with definite initial canonical momentum $\pi_0 = 0$. The part related to the oscillator modes is the same as before, given in (8.9).

In Fig. 8.2, the time evolution of the cosine of the phase field and the phase-phase correlator can be seen, starting from the initial state (8.11) in a volume $l = 10$ and for multiple values of the interaction strength K. For the MSTHA calculations, we opted for zero mode cutoff parameters $n_{\max} = 11, 17, 35$ and 225 for $K = 1, 1.56, 4$ and 27, respectively. These values were chosen in a way that the dynamics remained unchanged with respect to increasing $n_{\max}$, and clearly illustrate the fact that for large K, the initial state spans a wide range of quantum pendulum states. Again, as before, the largest value of K ($K = 27$) corresponds to the experimentally relevant interaction strength. The oscillator modes were truncated using values $\ell_{\max} = 26, 20, 28$ and 20, corresponding to a total Hilbert space dimension of $251339, 60911, 2521750$ and 806175 for $K = 1, 1.56, 4$ and 27, respectively.

The MSTHA results converge well for $K = 1$ and 1.56, providing essentially exact quantum evolution. For $K = 4$, the results do not strictly converge for the cutoff values studied here but are very close to the exact results. However, for larger values of the Luttinger
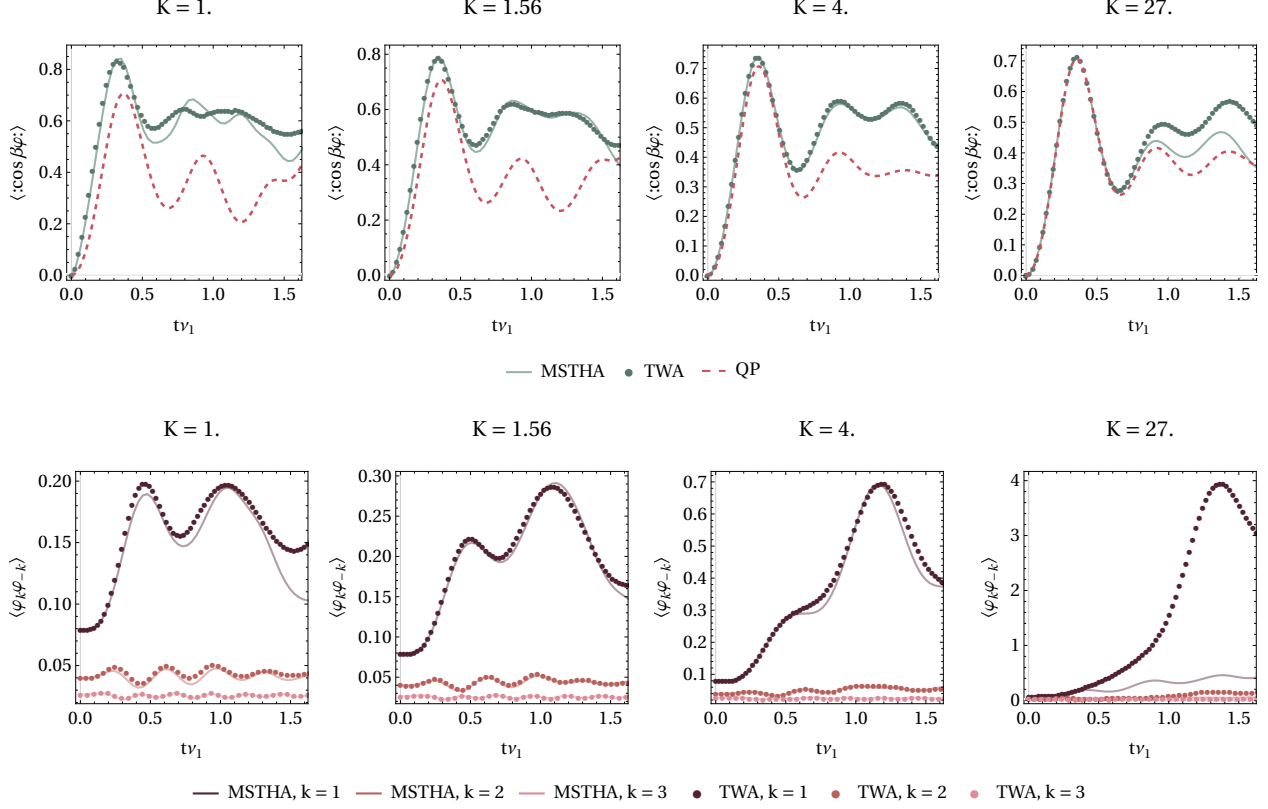
Figure 8.2: Time evolution of the expectation value of $: \cos \beta \hat{\varphi} :$ (top row) and the phase-phase correlator $\langle \hat{\varphi}_k \hat{\varphi}_{-k} \rangle$ (bottom row) for a wide range of the Luttinger parameter K and $l = 10$. During the quench, the system is initiated in the quantum pendulum ground state (8.11). The MSTHA is shown in solid lines, while the joined markers denote the TWA results. The difference between the two methods becomes invisible for the two largest values of K. The dashed red line denotes the (numerically) exact solution of the zero-mode (quantum pendulum) dynamics.

parameter, the MSTHA results showcase much slower convergence, requiring the inclusion of higher excitations in the oscillator modes, which makes the method very computationally expensive. This limits its validity to parameters outside of the experimental range, where the method requires smaller truncation values to converge.

Similarly to before, the TWA struggles to capture the correct dynamics for $K = 1$, when the quantum effects are strong, signalled by the deviations from the numerically exact MSTHA results. However, the accuracy of the TWA is improved for $K = 1.56$, matching with the MSTHA. This improvement originates from the initial state (8.11), as during the quench a large energy density is injected into the system, giving rise to large excitation numbers in the oscillator modes, subsequently decohering the dynamics of the quantum pendulum, as can be seen in Fig. 8.2. This behaviour persists for smaller interaction strengths $K \geq 2$, all the way to the experimental parameter range, where the TWA can be considered very accurate. This is contrasted by the behaviour found in the case where the initial state is the quantum pendulum ground state 8.6, where the small induced energy density forbids the accumulation of large occupation numbers (presented in Fig 8.1) that could decohere the

zero mode dynamics. When the system is initialised in the free boson vacuum (8.11), the large energy of the initial state with respect to the post-quench ground state is transferred to the oscillator modes during the quench. These occupations grow with K, as seen in Fig. 8.2, resulting in the matching of the two methods for $K = 1.56$ and 4, and the accuracy of the TWA for the experimental parameter $K = 27$.

Again, the red dashed lines in Fig. 8.2 show the single-mode dynamics governed by the zero mode Hamiltonian (8.7). For large values of K, the zero mode dynamics is close to the MSTHA and TWA simulations, suggesting that the zero mode dominates the dynamics of the sine-Gordon model. However, the presence of the oscillator modes contributes substantially to the dynamics even for the experimentally relevant weakly interacting regime, consistent with the observation that the large energy transfer to the non-zero modes counteracts their weak coupling to the quantum pendulum, resulting in large occupation numbers in the respective modes influencing the dynamics.

8.2 Summary

To study the low-energy out-of-equilibrium dynamics of two tunnel-coupled one-dimensional bosonic quasi-condensates, we performed quantum quenches in the sine-Gordon model. The parameter range accessible to experiments corresponds to a very weak (sine-Gordon) interaction strength between the modes, motivating the use of semi-classical methods to study the dynamics. Therefore, we apply the semi-classical truncated Wigner approximation (TWA) that has been previously applied to study the dynamics of the model [115, 173]. However, the accuracy of the TWA is hard to control and needs to be carefully validated against other, better-controlled methods.

To this end, we also implement a version of the truncated Hamiltonian approach (THA). Though previous versions of the method, called the truncated conformal space approach (TCSA) have been recently used to study the dynamics [132] and also to validate the TWA [115], their use was limited to the strongly interacting regime characterised by small values of the Luttinger parameter K. Due to the weak coupling between the zero and non-zero modes in the experimentally available regime corresponding to large K, it is natural to ask whether the non-zero modes substantially affect the dynamics of the zero mode. Therefore, we develop an improved version of the TCSA by including a mini-superspace treatment of the zero mode by separating it from the non-zero modes and pre-diagonalising it numerically exactly. The sine-Gordon model can be considered to describe a quantum pendulum (the zero mode) coupled to a bath of non-linearly interacting phononic degrees of freedom (non-zero modes). The resulting mini-superspace-based THA (MSTHA) is advantageous in many regards: it makes the distinction between the zero and non-zero modes apparent, improves on the previous TCSA by extending its validity to larger values of K, and naturally allows for simulating quench protocols that have been previously unavailable to the original TCSA.

To better understand the role of non-zero modes and the applicability of both the TWA and MSTHA, we considered quantum quenches starting from two types of initial states, corresponding to small and large injected energy densities. For the mild quench, starting from the ground state of the quantum pendulum, the MSTHA performed excellently, giving well-converged results for all values of K studied, from very strong interactions $K = 1$ to the

experimentally available $K = 27$, a regime inaccessible by previous implementations of the TCSA [115]. In the case of the stronger quench, the system is initiated in the free massless boson vacuum. Here, we find that the MSTHA performs similarly well for strong interactions $K \lesssim 4$, yielding essentially (numerically) exact results. However, for large K close to the experimentally relevant parameters, the method fails to converge for the truncation values studied here due to the computationally tasking representation of the initial state and the large occupation numbers of the non-zero modes required to reproduce the exact quantum dynamics.

According to expectations, we find that the TWA performs very well for weak interactions, even when the energy density injected by the quench is small, signalled by its close match with the MSTHA results. However, deviations between the methods start to grow with decreasing K, and the TWA breaks down close to the limit of hard-core repulsion between the bosons forming the condensates, $K \approx 1$. This behaviour also carries over to stronger quenches, starting from the free massless boson ground state; nevertheless, the TWA shows strong improvements due to the larger energy density, allowing for the build-up of larger occupation numbers in the phononic modes. As a result, the validity of the TWA is extended to up to $K \geq 1.56$ and is considered very accurate in the large K limit directly relevant to experiments.

We find that the contribution of the non-zero modes to the quantum pendulum dynamics is minor whenever the inter-mode interaction is weak, particularly for mild quenches. However, in the case of strong quenches, even in the experimentally available weakly interacting regime, the eventual build-up of excitations in the phononic degrees of freedom affects the dynamics substantially, rendering the single-mode dynamics impractical when describing the dynamics of the condensates.

Overall, our findings establish the TWA and MSTHA as powerful complementary methods to study the dynamics of the sine-Gordon model. Ultimately, the choice should depend on the quench protocols studied and the strength of interactions: the MSTHA performs excellently in the case of mild quenches or strong quenches and strong interactions, while the TWA is a great choice for quenches when the energy density injected into the system is large, or the interactions are weak, even in the case of mild quenches.

Chapter 9

Conclusions

The dynamics of isolated quantum many-body systems has attracted prominent attention in contemporary theoretical physics. Recent advances in cold-atomic experiments [2–8] opened the possibility of probing the non-equilibrium dynamics of many strongly correlated condensed matter systems, leading to a rise in interest in corresponding theoretical investigations.

One of the cornerstones of one-dimensional quantum many-body research is integrable models characterised by an infinite set of local conserved charges and factorised scattering of quasi-particles. On the one hand, as discussed in Chapter 2, time evolution is strongly affected by integrability, and the details of their equilibration are generally an open question. On the other hand, integrability allows for powerful analytical approaches to study the spectrum and the dynamics in these systems, in many cases leading to exact results.

Quantum spin chains provide a prevalent platform for studying integrability and its breakdown in quantum many-body systems. Apart from analytic and numerical investigations, today, their dynamics can be realised and studied experimentally in a laboratory setting [71–75]. In the context of integrable spin chains, one of the main focus is on the construction and categorisation of the local conserved charges and corresponding generalised currents that contribute to the integrable nature of these systems. Recently, the problem gained renewed interest due to the so-called generalised hydrodynamics (GHD) that describes the non-equilibrium dynamics of integrable systems at the Euler scale [138, 139] with many new exact results for the expectation values of generalised currents [76, 137].

Recently, it was discovered in [137] that the existence of exact formulae for the expectation values of generalised currents is strongly connected to the long-range deformations of integrable spin chains known in the Ads/CFT correspondence. As a result, the authors showed that perturbing an integrable spin chain by one of its currents preserves integrability at first order in perturbation theory in the integrability breaking parameter g. Similar behaviour has been observed in $T\bar{T}$-deformations of integrable quantum field theories [148–151] with strong connections to the long-range deformations. This new class of integrability breaking has been dubbed *weak* in contrast with the usual *strong* integrability breaking that occurs already at first order in perturbation theory. The distinction between the two types of integrability breaking is a novel one: in a recent work [153], the authors argue that weak integrability breaking corresponds to moving along the tangent space of the manifold of integrable models embedded in the full space of quantum many-body systems, and as a result, the onset

of chaos is much slower compared to the usual strong integrability breaking, equivalent to 'radially' moving away from the integrable system.

To investigate the weak integrability breaking of quantum spin chains, we compared the current and next-to-nearest-neighbour (NNNI) perturbations of the spin-1/2 XXZ spin chain. While the latter is a well-known example of a strongly integrability-breaking perturbation, the generalised current perturbation is expected to break integrability at higher orders in perturbation theory. The breakdown of integrability can be probed via some indicator of (non-)integrability, such as the distribution of normalised consecutive level spacings. While for a finite system, the level spacing statistics can continuously vary between the Poissonian and Wigner-Dyson distributions (characterising integrable and non-integrable behaviour, respectively), in the limit of infinite system size any finite value of the integrability-breaking parameter g results in the sudden change from the Poissonian to the Wigner-Dyson statistics. Therefore, the deciding factor between weak and strong integrability breaking is the scaling of the rate of crossover with the system size [166, 169, 170].

Through numerical exact diagonalisation, we demonstrated that the current perturbation scales more slowly in the volume L than the NNNI perturbation, signalling weak integrability breaking in both the gapless and gapped phases. In particular, in the gapless phase, the scaling is expected to be described by a power-law L^{-b}. In the NNNI case, our value for $b_{\text{NNNI}} \approx 3$ agrees with previous results found in the literature [170]. The value 3 is eventually claimed to be universal in gapless spin chains with strongly broken integrability, albeit without analytical evidence. For the current perturbation J, we obtain the value $b_J \approx 2$ for the exponent. Though the order at which integrability is broken cannot be deduced from these results, the marked difference between the exponents is clear and supports the idea that perturbing an integrable spin chain via one of its generalised currents preserves integrability at first order.

The universality of these exponents is still an open question. In a recent work [166], the authors investigated the weak integrability breaking in a field theoretic setting and observed that the difference between the exponents corresponding to strong and weak breaking is similarly close to 1, albeit their values are different and therefore cannot be declared universal. The work [194] describes the breakdown of integrability and the onset of many-body quantum chaos as a Fock-space delocalisation process that depends continuously on the system size with some appropriate scaling exponents.

Close to the critical point, the dynamics of the relevant (large-scale) degrees of freedom of lattice models are described by an appropriate quantum field theory (QFT) [1]. As discussed in Chapter 4, the dynamics of interacting QFTs can not be solved exactly and calls for approximations and numerical methods. Therefore, understanding the validity of different approaches is crucial in understanding the dynamics of these many-body systems.

A textbook example of interacting non-integrable relativistic QFTs is the $(1+1)$-dimensional φ^4 model. It describes the scaling limit of the Ising model and serves as an ideal platform to study the validity of semi-classical approximations for the non-equilibrium dynamics of non-integrable field theories. Two such widely used approaches are the self-consistent Hartree-Fock (SCA or mean field) approximation [104–111] and the truncated Wigner approach (TWA) [112–115] introduced in Chapter 4. The SCA for the φ^4 model was developed by Cardy and Sotiriadis in [111]. It approximates the time evolution by omitting the connected part of the interaction, reducing the dynamics to a free boson with

a self-consistently obtained time-dependent mass. In the TWA, the dynamics is computed by Monte Carlo averaging an ensemble of classical trajectories distributed accordingly to a Wigner quasi-probability distribution describing the quantum fluctuations in the initial state.

To determine their range of validity, we simulated the time evolution of expectation values of local observables following quantum quenches [19, 20], a paradigmatic, experimentally viable protocol to investigate the out-of-equilibrium time evolution (for more details c.f. Chapter 2). As a general rule, the accuracy of semi-classical approximations is hard to control, and as a benchmark, we also simulate the time evolution via the truncated Hamiltonian approach (THA) built upon the free massive boson basis, which has been previously applied successfully to study the properties of the theory [81–83, 89]. The THA is a non-perturbative approach for studying the spectral properties and time evolution of relevant perturbations of (solvable) quantum field theories originally developed by Zamolodchikov and Yurov [116].

The validity of semi-classical approaches was tested by simulating the non-equilibrium time evolution of the Fourier transform of the correlator following general quenches in the $\mathbb{Z}_2$-symmetric phase of the φ^4 theory consisting of changing the mass m and the quartic coupling λ. For the wide range of interaction strengths studied, the THA proved very successful in computing the time evolution and showed negligible cutoff dependence, practically yielding exact results and serving as a reliable benchmark for the semi-classical simulations.

According to expectations, in the limit of small λ, the SCA agrees with the THA and successfully reproduces the exact time evolution. However, the SCA breaks down when the interactions become stronger, signalled by the large deviations from the THA curve. The TWA exhibited similar behaviour and produced accurate results in the case of small interactions. For larger values of λ however, the TWA results show quick relaxation to a symmetry-broken classical steady state in contrast to the THA due to mass renormalisation: the TWA is formulated on the lattice using the bare (non-renormalised) mass of the system. For large values of λ, the bare mass becomes negative, giving rise to a classically spontaneously symmetry-broken potential, causing the relaxation to a steady state and failing to reproduce the exact quantum evolution. Our findings have important consequences for the TWA when applied to other field theories with additive mass renormalisation, such as higher-order Ginzburg-Landau theories. The TWA has also been applied to the sine-Gordon model [115, 174], where this effect is missing due to the multiplicative renormalisation of the mass in the theory.

Apart from its quantum statistical mechanical importance, the (1+1)d φ^4 theory provides a one-dimensional analogue of the Higgs field in the Standard Model. Recently, it has gained additional attention due to the indication of the metastability of the Higgs vacuum [77, 177], which resulted in a newfound interest for the tunnelling in quantum field theories, a.k.a. the decay of the false vacuum. Perturbing the φ^4 model via an odd function of the field $\hat{\varphi}$ in the spontaneous symmetry broken phase gives rise to a metastable state in the spectrum called the false vacuum. A system prepared in the false vacuum will eventually decay through quantum mechanical tunnelling, driven through nucleations of finite regions (bubbles) of the true vacuum (the true ground state of the theory). These bubbles then expand, propelled by the energy difference between the false and true vacua, converting the available space to the true ground state. The false vacuum decay is usually studied in the context of high-energy physics; however, the recent advances in cold-atomic experiments enabled the study

of the phenomena in various condensed matter setups [178–183], also resulting in its recent theoretical study in various systems [177, 186, 187].

The main quantity of interest in this context is the bubble nucleation or tunnelling rate Γ. In his seminal works [175, 176], Coleman proposed a semi-classical formula for Γ, which was later extended to generic one-dimensional systems taking into account all 1-loop corrections by Voloshin [184] and expected to be valid in the thin-wall limit when the size of walls of the bubble is much smaller than its volume. Similar results are available for spin chains [185]. Here, we focus on the (1+1)d φ^4 theory and compute the tunnelling rate per unit volume γ by simulating the false vacuum decay following quantum quenches using the truncated Hamiltonian approach. Therefore, we apply a special treatment of the zero mode called the mini-superspace approach consisting of separating and pre-diagonalising the zero mode to consider the main part of the symmetry breaking. The tunnelling rate γ can be extracted from the time evolution by preparing the system close to the false vacuum and identifying the exponential decay in the time evolution of the order parameter indicated by a linear drop in its logarithm.

We find that the obtained tunnelling rate as a function of the latent heat $\mathcal{E}$ agrees well with Voloshin's formula (7.21) [184] up to fitting an overall normalisation factor. Such redefinition of the normalisation is ultimately expected: Voloshin's formula for the tunnelling rate, expected to be valid for all one-dimensional systems, does not agree with the one proposed for the Ising model by Rutkevich [185]. Additionally, a similar numerical study of the vacuum decay in the Ising and tricritical Ising field theories required the redefinition of the normalisation of the tunnelling rate [188]. The precise origin of the re-normalisation factor is generally an open question with promising directions in recent research in higher dimensions [177, 186, 187]. To sum up, our findings establish the THA as a powerful tool to probe strongly-correlated, non-perturbative phenomena in non-equilibrium dynamics, such as the false vacuum decay, with definite and precise numerical results that can serve as a benchmark for this highly researched open problem.

The one-dimensional φ^4 theory is a paradigmatic model in statistical and high-energy physics that exhibits interesting physical phenomena such as false vacuum decay. Currently, however, there are no condensed matter realisations of the system that would serve as the basis to study its dynamics experimentally. Instead, experiments using two Josephson-coupled one-dimensional bosonic quasi-condensates [2, 4, 8, 101, 102] provided an effective quantum simulator for non-equilibrium dynamics of the sine-Gordon model. The sine-Gordon model is a prevalent example of integrable quantum field theories that describes the dynamics of collective degrees of freedom of many gapped one-dimensional condensed matter systems [90–96, 98, 99] through bosonisation, such as the coupled condensates realised in the experiments [100]. However, the non-equilibrium time evolution observed in the experiments suggests dynamics beyond the sine-Gordon model [195–197], attributed to additional relevant degrees of freedom such as the symmetric modes or the transverse modes originating from the quasi-one-dimensional geometry. Therefore, identifying the relevant degrees of freedom and constructing the simplest theoretical model describing the experimental observations is crucial to understanding the dynamics and is generally an open question. Answering it requires a precise numerical description of the sine-Gordon dynamics in the parameter range available to the experiments.

In the context of experiments, the strength of sine-Gordon interactions is typically char-

acterised by the Luttinger parameter K. In the experimental setup, K is large $K \approx 27$, which corresponds to very weak interactions between the sine-Gordon modes. As a result, a natural viewpoint is to consider the sine-Gordon model as a quantum pendulum (the zero mode) coupled to a bath of non-linearly interacting phononic degrees of freedom (non-zero modes).

Based on the quantum pendulum picture and motivated by the success of THA for the φ^4 model, we study the non-equilibrium dynamics of the sine-Gordon model using a truncated Hamiltonian approach built upon the basis of the massless free boson based on a mini-superspace treatment of the zero mode (MSTHA). The mini-superspace approach has two main advantages: firstly, it helps achieve better accuracy by treating the zero mode of the phase field exactly. Secondly, it allows for the precise control of the modes in the theory by treating the zero mode separately, motivated by the quantum pendulum picture. Previous installations of the THA constructed on the conformal basis (TCSA) have been applied to study the spectral properties and dynamics of the model [115, 124, 131, 132] generally successfully, but failed to reproduce the exact dynamics in the semi-classical regime characteristic to the experiments. The MSTHA also serves as a benchmark for the truncated Wigner approach that has proved to be successful in approximating the dynamics of the condensates [115, 173].

To understand the validity and limitations of both approaches, we perform quantum quenches starting from two distinct initial states corresponding to mild and strong quenches characterised by their injected energy densities, starting from the quantum pendulum and free boson ground states, respectively. While the former has no direct experimental relevance, the latter corresponds to a sudden coupling between the initially independent condensate pair and can be investigated experimentally. For the mild quench starting from the quantum pendulum ground state, the MSTHA shows negligible truncation effects and can be considered practically exact for the wide range of sine-Gordon interaction strengths studied, all the way up to the experimentally relevant values. In contrast, the TWA works well in the semi-classical regime characteristic of the experiments but breaks down whenever the correlations grow strong enough.

In the case of the strong quench, the TWA works similarly well for large values of the Luttinger parameter K (corresponding to weak interactions), and its validity is extended to stronger interactions due to the increased energy density injected into the system. This is eventually expected, as the increase in the energy results in the growing number of excitations that decohere the dynamics, favouring the TWA. However, this scenario is not favourable for the MSTHA when K is too large: the large occupation numbers necessary to reproduce the exact dynamics require very large cutoff values inaccessible to the MSTHA, ultimately rendering it unreliable in the experimentally relevant parameter regime. Nevertheless, these results establish the TWA and the MSTHA as powerful complementary methods for studying the non-equilibrium dynamics of the sine-Gordon model for a wide range of parameters and various quench scenarios. Depending on the injected energy density during the quench, both methods offer accurate ways of computing the non-equilibrium dynamics in the parameter range accessible to experiments.

The success of the TWA for large values of the Luttinger parameter suggests that in the experimental regime, the role of quantum fluctuations is greatly suppressed by the large occupation numbers that decohere the dynamics. Additionally, the role of the non-zero

modes on the dynamics shows a strong dependence on the quench scenario: for small injected energy densities, the phononic degrees of freedom have limited effect on the time evolution of the quantum pendulum when the inter-mode interactions are relatively weak. When the injected energy density during the quench is large, apart from an initial transient, the low-momentum phononic modes strongly affect the dynamics when their occupation number becomes large in the experimentally relevant weakly interacting regime.

Moreover, we find that the sine-Gordon model does not account for the experimentally observed phase-locking [195], suggesting the presence of additional relevant degrees of freedom contributing to the experimental dynamics. One of the main candidates is the symmetric modes of the condensate that, in the presence of inhomogeneities (due to the spatially dependent longitudinal trapping potential), couple strongly to the relative degrees of freedom described by the sine-Gordon model. As of now, however, the extended system has only been studied using mean field theory [198] where the authors demonstrated that the coupling of the (anti)symmetric sectors leads to very little effects on the sine-Gordon time evolution. In light of the results of our simulations, a more fruitful approach would be the extension of the TWA to contain the symmetric modes as well.

Summary of thesis points

I. **I demonstrated that the weak integrability breaking of the spin-1/2 XXZ spin chain induced by perturbing it with one of its conserved generalised currents can be captured in the level spacing statistics of the perturbed system.**

It has been previously shown that perturbing an integrable spin chain by one of its higher conserved currents preserves the integrable properties of the system at first order in perturbation theory – in contrast to the usual 'strong' integrability breaking – therefore only 'weakly' breaking integrability.

Applying exact diagonalisation and computing the level spacing statistics as an indicator of the integrability breaking, I compared the finite size scaling of the crossover coupling of the strongly integrability-breaking next-to-nearest-neighbour interaction and the current perturbation and demonstrated that the latter breaks integrability in the weak sense. My findings were published in [85].

II. **I determined the range of validity of two popular semi-classical approaches, the self-consistent Hartree-Fock approximation (SCA) and the truncated Wigner approach (TWA), by simulating quantum quenches in the (1+1)d φ^4 theory and comparing the non-equilibrium time evolution to the truncated Hamiltonian approach (THA).**

I demonstrated the applicability of the THA for studying the non-equilibrium dynamics by quenching the mass and interaction parameters and analyzing the cutoff dependence of the time evolution of the one-point function for a wide range of quench strengths. I demonstrated the failure of the semi-classical approximations for increasing interaction strength and the rise of a symmetry-broken steady state in the TWA anytime the bare mass becomes negative. These results were published in [199].

III. **I simulated the decay of the false vacuum and numerically determined the bubble nucleation rate in the spontaneously symmetry-broken (1+1)d φ^4 theory.**

Using the truncated Hamiltonian approach, I simulated the real-time decay following quantum quenches in a system initiated close to the false vacuum and extracted the decay rate. The numerical results agree with the theoretical predictions up to an overall (numerical) normalisation factor that only depends on the interaction coupling of the theory. Moreover, these results establish the THA as a powerful tool to investigate

strongly non-perturbative phenomena, even in a non-equilibrium setting. I published my results in [200].

IV. **I simulated the non-equilibrium dynamics of the sine-Gordon model, partially describing a pair of Josephson-coupled one-dimensional bosonic quasi-condensates. The results establish that in the experimentally available weakly interacting regime, the dynamics can be well approximated by a semi-classical description and also clarify the role of the phononic modes of the theory.**

Using a novel version of THA based on a mini-superspace (MSTHA) and the truncated Wigner approximation, we simulated the time evolution of the one-point function and occupation numbers for a wide range of interaction strengths and two classes of quench protocols corresponding to small and large energy densities. Additionally, our results demonstrate that the MSTHA accurately describes the time evolution from the hard-core boson limit to the weakly interacting regime available in experiments when the injected energy density is sufficiently small. These findings were published in [174].

Appendix A

Computation of THA matrix elements

A.1 Massive free boson basis

Now we discuss the finite matrix representation of the finite volume Hamiltonian

$$\hat{H} = \hat{H}_{\mathrm{KG}}^m + \sum_{n=0}^{N} g_n \hat{V}_n \,; \qquad \hat{V}_n = \int_0^L dx : \hat{\varphi}^n : \tag{A.1}$$

in the basis of the massive free boson, given by the Klein-Gordon Hamiltonian

$$\hat{H}_{\mathrm{KG}}^m = \int_0^L dx : \left(\frac{1}{2}(\partial_t \hat{\varphi})^2 + \frac{1}{2}(\partial_x \hat{\varphi})^2 + \frac{1}{2}m^2 \hat{\varphi}^2 \right) : \,. \tag{A.2}$$

Here, normal ordering is carried out with respect to the free theory (A.2) and is denoted by semicolons. The free theory (A.2) can be diagonalised via Fourier transformation of the field $\hat{\varphi}$:

$$\hat{\varphi}(x,t) = \sum_k \frac{1}{\sqrt{2\omega_k L}} \left[a_k e^{-i(\omega_k t - kx)} + a_k^\dagger e^{i(\omega_k t - kx)} \right] \tag{A.3}$$

where the one-particle energies are given by $\omega_k = \sqrt{m^2 + k^2}$ and the momentum modes k form a discrete set which depends on the boundary condition:

$$k = \frac{2\pi n}{L} \tag{A.4}$$

with

$$
\begin{aligned}
&n = 0, \pm 1, \pm 2, \pm 3, \dots \quad \text{for periodic boundary condition } \hat{\varphi}(x+L) = \hat{\varphi}(x) \\
&n = \pm \frac{1}{2}, \pm \frac{3}{2}, \pm \frac{5}{2}, \dots \quad \text{for antiperiodic boundary condition } \hat{\varphi}(x+L) = -\hat{\varphi}(x) \,.
\end{aligned}
\tag{A.5}
$$

In Eq. (A.3), the field $\hat{\varphi}$ is expressed in terms of creation/annihilation operators $a_k^\dagger / a_k$ that satisfy the canonical commutation relations

$$[a_k, a_l] = [a_k^\dagger, a_l^\dagger] = 0, \quad [a_k, a_l^\dagger] = \delta_{kl} \,. \tag{A.6}$$

Substituting (A.3) into (A.2), the Klein-Gordon Hamiltonian becomes diagonal

$$\hat{H}_{\mathrm{KG}}^m = \sum_k \omega_k \, a_k^\dagger a_k \,. \tag{A.7}$$

Its eigenvectors are multiparticle states

$$\hat{H}_{\mathrm{KG}}^m \, |n_1, n_2, n_3, \ldots\rangle = \left(\sum_k n_k \omega_k \right) |n_1, n_2, n_3, \ldots\rangle \tag{A.8}$$

characterised by the occupation numbers n_k of the momentum modes k. They are created from the vacuum $|0\rangle$:

$$|n_1, n_2, n_3, \ldots\rangle = (a_1^\dagger)^{n_1} (a_2^\dagger)^{n_2} (a_3^\dagger)^{n_3} \ldots |0\rangle$$
$$a_k \, |0\rangle = 0 \tag{A.9}$$

and span the Hilbert space of the free massive boson, called the Fock space.

The matrix element of an operator $\hat{V}_n$ can be straightforwardly computed using the action of creation and annihilation operators on the Fock vectors

$$a_k^\dagger \, |n_1, n_2, n_3, \ldots, n_k, \ldots\rangle = \sqrt{n_k + 1} \, |n_1, n_2, n_3, \ldots, n_k + 1, \ldots\rangle$$
$$a_k \, |n_1, n_2, n_3, \ldots, n_k, \ldots\rangle = \sqrt{n_k} \, |n_1, n_2, n_3, \ldots, n_k - 1, \ldots\rangle \,, \tag{A.10}$$

together with the appropriate selection rules corresponding to momentum conservation originating from the integral in $\hat{V}_n$ (A.1):

$$\sum_j k_j^+ - \sum_j k_j^- = 0 \tag{A.11}$$

where the $\{k_j^+\}$ and $\{k_j^-\}$ are the set momentum modes corresponding to the set of creation (+) and annihilation (-) operators appearing in any given term in $\hat{V}_n$.

A.2 Massless free boson basis

In the MSTHA formalism, the sine-Gordon Hamiltonian

$$\hat{H}_{\mathrm{sG}} = \int_0^L dx : \left[\frac{1}{2} (\partial_t \hat{\varphi})^2 + \frac{1}{2} (\partial_x \hat{\varphi})^2 - \frac{\lambda}{2} \left(e^{i\beta\hat{\varphi}} + e^{-i\beta\hat{\varphi}} \right) \right] : \,. \tag{A.12}$$

is represented by a finite matrix on the eigenbasis free massless boson

$$\hat{H}_{\mathrm{FB}} = \int_0^L dx : \left[\frac{1}{2} (\partial_t \hat{\varphi})^2 + \frac{1}{2} (\partial_x \hat{\varphi})^2 \right] : \,. \tag{A.13}$$

To evaluate the matrix elements of the perturbing exponential operators, we first analytically continue the time t to Euclidean signature $\tau = -it$. The resulting space-time cylinder can be mapped to the complex plain parametrised by z by the conformal transformation

$$z = \exp \left\{ \frac{2\pi}{L} (\tau - ix) \right\} \quad, \quad \bar{z} = \exp \left\{ \frac{2\pi}{L} (\tau + ix) \right\} \,. \tag{A.14}$$

The transformation maps the exponential operators defined on the cylinder to the ones defined on the $(z, \bar{z})$-plane as

$$: e^{i\beta\nu\hat{\varphi}} :^{\text{cyl}} = \left(\frac{2\pi|z|}{L}\right)^{2h_\nu} : e^{i\beta\nu\hat{\varphi}} :^{\text{pl}} \tag{A.15}$$

with

$$h_\nu = \frac{\nu^2\beta^2}{8\pi} . \tag{A.16}$$

Their matrix element between arbitrary eigenstates $|\psi\rangle$ of the free Hamiltonian (A.13) can be computed as

$$\int_0^L dx \, \langle\psi'| : \exp\left\{i\nu\beta\hat{\varphi}(0, x)\right\} :^{\text{cyl}} |\psi\rangle = L\left(\frac{2\pi}{L}\right)^{2-2h_\nu} \langle\psi'| : \exp\left\{i\nu\beta\hat{\varphi}(1, 1)\right\} :^{\text{pl}} |\psi\rangle \, \delta_{s_\psi s_{\psi'}} \tag{A.17}$$

where the Kronecker delta ensures momentum conservation. Therefore, representing the cosine operator on the free boson basis reduces to computing the matrix elements

$$\langle\psi'| : \exp\left\{i\mu\beta\hat{\varphi}(1, 1)\right\} :^{\text{pl}} |\psi\rangle , \tag{A.18}$$

which can be straightforwardly performed [131]. Explicit formulas are given below.

To discuss the eigenstates $|\psi\rangle$ of (A.13), we first consider the Hamiltonian(s) truncated to the zero mode, equivalent to basic quantum mechanics with no spatial dependence. In the single-mode approximation, the sine-Gordon Hamiltonian (A.12) corresponds to a quantum pendulum

$$\hat{H}_{\text{QP}} = \frac{1}{2L}\hat{\pi}_0^2 - \lambda L\left(\frac{2\pi}{L}\right)^{2h} \cos(\beta\hat{\varphi}_0) . \tag{A.19}$$

Diagonalisation of the free part

$$\hat{H}_{\text{FQM}} = \frac{1}{2L}\hat{\pi}_0^2 = -\frac{1}{2L}\partial_{\varphi_0}^2 \tag{A.20}$$

yields solutions $\{|\nu\rangle\}$ in the form of plane waves:

$$|\nu\rangle = \sqrt{\frac{\beta}{2\pi}}e^{i\beta\nu\varphi_0} \tag{A.21}$$

$$\frac{1}{2L}\hat{\pi}_0^2 |\nu\rangle = \frac{(\nu\beta)^2}{2L} |\nu\rangle . \tag{A.22}$$

which are created by the exponential operators from the vacuum $|0\rangle$:

$$|\nu\rangle = e^{i\beta\nu\hat{\varphi}_0} |0\rangle , \quad |0\rangle = \frac{\beta}{2\pi} . \tag{A.23}$$

The exponential operators act as ladder operators on the plane wave basis:

$$e^{\pm i\mu\beta\hat{\varphi}_0} |\nu\rangle = |\nu \pm \mu\rangle . \tag{A.24}$$

Finally, the eigenstates of the free boson (A.13) are multiparticle states built upon the plane wave basis $\{|\nu\rangle\}$:

$$\mathcal{H}_{\text{FB}} = \bigoplus_{\nu \in \mathbb{Z}} \mathcal{F}_\nu, \tag{A.25}$$

where each Fock module $\mathcal{F}_\nu$ is composed of free multiparticle states (containing left- and right-moving particles) built upon the appropriate plane wave $|\nu\rangle$

$$\mathcal{F}_\nu = \left\{ |\psi\rangle = \prod_{k>0} a_{-k}^{r_k} \bar{a}_{-k}^{\bar{r}_k} |\nu\rangle \,\bigg|\, r_k, \bar{r}_k \in \mathbb{N}^+ \right\}. \tag{A.26}$$

Now we compute the matrix elements (A.18) of the exponential operators

$$\langle \psi' | : \exp\left\{i\mu\beta\hat{\varphi}(1,1)\right\} :^{\text{pl}} |\psi\rangle \tag{A.27}$$

between the free boson eigenstates

$$\begin{aligned} |\psi\rangle &= \frac{1}{N_\psi} \prod_{k=1}^\infty a_{-k}^{r_k} \bar{a}_{-k}^{s_k} |\nu\rangle \\ |\psi'\rangle &= \frac{1}{N_{\psi'}} \prod_{k=1}^\infty a_{-k}^{r'_k} \bar{a}_{-k}^{s'_k} |\nu'\rangle \,. \end{aligned} \tag{A.28}$$

The normalisation factors have the form

$$N_\psi^2 = \prod_{k=1}^\infty \langle a_k^{r_k} a_{-k}^{r_k}\rangle \langle \bar{a}_k^{s_k} \bar{a}_{-k}^{s_k}\rangle = \prod_{k=1}^\infty (r_k! k^{r_k})(s_k! k^{s_k}) \tag{A.29}$$

and ensure that the conformal basis is orthonormal:

$$\langle \psi' | \psi \rangle = \delta_{\nu,\nu'} \prod_{k=1}^\infty \delta_{r_k, r'_k} \delta_{s_k, s'_k} \,. \tag{A.30}$$

Due to the normal ordering, the exponential operators at positions $z = \bar{z} = 1$ take the form

$$: \exp\left\{i\mu\beta\hat{\varphi}(1,1)\right\} :^{\text{pl}} = e^{i\mu\beta\hat{\varphi}_0} \prod_{k=1}^\infty e^{\alpha \frac{a_{-k}}{k}} e^{-\alpha \frac{a_k}{k}} e^{\alpha \frac{\bar{a}_{-k}}{k}} e^{-\alpha \frac{\bar{a}_k}{k}} \tag{A.31}$$

where

$$\alpha = \frac{\mu\beta}{\sqrt{4\pi}} \,. \tag{A.32}$$

The matrix element (A.18) can now be expressed as

$$\begin{aligned} &\langle \psi' | : \exp\left\{i\mu\beta\hat{\varphi}(1,1)\right\} :^{\text{pl}} |\psi\rangle = \\ &= \frac{1}{N_\psi N_{\psi'}} \delta_{\nu',\nu+\mu} \prod_{k=1}^\infty \langle a_k^{r'_k} e^{\alpha \frac{a_{-k}}{k}} e^{-\alpha \frac{a_k}{k}} a_{-k}^{r_k}\rangle \langle \bar{a}_k^{s'_k} e^{\alpha \frac{\bar{a}_{-k}}{k}} e^{-\alpha \frac{\bar{a}_k}{k}} \bar{a}_{-k}^{s_k}\rangle \\ &= \frac{1}{N_\psi N_{\psi'}} \delta_{\nu',\nu+\mu} \left[\prod_{k=1}^\infty \langle a_k^{r'_k} e^{\alpha \frac{a_{-k}}{k}} e^{-\alpha \frac{a_k}{k}} a_{-k}^{r_k}\rangle\right] \left[\prod_{k=1}^\infty \langle \bar{a}_k^{s'_k} e^{\alpha \frac{\bar{a}_{-k}}{k}} e^{-\alpha \frac{\bar{a}_k}{k}} \bar{a}_{-k}^{s_k}\rangle\right] \,. \end{aligned} \tag{A.33}$$

Finally, the contribution of a single mode to the expectation value can be evaluated as follows:

$$\langle a_k^{r'_k} e^{\alpha \frac{a_{-k}}{k}} e^{-\alpha \frac{a_k}{k}} a_{-k}^{r_k} \rangle = \sum_{j'=0}^{\infty} \sum_{j=0}^{\infty} \frac{(-1)^j}{j! j'!} \left(\frac{\alpha}{k}\right)^{j+j'} \langle a_k^{r'_k} a_{-k}^{j'} a_k^{j} a_{-k}^{r_k} \rangle \ , \tag{A.34}$$

where

$$\langle a_k^{r'_k} a_{-k}^{j'} a_k^{j} a_{-k}^{r_k} \rangle = k^{j+j'} \binom{r_k}{j} \binom{r'_k}{j'} j! j'! (r_k - j)! k^{r_k - j} \delta_{r_k - j, r'_k - j'} \ . \tag{A.35}$$

Appendix B

Bosonisation of a pair of coupled bosonic quasi-condensates

The dynamics of a one-dimensional bosonic quasi-condensate is governed by the Hamiltonian

$$\hat{H}_{\mathrm{QC}} = \int dz \ \hat{\psi}^\dagger(z) \left[-\frac{\hbar}{2m}\partial_z^2 + V(z) - \mu \right] \hat{\psi}(z) + \frac{g}{2} \int dz \ \hat{\psi}^\dagger(z)\hat{\psi}^\dagger(z)\hat{\psi}(z)\hat{\psi}(z) \,, \qquad \text{(B.1)}$$

where the bosonic field operators satisfy the common canonical commutation relations

$$[\hat{\psi}(z), \hat{\psi}^\dagger(z')] = i\delta(z - z') \,. \qquad \text{(B.2)}$$

The atoms are subject to a longitudinal trapping potential $V(z)$, μ is the chemical potential, and g is some effective one-dimensional coupling. The strength of the interactions between atoms is characterised by the parameter

$$\gamma = \frac{mg}{\hbar^2 \rho_0} \,, \qquad \text{(B.3)}$$

where ρ_0 is the longitudinal density of atoms. Bosonisation of the condensate starts by expressing the field variable in terms of density $\hat{\rho}(z)$ and phase fields $\hat{\theta}(z)$ as

$$\hat{\psi}(z) = \sqrt{\hat{\rho}(z)}e^{i\hat{\theta}(z)}; \quad \hat{\rho} = \rho_0 + \delta\hat{\rho} \,. \qquad \text{(B.4)}$$

the density fluctuations $\delta\hat{\rho}$ and the phase field $\hat{\theta}$ obey the commutation relations $[\hat{\theta}(z), \delta\hat{\rho}(z')] = i\delta(z - z')$. Substituting (B.4) to (B.1) and expanding to second order in density and phase fluctuations yields a low-energy effective field theory in the form of the Tomonaga-Luttinger-liquid Hamiltonian

$$\hat{H}_{\mathrm{TLL}} = \frac{\hbar}{2\pi} \int dz \ \left[\nu_N \pi^2 \delta\hat{\rho}^2 + \nu_J(\partial_z\hat{\theta})^2 \right] \,. \qquad \text{(B.5)}$$

The parameters $\nu_{N/J}$ are called the density/phase stiffness and can be written in terms of the parameters characterising the condensate:

$$\nu_J = \frac{\pi\hbar\rho_0}{m}, \qquad \nu_N = \frac{1}{\pi\hbar}\partial_{\rho_0}\mu \overset{\gamma \ll 1}{\approx} \frac{g}{\pi\hbar} \,. \qquad \text{(B.6)}$$

Due to the confining potential $V(z)$, the background density ρ_0 and the parameters (B.6) carry a z-dependence. We focus on homogeneous systems so the spatial dependence can be dropped. Introducing the Luttinger parameter $\tilde{K}$ and sound velocity c

$$\tilde{K} = \sqrt{\frac{\nu_J}{\nu_N}}, \qquad c = \sqrt{\nu_J \nu_N}, \tag{B.7}$$

the Hamiltonian (B.5) can be brought to the usual Luttinger liquid form:

$$\hat{H}_{\mathrm{TLL}} = \frac{\hbar c}{2} \int dz \, \left[\frac{\pi}{\tilde{K}} \delta\hat{\rho}^2 + \frac{\tilde{K}}{\pi} (\partial_z \hat{\theta})^2 \right]. \tag{B.8}$$

Loading a pair of bosonic one-dimensional quasi-condensates to a longitudinally elongated double well potential, the finite potential barrier instigates a coupling between the condensate pair through quantum mechanical tunnelling. The system can be described by the Hamiltonian:

$$\hat{H}_{\mathrm{QCP}} = \sum_{j=1,2} \int dz \, \hat{\psi}_j^\dagger(z) \left[-\frac{\hbar}{2m} \partial_z^2 + V(z) - \mu_j \right] \hat{\psi}_j(z) + \frac{g}{2} \int dz \, \hat{\psi}_j^\dagger(z) \hat{\psi}_j^\dagger(z) \hat{\psi}_j(z) \hat{\psi}_j(z)$$
$$-\hbar J \int dz \, \left[\hat{\psi}_1^\dagger \hat{\psi}_2 + \hat{\psi}_2^\dagger \hat{\psi}_1 \right], \tag{B.9}$$

where the last term describes the tunnelling of particles between the condensates with tunnel coupling J. Setting $\mu_1 = \mu_2 = \mu$ and introducing the density-phase variables as

$$\hat{\psi}_j(z) = \sqrt{\hat{\rho}_j(z)} e^{i\hat{\theta}_j(z)}; \quad \hat{\rho} = \rho_0 + \delta\hat{\rho}_j, \tag{B.10}$$

the coupled condensate pair can be bosonised by substituting (B.10) to (B.9) and expanding the Hamiltonian up to the second order in the fluctuations. The resulting Hamiltonian describes a pair of Luttinger liquids

$$\hat{H}_{\mathrm{QCP}} = \hat{H}_{\mathrm{TLL},\,1}(\tilde{K}) + \hat{H}_{\mathrm{TLL},\,2}(\tilde{K}) + \hat{H}_J(\hat{\theta}_1 - \hat{\theta}_2) \tag{B.11}$$

with an interaction Hamiltonian $\hat{H}_J$ coupling them together. Here, we explicitly indicated the Luttinger parameters that parameterise the TLL Hamiltonians. Since $\hat{H}_J$ only depends on the relative phase $\hat{\theta}_1 - \hat{\theta}_2$, it is helpful to perform a change of variables of the form

$$
\begin{aligned}
\delta\hat{\rho}_c &= \delta\hat{\rho}_1 + \delta\hat{\rho}_2 \\
\delta\hat{\rho}_r &= \frac{\delta\hat{\rho}_1 - \delta\hat{\rho}_2}{2} \\
\hat{\theta}_c &= \frac{\hat{\theta}_1 + \hat{\theta}_2}{2} \\
\hat{\theta}_r &= \hat{\theta}_1 - \hat{\theta}_2.
\end{aligned}
\tag{B.12}
$$

Here, the subscripts r/c denote the relative/common (or antisymmetric/symmetric) degrees of freedom. The Luttinger liquid of the Hamiltonian (B.11) can be brought to the form

$$\hat{H}_{\mathrm{TLL},\,1}(\tilde{K}) + \hat{H}_{\mathrm{TLL},\,2}(\tilde{K}) = \hat{H}_{\mathrm{TLL},\,c}(K_c) + \hat{H}_{\mathrm{TLL},\,r}(K_r) \tag{B.13}$$

with $K_c = 2\tilde{K}$ and $K_r = \tilde{K}/2$. The interaction Hamiltonian $\hat{H}_J$ can be expanded in the density fluctuations up to second order to yield

$$\hat{H}_J = -\hbar J \int dz \ [2\rho_0 + \delta\hat{\rho}_c] (\cos\hat{\theta}_r - 1) + \frac{\hbar J}{\rho_0} \delta\hat{\rho}_r^2 \cos\hat{\theta}_r$$

$$\approx -2\hbar J\rho_0 \int dz \ \cos\hat{\theta}_r \,. \tag{B.14}$$

The second line is obtained by neglecting the density fluctuations and results in the decoupling of the common and relative degrees of freedom:

$$\hat{H}_c = \frac{\hbar c}{2} \int dz \ \left[\frac{\pi}{2\tilde{K}} \delta\hat{\rho}_c^2 + \frac{2\tilde{K}}{\pi} (\partial_z\hat{\theta}_c)^2 \right] \tag{B.15}$$

$$\hat{H}_r = \frac{\hbar c}{2} \int dz \ \left[\frac{2\pi}{\tilde{K}} \delta\hat{\rho}_r^2 + \frac{\tilde{K}}{2\pi} (\partial_z\hat{\theta}_r)^2 \right] - 2\hbar J\rho_0 \int dz \ \cos\hat{\theta}_r \,, \tag{B.16}$$

revealing the relative mode dynamics to be described by the sine-Gordon model. We can bring $\hat{H}_r$ to a more familiar form by redefining the canonical variables as

$$\hat{\varphi} = \beta^{-1}\hat{\theta}_r \quad , \quad \hat{\pi} = \beta\delta\hat{\rho}_r \tag{B.17}$$

with

$$\beta = \sqrt{\frac{2\pi}{\tilde{K}}} = \sqrt{\frac{\pi}{K_r}} \,, \tag{B.18}$$

leading to the usual form of the sine-Gordon model:

$$\hat{H}_{\mathrm{sG}} = \frac{1}{2} \int dz \ [\hat{\pi}^2 + (\partial_z\hat{\varphi})^2] - \lambda \int dz : \cos\beta\hat{\varphi} : \,. \tag{B.19}$$

The normal ordering in the above Hamiltonian is obtained by redefining the coupling λ, which now has a dimension [energy]$^{2-2h}$, where $2h = \beta^2/4\pi$ is the anomalous dimension of the cosine operator. Here, we remark that throughout the main text, we consider the dynamics of the relative phase and omit the contributions coming from the common degrees of freedom, and so we drop the subscript of the relative Luttinger parameter K_r and simply refer to it as K.

Bibliography

[1] G. Mussardo, *Statistical Field Theory: An Introduction to Exactly Solved Models in Statistical Physics (2nd edn)*. 2020.

[2] S. Hofferberth, I. Lesanovsky, B. Fischer, T. Schumm, and J. Schmiedmayer, "Non-equilibrium coherence dynamics in one-dimensional Bose gases," *Nature* **449** (2007) 324–327, `arXiv:0706.2259 [cond-mat.other]`.

[3] F. Meinert, M. J. Mark, E. Kirilov, K. Lauber, P. Weinmann, A. J. Daley, and H. C. Nägerl, "Quantum Quench in an Atomic One-Dimensional Ising Chain," *Phys. Rev. Lett.* **111** (2013) 053003, `arXiv:1304.2628 [cond-mat.quant-gas]`.

[4] M. Gring, M. Kuhnert, T. Langen, T. Kitagawa, B. Rauer, M. Schreitl, I. Mazets, D. A. Smith, E. Demler, and J. Schmiedmayer, "Relaxation and Prethermalization in an Isolated Quantum System," *Science* **337** (2012) 1318, `arXiv:1112.0013 [cond-mat.quant-gas]`.

[5] S. Trotzky, Y. A. Chen, A. Flesch, I. P. McCulloch, U. Schollwöck, J. Eisert, and I. Bloch, "Probing the relaxation towards equilibrium in an isolated strongly correlated one-dimensional Bose gas," *Nature Physics* **8** (2012) 325–330, `arXiv:1101.2659 [cond-mat.quant-gas]`.

[6] T. Fukuhara, P. Schauß, M. Endres, S. Hild, M. Cheneau, I. Bloch, and C. Gross, "Microscopic observation of magnon bound states and their dynamics," *Nature* **502** (2013) 76–79, `arXiv:1305.6598 [cond-mat.quant-gas]`.

[7] M. Cheneau, P. Barmettler, D. Poletti, M. Endres, P. Schauß, T. Fukuhara, C. Gross, I. Bloch, C. Kollath, and S. Kuhr, "Light-cone-like spreading of correlations in a quantum many-body system," *Nature* **481** (2012) 484–487, `arXiv:1111.0776 [cond-mat.quant-gas]`.

[8] T. Langen, R. Geiger, M. Kuhnert, B. Rauer, and J. Schmiedmayer, "Local emergence of thermal correlations in an isolated quantum many-body system," *Nature Physics* **9** (2013) 640–643, `arXiv:1305.3708 [cond-mat.quant-gas]`.

[9] M. H. Anderson, J. R. Ensher, M. R. Matthews, C. E. Wieman, and E. A. Cornell, "Observation of Bose-Einstein Condensation in a Dilute Atomic Vapor," *Science* **269** (1995) 198–201.

[10] K. B. Davis, M. O. Mewes, M. R. Andrews, N. J. van Druten, D. S. Durfee, D. M. Kurn, and W. Ketterle, "Bose-Einstein condensation in a gas of sodium atoms," *Phys. Rev. Lett.* **75** (1995) 3969–3973.

[11] M. Kruczenski, J. Penedones, and B. C. van Rees, "Snowmass White Paper: S-matrix Bootstrap," *arXiv e-prints* (2022) arXiv:2203.02421, `arXiv:2203.02421 [hep-th]`.

[12] V. E. Korepin, N. M. Bogoliubov, and A. G. Izergin, *Quantum Inverse Scattering Method and Correlation Functions*. 1993.

[13] L. D. Faddeev, "How Algebraic Bethe Ansatz works for integrable model," *arXiv e-prints* (1996) hep–th/9605187, `arXiv:hep-th/9605187 [hep-th]`.

[14] F. Franchini, *An Introduction to Integrable Techniques for One-Dimensional Quantum Systems*, vol. 940. 2017.

[15] P. Calabrese, F. H. L. Essler, and G. Mussardo, "Introduction to 'quantum integrability in out of equilibrium systems'," *Journal of Statistical Mechanics: Theory and Experiment* **2016** (2016) 064001. `https://dx.doi.org/10.1088/1742-5468/2016/06/064001`.

[16] T. Langen, S. Erne, R. Geiger, B. Rauer, T. Schweigler, M. Kuhnert, W. Rohringer, I. E. Mazets, T. Gasenzer, and J. Schmiedmayer, "Experimental observation of a generalized Gibbs ensemble," *Science* **348** (2015) 207–211, `arXiv:1411.7185 [cond-mat.quant-gas]`.

[17] T. Kinoshita, T. Wenger, and D. S. Weiss, "A quantum Newton's cradle," *Nature* **440** (2006) 900–903.

[18] N. Beisert, C. Ahn, L. F. Alday, Z. Bajnok, J. M. Drummond, L. Freyhult, N. Gromov, R. A. Janik, V. Kazakov, T. Klose, G. P. Korchemsky, C. Kristjansen, M. Magro, T. McLoughlin, J. A. Minahan, R. I. Nepomechie, A. Rej, R. Roiban, S. Schäfer-Nameki, C. Sieg, M. Staudacher, A. Torrielli, A. A. Tseytlin, P. Vieira, D. Volin, and K. Zoubos, "Review of AdS/CFT Integrability: An Overview," *Letters in Mathematical Physics* **99** (2012) 3–32, `arXiv:1012.3982 [hep-th]`.

[19] P. Calabrese and J. Cardy, "Time Dependence of Correlation Functions Following a Quantum Quench," *Phys. Rev. Lett.* **96** (2006) 136801, `arXiv:cond-mat/0601225 [cond-mat.stat-mech]`.

[20] P. Calabrese and J. Cardy, "Quantum quenches in extended systems," *Journal of Statistical Mechanics: Theory and Experiment* **2007** (2007) 06008, `arXiv:0704.1880 [cond-mat.stat-mech]`.

[21] J.-S. Caux and F. H. L. Essler, "Time Evolution of Local Observables After Quenching to an Integrable Model," *Phys. Rev. Lett.* **110** (2013) 257203, `arXiv:1301.3806 [cond-mat.stat-mech]`.

[22] J.-S. Caux, "The Quench Action," *Journal of Statistical Mechanics: Theory and Experiment* **6** (2016) 064006, `arXiv:1603.04689 [cond-mat.str-el]`.

[23] D. Schuricht and F. H. L. Essler, "Dynamics in the Ising field theory after a quantum quench," *Journal of Statistical Mechanics: Theory and Experiment* **2012** (2012) 04017, `arXiv:1203.5080 [cond-mat.str-el]`.

[24] B. Bertini, D. Schuricht, and F. H. L. Essler, "Quantum quench in the sine-Gordon model," *Journal of Statistical Mechanics: Theory and Experiment* **2014** (2014) 10035, `arXiv:1405.4813 [cond-mat.stat-mech]`.

[25] J. M. Deutsch, "Quantum statistical mechanics in a closed system," *Phys. Rev. A* **43** (1991) 2046–2049.

[26] M. Srednicki, "Chaos and quantum thermalization," *Phys. Rev. E* **50** (1994) 888–901, `arXiv:cond-mat/9403051 [cond-mat]`.

[27] M. Rigol and M. Srednicki, "Alternatives to Eigenstate Thermalization," *Phys. Rev. Lett.* **108** (2012) 110601, `arXiv:1108.0928 [cond-mat.stat-mech]`.

[28] M. Rigol, V. Dunjko, and M. Olshanii, "Thermalization and its mechanism for generic isolated quantum systems," *Nature* **452** (2008) 854–858, `arXiv:0708.1324 [cond-mat.stat-mech]`.

[29] M. Srednicki, "The approach to thermal equilibrium in quantized chaotic systems," *Journal of Physics A Mathematical General* **32** (1999) 1163–1175, `arXiv:cond-mat/9809360 [cond-mat.stat-mech]`.

[30] W. Beugeling, R. Moessner, and M. Haque, "Off-diagonal matrix elements of local operators in many-body quantum systems," *Phys. Rev. E* **91** (2015) 012144. `https://link.aps.org/doi/10.1103/PhysRevE.91.012144`.

[31] M. Rigol, "Breakdown of Thermalization in Finite One-Dimensional Systems," *Phys. Rev. Lett.* **103** (2009) 100403, `arXiv:0904.3746 [cond-mat.stat-mech]`.

[32] M. Rigol, "Quantum quenches and thermalization in one-dimensional fermionic systems," *Phys. Rev. A* **80** (2009) 053607, `arXiv:0908.3188 [cond-mat.stat-mech]`.

[33] J. R. Schrieffer and P. A. Wolff, "Relation between the Anderson and Kondo Hamiltonians," *Phys. Rev.* **149** (1966) 491–492.

[34] R. Steinigeweg, J. Herbrych, and P. Prelovšek, "Eigenstate thermalization within isolated spin-chain systems," *Phys. Rev. E* **87** (2013) 012118, `arXiv:1208.6143 [cond-mat.str-el]`.

[35] W. Beugeling, R. Moessner, and M. Haque, "Finite-size scaling of eigenstate thermalization," *Phys. Rev. E* **89** (2014) 042112, `arXiv:1308.2862 [cond-mat.stat-mech]`.

[36] H. Kim, T. N. Ikeda, and D. A. Huse, "Testing whether all eigenstates obey the eigenstate thermalization hypothesis," *Phys. Rev. E* **90** (2014) 052105, `arXiv:1408.0535 [cond-mat.stat-mech]`.

[37] R. Mondaini, K. R. Fratus, M. Srednicki, and M. Rigol, "Eigenstate thermalization in the two-dimensional transverse field Ising model," *Phys. Rev. E* **93** (2016) 032104, `arXiv:1512.04947 [cond-mat.stat-mech]`.

[38] R. Steinigeweg, A. Khodja, H. Niemeyer, C. Gogolin, and J. Gemmer, "Pushing the Limits of the Eigenstate Thermalization Hypothesis towards Mesoscopic Quantum Systems," *Phys. Rev. Lett.* **112** (2014) 130403, `arXiv:1311.0169 [cond-mat.stat-mech]`.

[39] S. Sorg, L. Vidmar, L. Pollet, and F. Heidrich-Meisner, "Relaxation and thermalization in the one-dimensional Bose-Hubbard model: A case study for the interaction quantum quench from the atomic limit," *Phys. Rev. A* **90** (2014) 033606, `arXiv:1405.5404 [cond-mat.stat-mech]`.

[40] M. Rigol, V. Dunjko, V. Yurovsky, and M. Olshanii, "Relaxation in a Completely Integrable Many-Body Quantum System: An AbInitio Study of the Dynamics of the Highly Excited States of 1D Lattice Hard-Core Bosons," *Phys. Rev. Lett.* **98** (2007) 050405, `arXiv:cond-mat/0604476 [cond-mat.other]`.

[41] M. Rigol, A. Muramatsu, and M. Olshanii, "Hard-core bosons on optical superlattices: Dynamics and relaxation in the superfluid and insulating regimes," *Phys. Rev. A* **74** (2006) 053616, `arXiv:cond-mat/0612415 [cond-mat.other]`.

[42] E. T. Jaynes, "Information theory and statistical mechanics," *Phys. Rev.* **106** (1957) 620–630. `https://link.aps.org/doi/10.1103/PhysRev.106.620`.

[43] D. Rossini, A. Silva, G. Mussardo, and G. E. Santoro, "Effective Thermal Dynamics Following a Quantum Quench in a Spin Chain," *Phys. Rev. Lett.* **102** (2009) 127204, `arXiv:0810.5508 [cond-mat.stat-mech]`.

[44] D. Rossini, S. Suzuki, G. Mussardo, G. E. Santoro, and A. Silva, "Long time dynamics following a quench in an integrable quantum spin chain: Local versus nonlocal operators and effective thermal behavior," *Phys. Rev. B* **82** (2010) 144302, `arXiv:1002.2842 [cond-mat.stat-mech]`.

[45] P. Calabrese, F. H. L. Essler, and M. Fagotti, "Quantum quench in the transverse field Ising chain: I. Time evolution of order parameter correlators," *Journal of Statistical Mechanics: Theory and Experiment* **2012** (2012) 07016, `arXiv:1204.3911 [cond-mat.quant-gas]`.

[46] P. Calabrese, F. H. L. Essler, and M. Fagotti, "Quantum quenches in the transverse field Ising chain: II. Stationary state properties," *Journal of Statistical Mechanics: Theory and Experiment* **2012** (2012) 07022, `arXiv:1205.2211 [cond-mat.stat-mech]`.

[47] B. Blass, H. Rieger, and F. Iglói, "Quantum relaxation and finite-size effects in the XY chain in a transverse field after global quenches," *EPL (Europhysics Letters)* **99** (2012) 30004, `arXiv:1205.3303 [cond-mat.stat-mech]`.

[48] B. Wouters, J. De Nardis, M. Brockmann, D. Fioretto, M. Rigol, and J. S. Caux, "Quenching the Anisotropic Heisenberg Chain: Exact Solution and Generalized Gibbs Ensemble Predictions," *Phys. Rev. Lett.* **113** (2014) 117202, `arXiv:1405.0172 [cond-mat.str-el]`.

[49] B. Pozsgay, M. Mestyán, M. A. Werner, M. Kormos, G. Zaránd, and G. Takács, "Correlations after Quantum Quenches in the XXZ Spin Chain: Failure of the Generalized Gibbs Ensemble," *Phys. Rev. Lett.* **113** (2014) 117203, `arXiv:1405.2843 [cond-mat.stat-mech]`.

[50] E. Ilievski, J. De Nardis, B. Wouters, J. S. Caux, F. H. L. Essler, and T. Prosen, "Complete Generalized Gibbs Ensembles in an Interacting Theory," *Phys. Rev. Lett.* **115** (2015) 157201, `arXiv:1507.02993 [quant-ph]`.

[51] E. Ilievski, M. Medenjak, T. Prosen, and L. Zadnik, "Quasilocal charges in integrable lattice systems," *Journal of Statistical Mechanics: Theory and Experiment* **6** (2016) 064008, `arXiv:1603.00440 [cond-mat.stat-mech]`.

[52] E. Ilievski, M. Medenjak, and T. Prosen, "Quasilocal Conserved Operators in the Isotropic Heisenberg Spin-1 /2 Chain," *Phys. Rev. Lett.* **115** (2015) 120601, `arXiv:1506.05049 [cond-mat.stat-mech]`.

[53] G. Fehér and B. Pozsgay, "Generalized Gibbs Ensemble and string-charge relations in nested Bethe Ansatz," *SciPost Physics* **8** (2020) 034, `arXiv:1909.04470 [cond-mat.stat-mech]`.

[54] C. J. Turner, A. A. Michailidis, D. A. Abanin, M. Serbyn, Papić, and Z. , "Weak ergodicity breaking from quantum many-body scars," *Nat. Phys.* **14** (2018) 745–749.

[55] M. Serbyn, D. A. Abanin, and Z. Papić, "Quantum many-body scars and weak breaking of ergodicity," *Nat. Phys.* **17** (2021) 675–685, `arXiv:2011.09486 [quant-ph]`.

[56] W. W. Ho, S. Choi, H. Pichler, and M. D. Lukin, "Periodic orbits, entanglement, and quantum many-body scars in constrained models: Matrix product state approach," *Phys. Rev. Lett.* **122** (2019) 040603. `https://link.aps.org/doi/10.1103/PhysRevLett.122.040603`.

[57] G. Biroli, C. Kollath, and A. M. Läuchli, "Effect of Rare Fluctuations on the Thermalization of Isolated Quantum Systems," *Phys. Rev. Lett.* **105** (2010) 250401, `arXiv:0907.3731 [cond-mat.quant-gas]`.

[58] C. J. Turner, A. A. Michailidis, D. A. Abanin, M. Serbyn, and Z. Papić, "Quantum scarred eigenstates in a Rydberg atom chain: Entanglement, breakdown of

thermalization, and stability to perturbations," *Phys. Rev. B* **98** (2018) 155134, `arXiv:1806.10933 [cond-mat.quant-gas]`.

[59] S. Moudgalya, B. A. Bernevig, and N. Regnault, "Quantum many-body scars and Hilbert space fragmentation: a review of exact results," *Reports on Progress in Physics* **85** (2022) 086501, `arXiv:2109.00548 [cond-mat.str-el]`.

[60] A. Chandran, T. Iadecola, V. Khemani, and R. Moessner, "Quantum Many-Body Scars: A Quasiparticle Perspective," *Annual Review of Condensed Matter Physics* **14** (2023) 443–469, `arXiv:2206.11528 [cond-mat.str-el]`.

[61] V. Oganesyan and D. A. Huse, "Localization of interacting fermions at high temperature," *Phys. Rev. B* **75** (2007) 155111, `arXiv:cond-mat/0610854 [cond-mat.str-el]`.

[62] R. Nandkishore and D. A. Huse, "Many-Body Localization and Thermalization in Quantum Statistical Mechanics," *Annual Review of Condensed Matter Physics* **6** (2015) 15–38, `arXiv:1404.0686 [cond-mat.stat-mech]`.

[63] A. Pal and D. A. Huse, "Many-body localization phase transition," *Phys. Rev. B* **82** (2010) 174411, `arXiv:1010.1992 [cond-mat.dis-nn]`.

[64] M. Serbyn, Z. Papić, and D. A. Abanin, "Quantum quenches in the many-body localized phase," *Phys. Rev. B* **90** (2014) 174302, `arXiv:1408.4105 [cond-mat.dis-nn]`.

[65] M. Tarzia, "Many-body localization transition in Hilbert space," *Phys. Rev. B* **102** (2020) 014208, `arXiv:2003.11847 [cond-mat.stat-mech]`.

[66] L. Herviou, J. H. Bardarson, and N. Regnault, "Many-body localization in a fragmented Hilbert space," *Phys. Rev. B* **103** (2021) 134207, `arXiv:2011.04659 [cond-mat.dis-nn]`.

[67] D. A. Abanin and Z. Papić, "Recent progress in many-body localization," *Annalen der Physik* **529** (2017) 1700169, `arXiv:1705.09103 [cond-mat.dis-nn]`.

[68] F. Alet and N. Laflorencie, "Many-body localization: An introduction and selected topics," *Comptes Rendus Physique* **19** (2018) 498–525, `arXiv:1711.03145 [cond-mat.str-el]`.

[69] P. W. Anderson, "Absence of Diffusion in Certain Random Lattices," *Phys. Rev.* **109** (1958) 1492–1505.

[70] J. Z. Imbrie, "On Many-Body Localization for Quantum Spin Chains," *Journal of Statistical Physics* **163** (2016) 998–1048, `arXiv:1403.7837 [math-ph]`.

[71] W. L. Tan, P. Becker, F. Liu, G. Pagano, K. S. Collins, A. De, L. Feng, H. B. Kaplan, A. Kyprianidis, R. Lundgren, W. Morong, S. Whitsitt, A. V. Gorshkov, and C. Monroe, "Domain-wall confinement and dynamics in a quantum simulator," *Nat. Phys.* **17** (2021) 742–747, `arXiv:1912.11117 [quant-ph]`.

[72] G. Pagano, P. W. Hess, H. B. Kaplan, W. L. Tan, P. Richerme, P. Becker, A. Kyprianidis, J. Zhang, E. Birckelbaw, M. R. Hernandez, Y. Wu, and C. Monroe, "Cryogenic trapped-ion system for large scale quantum simulation," *Quantum Science and Technology* **4** (2019) 014004, `arXiv:1802.03118 [quant-ph]`.

[73] A. Signoles, T. Franz, R. Ferracini Alves, M. Gärttner, S. Whitlock, G. Zürn, and M. Weidemüller, "Glassy Dynamics in a Disordered Heisenberg Quantum Spin System," *Phys. Rev. X* **11** (2021) 011011, `arXiv:1909.11959 [quant-ph]`.

[74] O. Breunig, M. Garst, E. Sela, B. Buldmann, P. Becker, L. Bohatý, R. Müller, and T. Lorenz, "Spin-(1)/(2) XXZ Chain System Cs_2CoCl_4 in a Transverse Magnetic Field," *Phys. Rev. Lett.* **111** (2013) 187202, `arXiv:1307.2870 [cond-mat.str-el]`.

[75] R. Toskovic, R. van den Berg, A. Spinelli, I. S. Eliens, B. van den Toorn, B. Bryant, J. S. Caux, and A. F. Otte, "Atomic spin-chain realization of a model for quantum criticality," *Nat. Phys.* **12** (2016) 656–660, `arXiv:1604.05597 [cond-mat.mes-hall]`.

[76] B. Pozsgay, "Algebraic Construction of Current Operators in Integrable Spin Chains," *Phys. Rev. Lett.* **125** (2020) 070602, `arXiv:2005.06242 [cond-mat.stat-mech]`.

[77] J. Elias-Miró, J. R. Espinosa, G. F. Giudice, G. Isidori, A. Riotto, and A. Strumia, "Higgs mass implications on the stability of the electroweak vacuum," *Physics Letters B* **709** (2012) 222–228, `arXiv:1112.3022 [hep-ph]`.

[78] M. Serone, G. Spada, and G. Villadoro, "$\lambda\phi^4$ theory — Part I. The symmetric phase beyond NNNNNNNNLO," *JHEP* **2018** (2018) 148, `arXiv:1805.05882 [hep-th]`.

[79] M. Serone, G. Spada, and G. Villadoro, "$\lambda\phi^4$ theory — Part II. the broken phase beyond NNNN(NNNN)LO," *JHEP* **2019** (2019) 47, `arXiv:1901.05023 [hep-th]`.

[80] A. Coser, M. Beria, G. P. Brandino, R. M. Konik, and G. Mussardo, "Truncated conformal space approach for 2D Landau-Ginzburg theories," *Journal of Statistical Mechanics: Theory and Experiment* **2014** (2014) 12010, `arXiv:1409.1494 [hep-th]`.

[81] M. Hogervorst, S. Rychkov, and B. C. van Rees, "Truncated conformal space approach in d dimensions: A cheap alternative to lattice field theory?," *Phys. Rev. D* **91** (2015) 025005, `arXiv:1409.1581 [hep-th]`.

[82] S. Rychkov and L. G. Vitale, "Hamiltonian truncation study of the φ^4 theory in two dimensions," *Phys. Rev. D* **91** (2015) 085011, `arXiv:1412.3460 [hep-th]`.

[83] S. Rychkov and L. G. Vitale, "Hamiltonian truncation study of the ϕ^4 theory in two dimensions. II. The Z_2 -broken phase and the Chang duality," *Phys. Rev. D* **93** (2016) 065014, `arXiv:1512.00493 [hep-th]`.

[84] J. Durnin, M. J. Bhaseen, and B. Doyon, "Nonequilibrium Dynamics and Weakly Broken Integrability," *Phys. Rev. Lett.* **127** (2021) 130601, `arXiv:2004.11030 [cond-mat.stat-mech]`.

[85] D. Szász-Schagrin, B. Pozsgay, and G. Takacs, "Weak integrability breaking and level spacing distribution," *SciPost Physics* **11** (2021) 037, `arXiv:2103.06308 [cond-mat.stat-mech]`.

[86] G. Fodor, "A review on radiation of oscillons and oscillatons," *arXiv e-prints* (2019) arXiv:1911.03340, `arXiv:1911.03340 [hep-th]`.

[87] R. F. Dashen, B. Hasslacher, and A. Neveu, "Nonperturbative methods and extended-hadron models in field theory. II. Two-dimensional models and extended hadrons," *Phys. Rev. D* **10** (1974) 4130–4138.

[88] G. Mussardo, "Neutral bound states in kink-like theories," *Nucl. Phys. B* **779** (2007) 101–154, `arXiv:hep-th/0607025 [hep-th]`.

[89] Z. Bajnok and M. Lajer, "Truncated Hilbert space approach to the 2d ϕ^4 theory," *Journal of High Energy Physics* **2016** (2016) 50, `arXiv:1512.06901 [hep-th]`.

[90] F. H. L. Essler and R. M. Konik, "Application of Massive Integrable Quantum Field Theories to Problems in Condensed Matter Physics," in *From Fields to Strings: Circumnavigating Theoretical Physics: Ian Kogan Memorial Collection (in 3 Vols). Edited by SHIFMAN MISHA ET AL. Published by World Scientific Publishing Co. Pte. Ltd*, pp. 684–830. 2005.

[91] E. Haller, R. Hart, M. J. Mark, J. G. Danzl, L. Reichsöllner, M. Gustavsson, M. Dalmonte, G. Pupillo, and H.-C. Nägerl, "Pinning quantum phase transition for a Luttinger liquid of strongly interacting bosons," *Nature* **466** (2010) 597–600, `arXiv:1004.3168 [cond-mat.quant-gas]`.

[92] T. Giamarchi, *Quantum Physics in One Dimension*. Oxford UP, 2004.

[93] D. Controzzi, F. H. L. Essler, and A. M. Tsvelik, "Dynamical Properties of one dimensional Mott Insulators," *arXiv e-prints* (2000) cond–mat/0011439, `arXiv:cond-mat/0011439 [cond-mat.str-el]`.

[94] I. Affleck and M. Oshikawa, "Field-induced gap in Cu benzoate and other $S = \frac{1}{2}$ antiferromagnetic chains," *Phys. Rev. B* **60** (1999) 1038–1056.

[95] I. Umegaki, H. Tanaka, T. Ono, H. Uekusa, and H. Nojiri, "Elementary excitations of the $S = \frac{1}{2}$ one-dimensional antiferromagnet KCuGaF$_6$ in a magnetic field and quantum sine-Gordon model," *Phys. Rev. B* **79** (2009) 184401.

[96] S. A. Zvyagin, A. K. Kolezhuk, J. Krzystek, and R. Feyerherm, "Excitation Hierarchy of the Quantum Sine-Gordon Spin Chain in a Strong Magnetic Field," *Phys. Rev. Lett.* **93** (2004) 027201.

[97] F. H. L. Eßler, "Sine-Gordon low-energy effective theory for copper benzoate," *Phys. Rev. B* **59** (1999) 14376–14383, `arXiv:cond-mat/9811309 [cond-mat.str-el]`.

[98] A. Roy and H. Saleur, "Quantum electronic circuit simulation of generalized sine-Gordon models," *Phys. Rev. B* **100** (2019) 155425.

[99] A. Roy, D. Schuricht, J. Hauschild, F. Pollmann, and H. Saleur, "The quantum sine-Gordon model with quantum circuits," *Nucl. Phys. B* **968** (2021) 115445.

[100] V. Gritsev, A. Polkovnikov, and E. Demler, "Linear response theory for a pair of coupled one-dimensional condensates of interacting atoms," *Phys. Rev. B* **75** (2007) 174511, `arXiv:cond-mat/0701421 [cond-mat.other]`.

[101] M. Tajik, M. Gluza, N. Sebe, P. Schüttelkopf, F. Cataldini, J. Sabino, F. Møller, S.-C. Ji, S. Erne, G. Guarnieri, S. Sotiriadis, J. Eisert, and J. Schmiedmayer, "Experimental observation of curved light-cones in a quantum field simulator," *Proceedings of the National Academy of Science* **120** (2023) e2301287120, `arXiv:2209.09132 [cond-mat.quant-gas]`.

[102] T. Schweigler, V. Kasper, S. Erne, I. Mazets, B. Rauer, F. Cataldini, T. Langen, T. Gasenzer, J. Berges, and J. Schmiedmayer, "Experimental characterization of a quantum many-body system via higher-order correlations," *Nature* **545** (2017) 323–326, `arXiv:1505.03126 [cond-mat.quant-gas]`.

[103] A. B. Zamolodchikov, "Mass Scale in the Sine-Gordon Model and its Reductions," *Int. J. Mod. Phys. A* **10** (1995) 1125–1150.

[104] F. Cooper and E. Mottola, "Initial-value problems in quantum field theory in the large-n approximation," *Phys. Rev. D* **36** (1987) 3114–3127. `https://link.aps.org/doi/10.1103/PhysRevD.36.3114`.

[105] D. Boyanovsky, "Quantum spinodal decomposition," *Phys. Rev. E* **48** (1993) 767–771. `https://link.aps.org/doi/10.1103/PhysRevE.48.767`.

[106] D. Boyanovsky, D.-S. Lee, and A. Singh, "Phase transitions out of equilibrium: Domain formation and growth," *Phys. Rev. D* **48** (1993) 800–815. `https://link.aps.org/doi/10.1103/PhysRevD.48.800`.

[107] D. Boyanovsky and H. J. de Vega, "Quantum rolling down out of equilibrium," *Phys. Rev. D* **47** (1993) 2343–2355. `https://link.aps.org/doi/10.1103/PhysRevD.47.2343`.

[108] G. F. Bonini and C. Wetterich, "Time evolution of correlation functions and thermalization," *Phys. Rev. D* **60** (1999) 105026. `https://link.aps.org/doi/10.1103/PhysRevD.60.105026`.

[109] A. Giraud and J. Serreau, "Decoherence and thermalization of a pure quantum state in quantum field theory," *Phys. Rev. Lett.* **104** (2010) 230405. `https://link.aps.org/doi/10.1103/PhysRevLett.104.230405`.

[110] Y. D. van Nieuwkerk and F. H. L. Essler, "Self-consistent time-dependent harmonic approximation for the sine-Gordon model out of equilibrium," *Journal of Statistical Mechanics: Theory and Experiment* **8** (2019) 084012, `arXiv:1812.06690 [cond-mat.quant-gas]`.

[111] S. Sotiriadis and J. Cardy, "Quantum quench in interacting field theory: A self-consistent approximation," *Phys. Rev. B* **81** (2010) 134305, `arXiv:1002.0167 [quant-ph]`.

[112] A. Polkovnikov, "Phase space representation of quantum dynamics," *Annals of Physics* **325** (2010) 1790–1852, `arXiv:0905.3384 [cond-mat.stat-mech]`.

[113] A. Polkovnikov, "Quantum corrections to the dynamics of interacting bosons: Beyond the truncated Wigner approximation," *Phys. Rev. A* **68** (2003) 053604, `arXiv:cond-mat/0303628 [cond-mat.stat-mech]`.

[114] A. A. Radovskaya and A. G. Semenov, "Semiclassical approximation meets Keldysh-Schwinger diagrammatic technique: scalar φ^4," *European Physical Journal C* **81** (2021) 704, `arXiv:2003.06395 [hep-ph]`.

[115] D. X. Horváth, I. Lovas, M. Kormos, G. Takács, and G. Zaránd, "Nonequilibrium time evolution and rephasing in the quantum sine-Gordon model," *Phys. Rev. A* **100** (2019) 013613, `arXiv:1809.06789 [cond-mat.quant-gas]`.

[116] V. P. Yurov and A. B. Zamolodchikov, "Truncated Comformal Space Approach to Scaling Lee-Yang Model," *International Journal of Modern Physics A* **5** (1990) 3221–3245.

[117] T. Rakovszky, M. Mestyán, M. Collura, M. Kormos, and G. Takács, "Hamiltonian truncation approach to quenches in the Ising field theory," *Nuclear Physics B* **911** (2016) 805–845, `arXiv:1607.01068 [cond-mat.stat-mech]`.

[118] D. X. Horváth and G. Takács, "Overlaps after quantum quenches in the sine-Gordon model," *Physics Letters B* **771** (2017) 539–545, `arXiv:1704.00594 [cond-mat.stat-mech]`.

[119] K. Hódsági, M. Kormos, and G. Takács, "Quench dynamics of the Ising field theory in a magnetic field," *SciPost Physics* **5** (2018) 027, `arXiv:1803.01158 [cond-mat.stat-mech]`.

[120] I. Kukuljan, S. Sotiriadis, and G. Takacs, "Correlation Functions of the Quantum Sine-Gordon Model in and out of Equilibrium," *Phys. Rev. Lett.* **121** (2018) 110402, `arXiv:1802.08696 [cond-mat.stat-mech]`.

[121] K. Hódsági, M. Kormos, and G. Takács, "Perturbative post-quench overlaps in quantum field theory," *Journal of High Energy Physics* **2019** (2019) 47, `arXiv:1905.05623 [cond-mat.stat-mech]`.

[122] I. Kukuljan, "Continuum approach to real time dynamics of (1 +1)D gauge field theory: Out of horizon correlations of the Schwinger model," *Phys. Rev. D* **104** (2021) L021702, `arXiv:2101.07807 [hep-th]`.

[123] P. Fonseca and A. Zamolodchikov, "Ising field theory in a magnetic field: analytic properties of the free energy," *arXiv e-prints* (2001) hep–th/0112167, `arXiv:hep-th/0112167 [hep-th]`.

[124] G. Feverati, F. Ravanini, and G. Takács, "Truncated conformal space at c=1, nonlinear integral equation and quantization rules for multi-soliton states," *Physics Letters B* **430** (1998) 264–273, `arXiv:hep-th/9803104 [hep-th]`.

[125] P. Dorey, A. J. Pocklington, R. Tateo, and G. Watts, "TBA and TCSA with boundaries and excited states," *Nuclear Physics B* **525** (1998) 641–663, `arXiv:hep-th/9712197 [hep-th]`.

[126] Z. Bajnok, L. Palla, and G. Takács, "Boundary states and finite size effects in sine-Gordon model with Neumann boundary condition," *Nuclear Physics B* **614** (2001) 405–448, `arXiv:hep-th/0106069 [hep-th]`.

[127] Z. Bajnok, L. Holló, and G. Watts, "Defect scaling Lee-Yang model from the perturbed DCFT point of view," *Nuclear Physics B* **886** (2014) 93–124, `arXiv:1307.4536 [hep-th]`.

[128] A. J. A. James, R. M. Konik, P. Lecheminant, N. J. Robinson, and A. M. Tsvelik, "Non-perturbative methodologies for low-dimensional strongly-correlated systems: From non-Abelian bosonization to truncated spectrum methods," *Reports on Progress in Physics* **81** (2018) 046002, `arXiv:1703.08421 [cond-mat.str-el]`.

[129] E. Katz, Z. U. Khandker, and M. T. Walters, "A conformal truncation framework for infinite-volume dynamics," *Journal of High Energy Physics* **2016** (2016) 140, `arXiv:1604.01766 [hep-th]`.

[130] N. Anand, A. L. Fitzpatrick, E. Katz, Z. U. Khandker, M. T. Walters, and Y. Xin, "Introduction to Lightcone Conformal Truncation: QFT Dynamics from CFT Data," *arXiv e-prints* (2020) arXiv:2005.13544, `arXiv:2005.13544 [hep-th]`.

[131] D. X. Horváth, K. Hódsági, and G. Takács, "Chirally factorised truncated conformal space approach," *Computer Physics Communications* **277** (2022) 108376, `arXiv:2201.06509 [hep-th]`.

[132] D. Horvath, S. Sotiriadis, M. Kormos, and G. Takacs, "Inhomogeneous quantum quenches in the sine-Gordon theory," *SciPost Physics* **12** (2022) 144, `arXiv:2109.06869 [cond-mat.str-el]`.

[133] G. Feverati, K. Graham, P. A. Pearce, G. Z. Tóth, and G. M. T. Watts, "A renormalization group for the truncated conformal space approach," *J. Stat. Mech.: Theory Exp.* **2008** (2008) 03011, `arXiv:cond-mat/0701605 [cond-mat.str-el]`.

[134] R. M. Konik and Y. Adamov, "Numerical Renormalization Group for Continuum One-Dimensional Systems," *Phys. Rev. Lett.* **98** (2007) 147205.

[135] P. Giokas and G. Watts, "The renormalisation group for the truncated conformal space approach on the cylinder," *arXiv e-prints* (2011) arXiv:1106.2448, `arXiv:1106.2448 [hep-th]`.

[136] S. Lukyanov and A. Zamolodchikov, "Exact expectation values of local fields in the quantum sine-Gordon model," *Nuclear Physics B* **493** (1997) 571–587, `arXiv:hep-th/9611238 [hep-th]`.

[137] B. Pozsgay, "Current operators in integrable spin chains: lessons from long range deformations," *SciPost Physics* **8** (2020) 016, `arXiv:1910.12833 [cond-mat.stat-mech]`.

[138] O. A. Castro-Alvaredo, B. Doyon, and T. Yoshimura, "Emergent Hydrodynamics in Integrable Quantum Systems Out of Equilibrium," *Physical Review X* **6** (2016) 041065, `arXiv:1605.07331 [cond-mat.stat-mech]`.

[139] B. Bertini, M. Collura, J. De Nardis, and M. Fagotti, "Transport in Out-of-Equilibrium X X Z Chains: Exact Profiles of Charges and Currents," *Phys. Rev. Lett.* **117** (2016) 207201, `arXiv:1605.09790 [cond-mat.stat-mech]`.

[140] D.-L. VU and T. Yoshimura, "Equations of state in generalized hydrodynamics," *SciPost Physics* **6** (2019) 023, `arXiv:1809.03197 [cond-mat.stat-mech]`.

[141] A. Urichuk, Y. Oez, A. Klümper, and J. Sirker, "The spin Drude weight of the XXZ chain and generalized hydrodynamics," *SciPost Physics* **6** (2019) 005.

[142] X. Cao, V. B. Bulchandani, and H. Spohn, "The GGE averaged currents of the classical Toda chain," *Journal of Physics A Mathematical General* **52** (2019) 495003, `arXiv:1905.04548 [cond-mat.stat-mech]`.

[143] M. Borsi, B. Pozsgay, and L. Pristyák, "Current Operators in Bethe Ansatz and Generalized Hydrodynamics: An Exact Quantum-Classical Correspondence," *Physical Review X* **10** (2020) 011054, `arXiv:1908.07320 [cond-mat.stat-mech]`.

[144] N. Beisert, "The dilatation operator of N=4 super Yang Mills theory and integrability," *Phys. Rep.* **405** (2004) 1–202, `arXiv:hep-th/0407277 [hep-th]`.

[145] T. Bargheer, N. Beisert, and F. Loebbert, "LETTER: Boosting nearest-neighbour to long-range integrable spin chains," *Journal of Statistical Mechanics: Theory and Experiment* **2008** (2008) L11001, `arXiv:0807.5081 [hep-th]`.

[146] T. Bargheer, N. Beisert, and F. Loebbert, "Long-range deformations for integrable spin chains," *Journal of Physics A Mathematical General* **42** (2009) 285205, `arXiv:0902.0956 [hep-th]`.

[147] B. Pozsgay, Y. Jiang, and G. Takács, "T T ¯-deformation and long range spin chains," *Journal of High Energy Physics* **2020** (2020) 92, `arXiv:1911.11118 [hep-th]`.

[148] F. A. Smirnov and A. B. Zamolodchikov, "On space of integrable quantum field theories," *Nuclear Physics B* **915** (2017) 363–383, `arXiv:1608.05499 [hep-th]`.

[149] A. Cavaglià, N. Gromov, and F. Levkovich-Maslyuk, "Separation of variables and scalar products at any rank," *Journal of High Energy Physics* **2019** (2019) 52, `arXiv:1907.03788 [hep-th]`.

[150] A. B. Zamolodchikov, "From tricritical Ising to critical Ising by thermodynamic Bethe ansatz," *Nuclear Physics B* **358** (1991) 524–546.

[151] G. Mussardo and P. Simon, "Bosonic-type /S -matrix, vacuum instability and CDD ambiguities," *Nuclear Physics B* **578** (2000) 527–551, `arXiv:hep-th/9903072 [hep-th]`.

[152] A. Bastianello, A. De Luca, and R. Vasseur, "Hydrodynamics of weak integrability breaking," *Journal of Statistical Mechanics: Theory and Experiment* **2021** (2021) 114003, `arXiv:2103.11997 [cond-mat.stat-mech]`.

[153] B. Doyon, J. Durnin, and T. Yoshimura, "The Space of Integrable Systems from Generalised $T\bar{T}$-Deformations," *SciPost Physics* **13** (2022) 072, `arXiv:2105.03326 [hep-th]`.

[154] P. Jung, R. W. Helmes, and A. Rosch, "Transport in Almost Integrable Models: Perturbed Heisenberg Chains," *Phys. Rev. Lett.* **96** (2006) 067202, `arXiv:cond-mat/0509615 [cond-mat.str-el]`.

[155] D. A. Rabson, B. N. Narozhny, and A. J. Millis, "Crossover from Poisson to Wigner-Dyson level statistics in spin chains with integrability breaking," *Phys. Rev. B* **69** (2004) 054403, `arXiv:cond-mat/0308089 [cond-mat]`.

[156] M. Rigol and L. F. Santos, "Quantum chaos and thermalization in gapped systems," *Phys. Rev. A* **82** (2010) 011604, `arXiv:1003.1403 [cond-mat.stat-mech]`.

[157] L. F. Santos and M. Rigol, "Onset of quantum chaos in one-dimensional bosonic and fermionic systems and its relation to thermalization," *Phys. Rev. E* **81** (2010) 036206, `arXiv:0910.2985 [cond-mat.stat-mech]`.

[158] L. F. Santos and M. Rigol, "Localization and the effects of symmetries in the thermalization properties of one-dimensional quantum systems," *Phys. Rev. E* **82** (2010) 031130, `arXiv:1006.0729 [cond-mat.stat-mech]`.

[159] G. P. Brandino, R. M. Konik, and G. Mussardo, "Energy level distribution of perturbed conformal field theories," *Journal of Statistical Mechanics: Theory and Experiment* **2010** (2010) 07013, `arXiv:1004.4844 [cond-mat.stat-mech]`.

[160] L. D'Alessio, Y. Kafri, A. Polkovnikov, and M. Rigol, "From quantum chaos and eigenstate thermalization to statistical mechanics and thermodynamics," *Advances in Physics* **65** (2016) 239–362, arXiv:1509.06411 [cond-mat.stat-mech].

[161] W. Beugeling, R. Moessner, and M. Haque, "Off-diagonal matrix elements of local operators in many-body quantum systems," *Phys. Rev. E* **91** (2015) 012144, arXiv:1407.2043 [cond-mat.stat-mech].

[162] W. Beugeling, A. Bäcker, R. Moessner, and M. Haque, "Statistical properties of eigenstate amplitudes in complex quantum systems," *Phys. Rev. E* **98** (2018) 022204, arXiv:1710.11433 [cond-mat.stat-mech].

[163] M. Haque, P. A. McClarty, and I. M. Khaymovich, "Entanglement of midspectrum eigenstates of chaotic many-body systems: Reasons for deviation from random ensembles," *Phys. Rev. E* **105** (2022) 014109, arXiv:2008.12782 [cond-mat.stat-mech].

[164] B. Bertini, P. Kos, and T. Prosen, "Exact Spectral Form Factor in a Minimal Model of Many-Body Quantum Chaos," *Phys. Rev. Lett.* **121** (2018) 264101, arXiv:1805.00931 [nlin.CD].

[165] M. Srdinšek, T. Prosen, and S. Sotiriadis, "Signatures of Chaos in Nonintegrable Models of Quantum Field Theories," *Phys. Rev. Lett.* **126** (2021) 121602, arXiv:2012.08505 [cond-mat.stat-mech].

[166] B. Fitos and G. Takács, "Weak vs. strong breaking of integrability in interacting scalar quantum field theories," *SciPost Physics* **15** (2023) 137, arXiv:2305.02666 [cond-mat.stat-mech].

[167] K. Kudo and T. Deguchi, "Unexpected non-Wigner behavior in level-spacing distributions of next-nearest-neighbor coupled XXZ spin chains," *Phys. Rev. B* **68** (2003) 052510, arXiv:cond-mat/0308099 [cond-mat.stat-mech].

[168] K. Kudo and T. Deguchi, "Level Statistics of XXZ Spin Chains with Discrete Symmetries: Analysis through Finite-size Effects," *Journal of the Physical Society of Japan* **74** (2005) 1992–2000, arXiv:cond-mat/0409761 [cond-mat.stat-mech].

[169] R. Modak and S. Mukerjee, "Finite size scaling in crossover among different random matrix ensembles in microscopic lattice models," *New Journal of Physics* **16** (2014) 093016, arXiv:1310.1443 [cond-mat.stat-mech].

[170] R. Modak, S. Mukerjee, and S. Ramaswamy, "Universal power law in crossover from integrability to quantum chaos," *Phys. Rev. B* **90** (2014) 075152, arXiv:1309.1865 [cond-mat.str-el].

[171] M. Lüscher, "Volume dependence of the energy spectrum in massive quantum field theories: I. Stable particle states," *Communications in Mathematical Physics* **104** (1986) 177–206.

[172] M. Lüscher, "Volume dependence of the energy spectrum in massive quantum field theories: II. Scattering states," *Communications in Mathematical Physics* **105** (1986) 153–188.

[173] E. G. Dalla Torre, E. Demler, and A. Polkovnikov, "Universal Rephasing Dynamics after a Quantum Quench via Sudden Coupling of Two Initially Independent Condensates," *Phys. Rev. Lett.* **110** (2013) 090404, `arXiv:1211.5145 [cond-mat.quant-gas]`.

[174] D. Szász-Schagrin, I. Lovas, and G. Takács, "Nonequilibrium time evolution in the sine-gordon model," *Phys. Rev. B* **109** (2024) 014308. `https://link.aps.org/doi/10.1103/PhysRevB.109.014308`.

[175] S. Coleman, "Fate of the false vacuum: Semiclassical theory," *Phys. Rev. D* **15** (1977) 2929–2936.

[176] J. Callan, Curtis G. and S. Coleman, "Fate of the false vacuum. II. First quantum corrections," *Phys. Rev. D* **16** (1977) 1762–1768.

[177] A. Andreassen, W. Frost, and M. D. Schwartz, "Consistent use of the standard model effective potential," *Phys. Rev. Lett.* **113** (2014) 241801. `https://link.aps.org/doi/10.1103/PhysRevLett.113.241801`.

[178] T. P. Billam, R. Gregory, F. Michel, and I. G. Moss, "Simulating seeded vacuum decay in a cold atom system," *Phys. Rev. D* **100** (2019) 065016, `arXiv:1811.09169 [hep-th]`.

[179] T. P. Billam, K. Brown, and I. G. Moss, "Simulating cosmological supercooling with a cold-atom system," *Phys. Rev. A* **102** (2020) 043324, `arXiv:2006.09820 [cond-mat.quant-gas]`.

[180] K. Lun Ng, B. Opanchuk, M. Thenabadu, M. Reid, and P. D. Drummond, "The fate of the false vacuum: Finite temperature, entropy and topological phase in quantum simulations of the early universe," *arXiv e-prints* (2020) arXiv:2010.08665, `arXiv:2010.08665 [quant-ph]`.

[181] T. P. Billam, K. Brown, A. J. Groszek, and I. G. Moss, "Simulating cosmological supercooling with a cold atom system II," *arXiv e-prints* (2021) arXiv:2104.07428, `arXiv:2104.07428 [cond-mat.quant-gas]`.

[182] S. Abel and M. Spannowsky, "Observing the fate of the false vacuum with a quantum laboratory," *arXiv e-prints* (2020) arXiv:2006.06003, `arXiv:2006.06003 [hep-th]`.

[183] A. Zenesini, A. Berti, R. Cominotti, C. Rogora, I. G. Moss, T. P. Billam, I. Carusotto, G. Lamporesi, A. Recati, and G. Ferrari, "Observation of false vacuum decay via bubble formation in ferromagnetic superfluids," *Nat. Phys.* (2024) , `arXiv:2305.05225 [hep-ph]`.

[184] M. B. Voloshin, "Decay of false vacuum in (1+1) dimensions," *ITEP* **8** (1985) 21.

[185] S. B. Rutkevich, "Decay of the metastable phase in d=1 and d=2 Ising models," *Phys. Rev. B* **60** (1999) 14525–14528, `arXiv:cond-mat/9904059` `[cond-mat.stat-mech]`.

[186] A. Ivanov, M. Matteini, M. Nemevšek, and L. Ubaldi, "Analytic thin wall false vacuum decay rate," *Journal of High Energy Physics* **2022** (2022) 209, `arXiv:2202.04498 [hep-th]`.

[187] A. Andreassen, D. Farhi, W. Frost, and M. D. Schwartz, "Direct approach to quantum tunneling," *Phys. Rev. Lett.* **117** (2016) 231601. `https://link.aps.org/doi/10.1103/PhysRevLett.117.231601`.

[188] M. Lencsés, G. Mussardo, and G. Takács, "Variations on vacuum decay: The scaling Ising and tricritical Ising field theories," *Phys. Rev. D* **106** (2022) 105003, `arXiv:2208.02273 [hep-th]`.

[189] G. Lagnese, F. M. Surace, M. Kormos, and P. Calabrese, "False vacuum decay in quantum spin chains," *Phys. Rev. B* **104** (2021) L201106, `arXiv:2107.10176` `[cond-mat.stat-mech]`.

[190] A. Degasperis, L. Fonda, and G. C. Ghirardi, "Does the lifetime of an unstable system depend on the measuring apparatus?," *Nuovo Cimento A Serie* **21** (1974) 471–484.

[191] B. Misra and E. C. G. Sudarshan, "The Zeno's paradox in quantum theory," *Journal of Mathematical Physics* **18** (1977) 756–763.

[192] A. Lerose, F. M. Surace, P. P. Mazza, G. Perfetto, M. Collura, and A. Gambassi, "Quasilocalized dynamics from confinement of quantum excitations," *Phys. Rev. B* **102** (2020) 041118, `arXiv:1911.07877 [cond-mat.stat-mech]`.

[193] O. Pomponio, M. A. Werner, G. Zaránd, and G. Takacs, "Bloch oscillations and the lack of the decay of the false vacuum in a one-dimensional quantum spin chain," *SciPost Physics* **12** (2022) 061, `arXiv:2105.00014 [cond-mat.stat-mech]`.

[194] V. B. Bulchandani, D. A. Huse, and S. Gopalakrishnan, "Onset of many-body quantum chaos due to breaking integrability," *Phys. Rev. B* **105** (2022) 214308, `arXiv:2112.14762 [cond-mat.stat-mech]`.

[195] M. Pigneur, T. Berrada, M. Bonneau, T. Schumm, E. Demler, and J. Schmiedmayer, "Relaxation to a Phase-Locked Equilibrium State in a One-Dimensional Bosonic Josephson Junction," *Phys. Rev. Lett.* **120** (2018) 173601, `arXiv:1711.06635` `[quant-ph]`.

[196] J. F. Mennemann, I. E. Mazets, M. Pigneur, H. P. Stimming, N. J. Mauser, J. Schmiedmayer, and S. Erne, "Relaxation in an extended bosonic Josephson junction," *Physical Review Research* **3** (2021) 023197, `arXiv:2012.05885` `[cond-mat.quant-gas]`.

[197] Y. D. van Nieuwkerk, J. Schmiedmayer, and F. Essler, "Josephson oscillations in split one-dimensional Bose gases," *SciPost Physics* **10** (2021) 090, `arXiv:2010.11214 [cond-mat.quant-gas]`.

[198] Y. D. van Nieuwkerk and F. Essler, "On the low-energy description for tunnel-coupled one-dimensional Bose gases," *SciPost Physics* **9** (2020) 025, `arXiv:2003.07873 [cond-mat.quant-gas]`.

[199] D. Szász-Schagrin, I. Lovas, and G. Takács, "Quantum quenches in an interacting field theory: Full quantum evolution versus semiclassical approximations," *Phys. Rev. B* **105** (2022) 014305, `arXiv:2110.01636 [cond-mat.stat-mech]`.

[200] D. Szász-Schagrin and G. Takács, "False vacuum decay in the $(1+1)$-dimensional φ^4 theory," *Phys. Rev. D* **106** (2022) 025008, `arXiv:2205.15345 [hep-th]`.